# Assessing neutron-induced carcinogenesis risk in high-energy radiation therapy: a Monte Carlo and track structure study


**Sachin Dev**

Medical Physics Unit

McGill University, Montreal

December 2024

A thesis submitted to McGill University in partial fulfillment of the requirements for the degree of

*Master of Science in Medical Radiation Physics*

# Acknowledgments

I am very grateful to my supervisor, Prof. John Kildea, for his invaluable guidance, encouragement, and mentorship throughout my MSc studies. I feel incredibly fortunate to have worked under John's supervision for two years, and I deeply appreciate the unwavering support he has provided.

I would like to express my sincere thanks to Ives, Peter, Piotr, Emily, Gabriela, Joseph, and Norma for creating an exceptional learning environment and offering their guidance throughout my courses.

To the members of the NICE-ROKS research group, I extend my heartfelt gratitude. Thank you, Felix and Chris, for the countless hours of discussion; Kalya and Odette, for your help with my presentations; Trey, for your unwavering support and motivation; and Nicola, James, and Zhenlun, for your assistance with TOPAS. Special thanks to Luc for translating my abstracts into French. I am also deeply thankful to Elliot, Gabriel, Josie, Abbey, and Paula for their friendship and camaraderie, and to Sarah, Gabriel, Renée, and Jules for our memorable lunches at Glen. Tony, I am grateful for all the weekend outings and the time we spent together. Margery, your love and support from my very first day at MPU mean the world to me.

Finally, I sincerely acknowledge the financial support provided by John. I am deeply thankful to my parents and family for their unwavering support.

To all who have contributed to my academic and personal growth, directly or indirectly, I am deeply indebted and offer my heartfelt thanks.

# Abstract

Secondary neutrons generated as a byproduct of high-energy radiotherapy (>8 MeV) increase the risk of iatrogenic cancers in patients. These neutrons are unavoidable as they get generated in the treatment machine as well as in patients' tissues during treatment. We aimed to investigate the relative biological effectiveness (RBE) of secondary neutrons by examining neutron-induced DNA damage in cells exposed in vitro to realistic neutron spectra at different locations in a 15 MV linac bunker. Previous studies have investigated the carcinogenic risk of neutrons using a flat neutron spectrum (uniform energy spectrum) and a spherical phantom model (ICRU-4 sphere) to represent the human torso. However, in this study, we are modeling a real-world cell irradiation experiment by modeling an in-vitro cell irradiation geometry in a Monte Carlo simulation and exposing it to realistic neutron spectra as measured in a radiotherapy bunker during a high-energy treatment procedure to evaluate DNA damage yields and corresponding RBEs.

This study built upon our Neutron-Induced Carcinogenic Effects (NICE) group's existing simulation pipeline. As a first step, we modeled an ICRU sphere phantom in TOPAS v3.6 and recorded the spectra of secondary charged particles from a flat spectrum of neutrons (1 keV, 1 MeV, 10 MeV). Validation was achieved by replicating the simulations in Geant4 v10.06, on which TOPAS v3.6 is based, and comparing the results to the previous work by our group using Geant4 v10.04 while accounting for changes to the Geant4 Monte Carlo toolkit between versions 10.04 and 10.06. Additionally, to correctly account for the transport of low energy neutrons in heterogeneous materials, a novel TOPAS extension was developed to simulate thermal neutron transport below 4 eV, thereby enhancing TOPAS's simulation capabilities in this energy regime for the first time.

Following validation, a cell culture flask geometry representing an in-vitro experimental setup was modeled in TOPAS and irradiated with realistic neutron spectra previously measured by our group in a 15 MV linac bunker. Secondary charged particle spectra (electrons, protons, oxygen ions) from the centermost scoring volume of the flask were

used in DNA track structure simulations in TOPAS-nBio. DNA damage yields from the neutron spectra were compared with those induced by 250 keV X-rays to calculate corresponding neutron RBEs based on complex DSB cluster ratios. The dose-dependence of the neutron RBEs was explored across doses from 0.1 Gy to 5.0 Gy. This study advances the bottom-up simulation methodology for neutron RBE estimation and offers a framework for future research into neutron-induced carcinogenesis.

# Résumé

Les neutrons secondaires générés comme sous-produit de la radiothérapie à haute énergie (>8 MeV) augmentent le risque de cancers iatrogènes chez les patients. La présence de ces neutrons est inévitable, car ils sont produits dans l'appareil de traitement et dans les tissus des patients pendant le traitement. Notre but était d'étudier l'efficacité biologique relative (EBR) des neutrons secondaires en examinant les dommages à l'ADN in vitro induits par les neutrons dans des cellules exposées à des spectres réalistiques de neutrons mesurés à différents emplacements dans un bunker de linac (accélérateur linéaire) de 15 MV. Des études précédentes ont analysé la cancérogénicité des neutrons en utilisant un spectre uniforme de neutrons et un modèle fantôme sphérique (sphère ICRU-4) pour représenter le torse humain. Cependant, dans cette étude, nous modélisons une expérience réelle d'irradiation en représentant la géométrie d'une irradiation cellulaire in vitro par une simulation Monte Carlo et en l'exposant à des spectres réalistiques de neutrons mesurés dans un bunker de radiothérapie lors d'une procédure de traitement à haute énergie afin d'évaluer les rendements des dommages à l'ADN et les EBR correspondants.

Cette étude s'appuie sur la procédure de simulation créée par notre groupe NICE (Neutron-Induced Carcinogenic Effects). Dans un premier temps, nous avons modélisé un fantôme sphérique ICRU dans TOPAS v3.6 et enregistré les spectres des particules secondaires chargées produites par un spectre uniforme de neutrons (1 keV, 1 MeV, 10 MeV). La validation a été réalisée en reproduisant les simulations dans Geant4 v10.06, sur lequel est basé TOPAS v3.6, et en comparant les résultats avec les travaux précédents de notre groupe utilisant Geant4 v10.04, tout en tenant compte des modifications apportées aux outils Monte Carlo Geant4 entre les versions 10.04 et 10.06. De plus, pour prendre en compte correctement le transport des neutrons de basse énergie dans les matériaux hétérogènes, une nouvelle extension de TOPAS a été développée pour simuler le transport des neutrons thermiques sous 4 eV, améliorant ainsi pour la première fois les capacités de simulation de TOPAS dans cette plage d'énergie.

Après validation, la géométrie d’un flacon de culture représentant un dispositif expérimental in vitro a été modélisée dans TOPAS et irradiée avec des spectres réalistiques de neutrons mesurés précédemment par notre groupe dans un bunker de linac de 15 MV. Les spectres des particules secondaires chargées (électrons, protons, ions oxygène) provenant du volume d’évaluation centrique du flacon ont été utilisés dans des simulations de structures de tracés d’ADN dans TOPAS-nBio. Les rendements des dommages à l’ADN dus aux spectres de neutrons ont été comparés à ceux induits par des rayons X de 250 keV pour calculer les EBR correspondants sur la base de ratios de cassures double-brin complexes groupés. La dépendance de l’EBR des neutrons à la dose a été explorée pour des doses comprises entre 0,1 Gy et 5,0 Gy. Cette étude fait progresser la méthode de simulation ascendante pour l'estimation de l'EBR des neutrons et offre un cadre pour les recherches futures sur la cancérogenèse induite par les neutrons.

# Contents

# List of Figures

# List of Tables

# List of Abbreviations

| | |
|---|---|
| **BIC** | Binary Cascade |
| **CERN** | European Council for Nuclear Research |
| **CH** | Condensed History (Monte Carlo) |
| **DNA** | Deoxyribonucleic Acid |
| **DSB** | Double Strand Break |
| **EBRT** | External Beam Radiation Therapy |
| **GEANT4** | Geometry And Tracking 4 |
| **HP** | High Precision |
| **ICRP** | International Commission on Radiological Protection |
| **ICRU** | International Commission on Radiation Units and Measurements |
| **ICRU-4** | ICRU 4-component soft tissue-equivalent sphere |
| **KERMA** | Kinetic Energy Released per unit Mass |
| **LET** | Linear Energy Transfer |
| **LINAC** | Linear Accelerator |
| **MC** | Monte Carlo |
| **MU** | Monitor Unit |
| **NICE** | Neutron-Induced Carcinogenic Effects |
| **PARTRAC** | Particle Track structure code |
| **PHITS** | Particle and Heavy Ion Transport code system |
| **QGS** | Quark-Gluon String |
| **RBE** | Relative Biological Effectiveness |

| | |
|---|---|
| **SSB** | Single Strand Break |
| **TOPAS** | Tool for Particle Simulation |
| **TOPAS-CDD** | TOPAS Clustered DNA Damage |
| **TS** | Track Structure |
| **US NRC** | United States Nuclear Regulatory Commission |

# Contribution of Authors

This thesis was exclusively written by the author, Sachin Dev, with guidance from Prof. John Kildea. Unless otherwise indicated, all figures and tables were produced by the author. All main sources of help were acknowledged.

# Chapter 1

# Introduction

## 1.1 Cancer and its statistics

Cancer is a group of diseases characterized by the uncontrolled growth and spread of abnormal cells [1]. If not detected and treated early, it can lead to serious health complications and death. Cancer is caused by genetic mutations that disrupt normal cellular processes such as proliferation, differentiation, and apoptosis. These mutations can be triggered by a combination of genetic predisposition, environmental exposures, and lifestyle factors, including smoking, diet, and physical inactivity [2]. Tumors are broadly categorized into two types based on their nature: benign tumors and malignant tumors [2]. Benign tumors are non-cancerous growths that do not invade into nearby tissues or spread to other parts of the body. These are slow-growing and localized. Malignant tumors are cancerous and have the potential to invade nearby tissues and metastasize to distant parts of the body through the blood or lymphatic system. They grow rapidly.

In Canada, cancer is a leading cause of mortality, accounting for approximately 22% of all deaths annually [3]. It is estimated that 45% of Canadians will be diagnosed with cancer in their lifetime. In 2023, it was projected that there would be over 240,000 new cancer cases and nearly 85,000 cancer-related deaths in Canada [3].

The most diagnosed cancers in Canada include lung, breast, prostate, and colorectal cancers. Lung cancer remains the leading cause of cancer-related deaths, responsible for approximately 25% of all cancer deaths.

The choice of treatment depends on the type of cancer, its stage, the patient's overall health, and specific genetic or molecular characteristics of the tumor. The most common cancer treatment options include removal of the tumor surgically, use of cytotoxic drugs to kill rapidly dividing cancer cells and using ionizing radiation to kill cancer cells.

## 1.2 Radiation therapy

Radiation therapy (RT) is a cornerstone in cancer treatment, utilizing ionizing radiation (radiation) to destroy malignant cells while sparing normal tissues as much as possible. It works by damaging the DNA of cancer cells, destroying their ability to replicate and leading to cell death. This method can be used as a standalone treatment or in conjunction with surgery, chemotherapy, and immunotherapy, depending on the type and stage of the cancer.

### Brachytherapy

Brachytherapy involves placing radioactive sources directly inside or near the tumor site, delivering high doses of radiation locally while limiting exposure to surrounding healthy tissues. It is commonly used for cancers of the cervix, prostate, breast, and skin. It is particularly effective for localized tumors and its precise targeting minimizes radiation to surrounding tissues.

### External beam radiation therapy (EBRT)

External beam radiation therapy (EBRT), on the other hand, relies primarily on linear accelerators (LINACs) to deliver radiation from outside the body.

A LINAC is a device that accelerates electrons to high energies using high-frequency electromagnetic waves within a linear tube. The resulting high-energy electron beam can be directly used to treat superficial tumors or directed to a target to produce X-rays (photon beam) for treating deeper tumors. The photon beam is then shaped using highly attenuating jaws to match the tumor's geometry before leaving the machine. LINACs feature a rotating gantry that houses the delivery and shaping components, enabling the beam to target the tumor from multiple angles as the patient lies on a treatment couch (Figure 1.1). The amount of radiation delivered by a LINAC is measured is terms of Monitor Unit (MU). It corresponds to the calibrated dose delivered to a specific point under defined conditions. This versatility makes LINACs suitable for treating a wide range of tumor types.

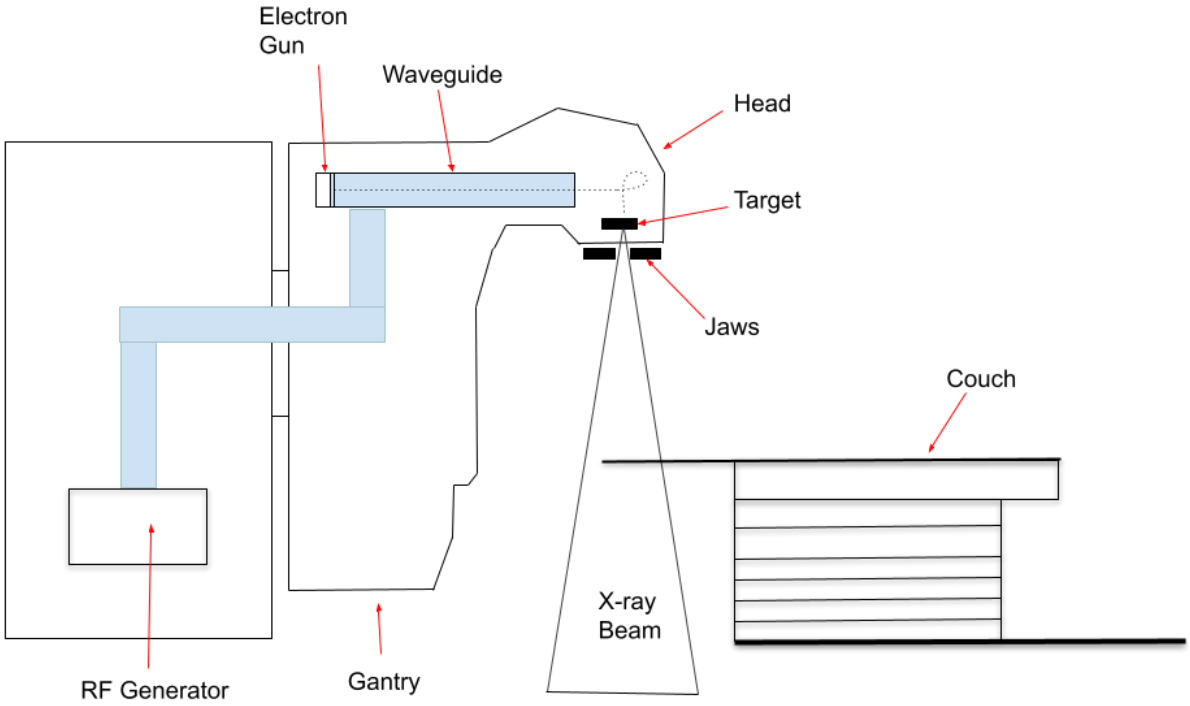


Figure 1.1 Schematic diagram of a medical linear accelerator.

In high-energy radiotherapy (≥ 8 MeV), patients are exposed to whole-body secondary neutron radiation that is generated by interactions of the high-energy primary radiation with the components of the LINAC head and patients' tissue [4]. This unavoidable exposure to secondary neutrons poses a risk of developing iatrogenic cancer for patients.

## 1.3 Radiation-induced carcinogenesis

Exposure to ionizing radiation can induce carcinogenesis [2]. Ionizing radiation, such as X-rays, γ-rays, or particle radiation, can damage cellular DNA through direct interactions or indirectly by generating reactive oxygen species. The resulting DNA damage can lead to mutations if not properly repaired. Radiation-induced cancers often have a long latency period, ranging from years to decades, depending on factors such as the type of cancer, radiation dose, and individual susceptibility. Different tissues have varying sensitivities to

radiation-induced carcinogenesis. Rapidly dividing tissues (e.g., bone marrow, thyroid, breast) are more susceptible, as their higher mitotic activity increases the likelihood of DNA damage propagation [2]

## 1.4 Project Objectives

The overarching goal of this thesis is to estimate the relative biological effectiveness (RBE) of neutrons under real-world conditions using TOPAS [5] and TOPAS-nBio [6]. The thesis is centered around the following primary objectives:

1. Validation of TOPAS v3.6 against Geant4 v10.04 [7-9] (used by Lund *et al.*, 2020 [10]):

   Result: All secondary charged particle energy spectra compared well, except for the electron spectra. However, only energy spectra were measured, not the relative dose contributions. This led to an investigation into the cause of the discrepancy in electron spectra.

2. Recognition of TOPAS v3.6 being based on Geant4 v10.06, not Geant4 v10.04 (used by Lund *et al*., 2020 [10]):

   As a result, all simulations were re-performed in Geant4 v10.06.

   Results:

   (i) Several updates and improvements to the hadronic physics models were introduced in the transition from Geant4 v10.04 to v10.06, prompting an investigation into their effects.

   (ii) Issues were identified in the Lund *et al.* (2020) [10] simulations, necessitating further investigations:

   (a) Thermal hydrogen in water was accidentally commented out by Lund *et al.* (2020) [10]. The effects of this omission were analyzed.

   (b) The local approximation condition used by Lund *et al.* (2020) [10] was found to be inappropriate for high-energy electrons. Its impact was examined.

(c) Mismatches in the total dose and relative dose contributions of secondary species were identified due to spherical neutron source dimensions. These effects were evaluated.

3. Estimation of neutron RBE for real-world conditions using TOPAS and TOPAS-nBio.

## 1.5 Overview of this thesis

A brief overview of cancer and its treatment using radiation has been described in Chapter 1. Chapter 2 explores the interaction of radiation with matter, detailing various photon interaction processes. Chapter 3 introduces Monte Carlo techniques, summarizing the tools utilized in this research or forming its foundational basis. Chapter 4 provides background information on radiation biology, including the steps involved in cancer induction following ionizing radiation exposure. The prior foundational work on which this thesis is built has been described in Chapter 5. The methods employed in this study are described in Chapter 6. Chapter 7 presents the results, which are further analyzed and discussed in Chapter 8. Finally, Chapter 9 concludes the thesis, highlighting key findings and suggesting directions for future research.

# Chapter 2

# Radiation Physics

## 2.1 Types of ionizing radiation and their interactions

### 2.1.1 Charged particles

Charged particles interact with atoms of an absorbing medium through Coulomb interactions with either orbital electrons or atomic nuclei as they penetrate the medium. Charged particle interactions can be divided into three categories depending on the size of the impact parameter *b* which is the closest distance between the charged particle trajectory and the center of atomic nucleus compared to the atomic radius *a* of the absorber atom as depicted in Figure 2.1.

#### Soft collisions

A soft collision occurs when the impact parameter *b* of the charged particle trajectory is much larger than the radius *a* of the absorber atom (i.e., $b >> a$). In this case, the charged particle interacts with the whole atom (and its bound electrons). Approximately 50% of the energy lost by a charged particle occurs in soft collisions. However, the energy transfer from a charged particle to an individual bound electron is very small.

#### Hard collisions

A hard collision occurs when the impact parameter *b* of a charged particle trajectory is of the order of radius *a* of the absorber atom (i.e., $b \approx a$). In this case, the charged particle may have a direct Coulomb interaction with a single atomic orbital electron and transfer to it a significant amount of energy. The orbital electron ejects the atom as a δ-ray that is usually energetic enough to undergo its own Coulomb interaction with absorber atoms.

## Radiative collisions

A radiative collision is defined as the Coulomb force interaction of a charged particle with the electromagnetic nuclear field of an absorber atom for $b << a$. The electron passes near the nucleus, an inelastic radiative interaction occurs in which an X-ray photon is emitted. The electron is not deflected in this process but gives a significant fraction ( up to 100%) of its kinetic energy to the photon, slowing down in the process [11]. Such X-rays are referred as bremsstrahlung. A radiative collision is also called a bremsstrahlung collision.

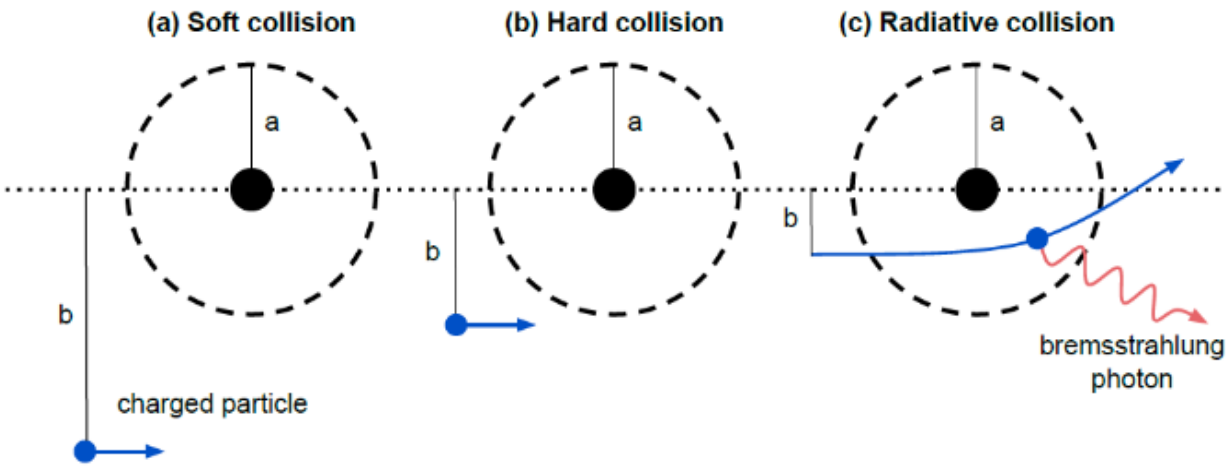


Figure 2.1 Three different types of Coulomb interactions of charged particles with an absorber atom of radius *a* and impact parameter *b*. (a) soft collision where $b >> a$ (b) hard collision where $b \approx a$, and (c) radiative collision where $b << a$. Figure reproduced from Podgoršak (2016) [12].

## Elastic collisions

When the impact parameter of a charged particle is much smaller than the atomic radius ($b << a$), an electron can also scatter elastically and does not emit an X-ray photon or excite the nucleus. It loses a significant amount of kinetic energy necessary to satisfy the conservation of momentum for the collision and deflected from its path.

### Cross-section

In the context of photon interactions, the cross-section is a measure of the probability of interaction occurring between a photon and a target particle, such as an electron in the absorbing material. The cross-section is measured in the units of area, typically in barns ( 1 barn = $10^{-28}$ $m^2$). Larger cross-section values indicate higher interaction probabilities.

## 2.1.2 Photons

This section provides an overview of the various types of interaction that photons of energy exceeding the ionization energy of absorber atoms can have with the absorbing media. The most important interaction processes from a radiotherapy standpoint are described below [12].

### Thomson scattering

Thomson scattering is the process by which an incoming photon can be scattered by an orbital electron. Low energy photons ($h\nu << m_e c^2$) are scattered by loosely bound, i.e., essentially free electrons of an absorber. The electron was assumed to be free to oscillate under the influence of the electric field vector of an incident classical electromagnetic wave then promptly reemit a photon of the same energy. The electron thus retains no kinetic energy as a result of this elastic scattering event.

### Rayleigh scattering

In this interaction, the photon is scattered by the combined action of the whole atom. It is an elastic event in which the photon loses none of its energy and the atom as a whole absorbs the transferred momentum. As a result, the atom is neither excited nor ionized and no dose is absorbed in the medium. The photon is scattered by a small angle with the same energy as the original photon. Rayleigh scattering is prominent mostly at low photon energies and for high atomic number absorbers.

### Compton effect

The Compton effect (Compton scattering) is a phenomenon in which a photon of energy *hv* interacts with a loosely bound electron of an absorber, resulting in transfer of energy

from the photon to the electron. The classical description of the effect assumes that the incident photon interacts with a free or stationary electron. The photon loses part of its energy and changes direction whereas the electron gains energy, which allows it to recoil and be ejected from the atom at an angle *θ*. The photon scatters at an angle *φ* with a new and lower energy *hν'*. The kinematics of Compton interactions can be described by following equations.

$$h\nu' = \frac{h\nu}{1+(\frac{h\nu}{m_0c^2})(1-cos\varphi)} \quad (2.1)$$

where $m_0c^2$ is the rest energy of the electron (0.511 MeV).

The kinetic energy $E_k$ of the recoil electron can be described by Equation 2.2.

$$E_k = h\nu - h\nu' \quad (2.2)$$

The Equation 2.3 relates electron scattering angle θ with photon scattering angle φ.

$$cot\theta = \left(1 + \frac{h\nu}{m_0c^2}\right)\tan(\frac{\varphi}{2}) \quad (2.3)$$

The Compton effect cross-section is independent of the atomic number *Z* of the absorber. It is the primary mechanism by which photons interact with human tissue in the therapeutic energy range.

## Photoelectric effect

In the photoelectric effect, an incident photon of energy *hν* interact with a tightly bound electron such as those in the inner shells of an atom, especially of high atomic number, and gives up all its energy to the electron. In this way, the incident photon is totally absorbed, and the electron is ejected from the material. The photoelectric effect cannot take place unless the energy of the incident photon is greater than binding energy $E_b$ of the electron. The kinetic energy $E_K$ given to the electron is independent of its scattering angle and can be described by the following equation:

$$E_K = h\nu - E_b \quad (2.4)$$

## Characteristic X-rays and the Auger effect

After an atomic vacancy is created, it is filled with an electron from a higher-level atomic shell and the resulting vacancy in the higher-level shell is filled by another even higher shell electron. This process continues until the vacancy migrates to the outer shell of the atom and is filled by a free electron from the material to neutralize the ion. The transition energies are emitted either in form of characteristic X-rays and/or Auger electrons having combined energies equal to the binding energy of the electron that was ejected as the photoelectron.

## Pair production and triplet production

In pair production, a photon disappears and gives rise to an electron and a positron. Pair production can only occur in a Coulomb force field, usually in the presence of a nucleus. The minimum energy required for pair production is 1.022 MeV. This threshold arises because the rest mass energy of an electron or positron is 0.511 MeV; hence, 1.022 MeV is needed to create both particles. However, when a high-energy photon interacts directly with an atomic electron, instead of a nucleus, an electron-positron pair is produced, and the original electron is ejected from its atomic shell. This results in three charged particles: the ejected atomic electron and the newly formed electron and positron. The probability of triplet production is lower than pair production. A minimum photon energy of $4m_0c^2$ = 2.044 MeV is required for triplet production because of momentum-conservation considerations.

## Photonuclear reaction

The photoneuclear reaction is a direct interaction between an energetic photon and an absorber nucleus causing nuclear disintegration. In this interaction the nucleus absorbs a photon and most likely emits a single neutron through a (γ,n) reaction or less likely protons, α particles, γ-rays, or fission fragments. Being an endothermic reaction, the incident photon must possess minimum energy. The threshold energy for the photonuclear reaction (energy required to separate a neutron from the nucleus) is of the order of 8 MeV or more for most nuclei, except for the deuteron and beryllium, for which

it is lower [11]. (γ,n) interactions have a practical importance in radiotherapy because the neutrons thus produced may lead to problems in radiation protection.

### 2.1.3 Neutrons

## Quarks and Gluons

Quarks are elementary particles and fundamental building blocks of matter. There are six flavors of quarks: up, down, charm, strange, top, and bottom. Quarks are never observed in isolation; they combine to form particles called hadrons.

Gluons are elementary particles that act as the force carriers for the strong nuclear force. They mediate the interaction between quarks, binding them together to form hadrons (e.g., protons and neutrons)

## Neutrons

Neutrons, being electric charge neutral, are indirectly ionizing radiation that can penetrate deep into materials. It is made up of two down quarks and one up quark (udd). They deposit dose through a two-step process. First neutrons transfer energy to heavy charged particles and then those heavy charged particles deposit energy in the absorber through Coulomb interactions. Neutrons may undergo a variety of reactions including elastic and inelastic scattering, nuclear capture, spallation, and fission. Neutrons are classified based on their kinetic energy into several categories listed in Table 2.1.

### Neutron elastic scattering

Neutrons interact via the strong nuclear force, which acts at very short distances (~1 femtometer). Since no Coulomb repulsion exists, neutrons can approach the nucleus more closely. In this process, the total kinetic energy and momentum of the neutron and nucleus system is conserved, although energy is redistributed between the two particles after the collision. While charged particles like protons or alpha particles scatter primarily through the Coulomb force, interacting with the electric field surrounding the nucleus causing them to be significantly deflected by the electrostatic repulsion.

During elastic scattering, if the target nucleus is hydrogen, then the neutron transfers on average half of its initial kinetic energy to the proton, which further transfers its kinetic energy to the medium through Coulomb interactions. On the other hand, if the target nucleus' mass is much larger than neutron's mass then the energy transfer is less efficient. Only 2% fractional energy is transferred from a neutron to a lead nucleus in head-on collision, which has implications for shielding against neutron radiation in high-energy linear accelerator installations.

Table 2.1 Classification of neutrons based on their kinetic energy [12].

| Category | Kinetic energy range |
|---|---|
| Ultracold neutrons | $E_K < 2 \times 10^{-7}$ eV |
| Very cold | $2 \times 10^{-7}$ eV ≤ $E_K$ ≤ $5 \times 10^{-5}$ eV |
| Cold neutrons | $5 \times 10^{-5}$ eV ≤ $E_K$ ≤ 0.025 eV |
| Thermal neutrons | $E_K$ ~ 0.025 eV |
| Epithermal neutrons | 1 eV ≤ $E_K$ ≤ 1 keV |
| Intermediate neutrons | 1 keV ≤ $E_K$ ≤ 0.1 MeV |
| Fast neutrons | $E_K$ > 0.1 MeV |

## Inelastic scattering

Inelastic scattering of neutrons is a type of neutron interaction with a nucleus where the neutron is first captured by the nucleus and then re-emitted as a neutron with a lower energy. The excited nucleus then de-excites by emitting high-energy γ-rays. Unlike elastic scattering, inelastic scattering results in a loss of kinetic energy in the neutron-nucleus system, as some energy is used to excite the nucleus. This type of interaction becomes significant when neutron energies are relatively high, typically in the range of several MeV or higher.

## Neutron capture

Neutron capture occurs when a neutron is absorbed by a nucleus, forming a heavier isotope. The excited nucleus then releases excess energy by emitting γ-rays or a proton.

The neutron capture cross-section is highest for slow (thermal) neutrons with energies around 0.025 eV and follows the 1/v law. This means that the cross-section is inversely proportional to the velocity of the thermal neutron and follows a $1/\sqrt{E}$ dependence on energy for thermal neutrons. In medical physics, neutron capture is used in nuclear reactors to produce cobalt-60 sources for radiotherapy and iridium-192 sources for brachytherapy.

### Neutron-induced fission

When high atomic number nuclei ($Z \geq 92$) are bombarded by thermal or fast neutrons, the target nucleus fragments into two daughter nuclei of lighter mass along with the production of several fast neutrons. Under the right conditions, released neutrons from each fission event can strike other fissile nuclei leading to further fission events in a self-sustaining process known as a chain reaction.

### Nuclear spallation

Nuclear spallation is defined as the disintegration of a target nucleus into many small residual components such as protons, neutrons and α-particles upon bombardment with a suitable projectile such as high-energy neutrons (typically above 100 MeV) or light or heavy ion beams. Most of the energy released in nuclear spallation is carried away by the heavier fragments that deposit energy locally whereas neutrons and γ-rays produced through de-excitation carry energy further away.

## 2.2 Quantities and concepts related to ionizing radiation

### Stopping power

As a charged particle passes through a medium, it experiences many interactions and loses energy. The rate of energy loss (dE) per unit path length (dx) by a charged particle in an absorbing medium is called linear stopping power ($-dE/dx$). Dividing the linear stopping power by the density ρ of the absorber results in the mass stopping power $S/\rho$. Two types of stopping power can be defined based on the charged particle interaction involved: (i) Radiation stopping power, caused by Coulomb interactions with the nuclei of the absorber. (ii) Collision stopping power, caused by Coulomb interactions with the orbital

electrons of the absorber. For protons, α-particles and other heavy charged particles, the radiation loss is negligible whereas light charged particles (electrons and positrons) experience appreciable energy loss. The total stopping power $S_{tot}$ for a charged particle travelling through an absorber is the sum of radiation stopping power and collision stopping power.

$$S_{tot} = S_{rad} + S_{col} \tag{2.5}$$

In medical physics, restricted collision stopping power is often used to know local energy deposition. It is calculated similarly to the collision stopping power by excluding the energy transfer to δ-rays greater than some upper threshold.

## Linear energy transfer

The linear energy transfer (LET) $L_{\Delta}$ is defined as the mean amount of energy that a given ionizing radiation imparts to an absorbing medium (such as tissue) per unit length. It is identical to the restricted stopping power, except the energy threshold (Δ) is set on the kinetic energy of δ-rays rather than the total amount of energy transferred [13]. LET is of great relevance in radiobiology and microdosimetry. Stopping power describes the total energy loss per unit distance, including all types of energy deposition by a particle in a medium whereas LET represents the energy that directly contributes to ionization and excitation in the medium, which is more relevant in accessing biological damage.

## Absorbed dose

The quantity absorbed dose is the ratio of the mean energy imparted by ionizing radiation per unit mass of matter. The SI unit of absorbed dose is $J.kg^{-1}$ and the special unit is gray (Gy) where 1 Gy = 1 $J.kg^{-1}$ [12].

## Lineal Energy

Lineal energy (y) is a microdosimetric quantity defined as the energy imparted to a target volume per unit mean chord length of that volume. Mathematically, it is expressed as:

$$y = \frac{\varepsilon}{\bar{l}} \tag{2.6}$$

where ε is the energy imparted in a single event, and $\bar{l}$ is the mean chord length of the target volume. It is measured in units of keV/μm.

While absorbed dose represents the macroscopic energy deposited per unit mass, lineal energy characterizes energy deposition on a microscopic scale, relevant for understanding radiation interactions at the cellular and subcellular levels. Unlike absorbed dose, which averages energy deposition over a large volume, lineal energy accounts for the stochastic nature of energy deposition in small structures, making it particularly useful for linking radiation quality to biological effects.

## Equivalent dose

Equivalent dose is a radiation protection quantity that accounts for the type and quality of radiation exposure to human tissue. The International Commission on Radiological Protection (ICRP) defines equivalent dose $H_T$ which, for a particle tissue or organ T, is the sum of the mean absorbed dose to the organ or tissue as a result of radiations of different types R, each multiplied by an appropriate radiation weighting factor $W_R$.

$$H_T = \sum_R W_R D_{T,R} \tag{2.7}$$

The SI unit of the equivalent dose is the sievert (Sv). Table 2.2 lists the ICRP's most recent recommendations for radiation weighting factors. The radiation weighting factors are based upon the RBE of the various radiations for stochastic effects at low doses and upon judgment of the ICRP.

Table 2.2 Radiation weighting factors, $W_R$, as recommended by the ICRP [14].

| Radiation | Energy (MeV) | $W_R$ |
|---|---|---|
| Photons | all | 1 |
| Electrons and muons | all | 1 |
| Neutrons | 0.01 MeV to >20 MeV | 5-20 |
| Protons (other than recoil protons) | E ≥2 | 2 |
| Alpha particles and heavy ions | all | 20 |

## Effective dose

To account for the variation in radiation sensitivity among the tissues and organs of the body, the quantity effective dose E was defined by the ICRP. The effective dose is defined as the sum of equivalent doses to exposed tissues and organs multiplied by the appropriate tissue weighting factor $W_T$.

$$E = \sum_T W_T H_T \tag{2.8}$$

The SI unit of effective dose is also the sievert. Table 2.3 lists the ICRP's most recent recommendations for tissue weighting factors. The sum of all tissue weighting factors is unity for the whole body. Organs with higher radio-sensitivity are assigned higher tissue weighting factors.

Table 2.3 Tissue weighting factors $W_T$, as recommended by the ICRP [14].

| Tissue | $W_T$ |
|---|---|
| Gonads | 0.20 |
| Bone marrow | 0.12 |
| Colon | 0.12 |
| Lung | 0.12 |
| Stomach | 0.12 |
| Bladder | 0.05 |
| Breast | 0.05 |
| Liver | 0.05 |
| Oesophagus | 0.05 |
| Thyroid | 0.05 |
| Bone surface | 0.01 |
| Skin | 0.01 |
| Remainder of the body | 0.05 |
| Whole body (sum of all organs) | 1.0 |

# Chapter 3

# Monte Carlo Simulations

The Monte Carlo method was formally developed during the Manhattan Project in the 1940s, which aimed to create the first nuclear weapons [15]. Its earliest significant application was in neutron transport simulations, where scientists used it to predict how neutrons would scatter and interact with materials in a nuclear reactor or bomb. Monte Carlo techniques have long been used in medical physics to model the transport and detection of ionizing radiation. Three of the most used Monte Carlo codes in medical physics are Geant4, MCNP [16], and EGSnrc [17]. Among other Monte Carlo codes being used for specific medical physics problems, there are more user-friendly interfaces and wrappers that simplify the use of the above-mentioned codes. These include TOPAS for Geant4, TOPAS-nBio for Geant4-DNA [18-21], and BEAMnrc [22] and DOSXYZnrc [23] for EGSnrc. Using Monte Carlo, the response of a radiation detector in a particular experiment can be predicted for direct comparison with experimental data. In this chapter, a brief description of the usability of Monte Carlo codes in radiation transport simulations, the types of Monte Carlo simulation techniques, along with an overview of existing Monte Carlo codes used in this thesis are provided.

## 3.1 Radiation transport simulation with Monte Carlo

## 3.2 Condensed-history simulations

In the condensed-history (CH) approach, instead of simulating each interaction, particle transport is simulated by grouping multiple scattering events into single “steps” or “sub-steps”. CH is specifically applied to charged particles because of the sheer number of interactions they undergo as they travel through matter. Unlike neutral particles, which typically have fewer and more distinct interactions, charged particles experience continuous and frequent collisions with atoms and electrons. CH simulation divides a particle’s path into segments, where each segment represents the cumulative effect of multiple interactions. In each segment, the model calculates a net change in particle

energy, direction, and position based on statistical methods, rather than calculating each small interaction separately. This approach is particularly useful in situations where individual microscopic interactions are not critical such as in dosimetry. CH is fast as it reduces the number of interactions that need to be simulated. However, the CH technique is not ideal in biological applications and microdosimetry since it averages effects over large steps and cannot capture the precise spatial patterns of energy depositions.

## 3.3 Track-structure simulations

The track-structure (TS) approach is also known as event-by-event Monte Carlo as it models each individual interaction a particle undergoes along its path. A TS simulation tracks particles as they interact with the medium accounting for each energy loss event, scatter event, and change in particle trajectory. The simulation generates a “track structure” that depicts each interaction’s location and nature in three-dimensional space. TS is ideal for studying DNA damage in biological cells from radiation exposure. TS simulations are computationally intensive and are generally feasible only for low-energy particles (e.g., electrons, protons, or ions up to a few MeV).

## 3.4 Existing Monte Carlo simulation toolkits

Out of several Monte Carlo simulation codes available, we chose TOPAS for CH simulations and TOPAS-nBio for TS biological simulations in this thesis project. As the first objective of this project (see section 1.4) was to replicate the Lund *et al.* (2020) [10] work in Geant4, which involved the generation of the secondary charged particles’ energy spectra and relative dose contributions in the ICRU sphere phantom [24], we used TOPAS which is a wrapper of Geant4. The second objective of this project was accomplished using TS simulations in our DNA model, built in TOPAS-nBio, to estimate secondary neutron RBE. Both TOPAS and TOPAS-nBio are open source align with our lab’s policy to develop software packages in an open-science framework.

### 3.4.1 Geant4

Geant4 (Geometry and Tracking 4) is a powerful open-source toolkit developed primarily by the European Council for Nuclear Research (CERN). It is a widely used simulation

toolkit used for simulating the passage of particles through matter in high-energy physics, medical physics, radiation shielding, and space science applications. It uses object-oriented technology and is implemented in the C++ programming language. It has a large set of physics models to handle the interactions of particles with matter across a wide energy range along with other functionality including tracking, geometry, and hits. Users can simulate interactions like ionization, bremsstrahlung, Compton scattering, and nuclear interactions. Geant4 allows users to define complex and customizable 3D geometries. The strength of Geant4 is its extensive flexibility, with classes and tools for customizing every aspect of a simulation, from geometry and materials to primary particle sources and physics lists, which leads to its complexity. Geant4 has a powerful user interface, including command-line and macro capabilities to control simulations. It also supports various visualization drivers, allowing users to view particle trajectories and geometries. In medical physics, Geant4 is widely used for radiation therapy planning, imaging, dosimetry, and studying radiation effects on biological tissues.

### 3.4.2 Geant4-DNA

Geant4-DNA is an extension of the Geant4 toolkit used for biological research that was released publicly in Geant4 version 9.1 in 2007. It is designed for simulating interactions of particles with biological matter at very low energies. Geant4-DNA is fully included in Geant4 and uses the same framework. It was developed to study radiation effects at the cellular and sub-cellular scale. Geant4-DNA includes detailed models for simulating the interactions of low-energy electrons, protons, and other particles with biological materials. These interactions are essential for studying radiation effects where traditional Geant4 models are not applicable. It models direct DNA damage caused by ionizing radiations as well as indirect damage from reactive species like hydroxyl radicals, which are produced through water radiolysis in irradiated tissue as biological tissues are largely composed of water. Geant4-DNA allows users to model geometries at the nanometric scale, such as DNA double-helix structure and sub-cellular components. This fine level of detail helps simulate particle tracks and radiation interactions within a DNA model. Being an extension of Geant4, Geant4-DNA benefits from the comprehensive infrastructure of Geant4, including its geometry, material, and particle tracking capabilities. It also leverages

Geant4's flexibility, allowing for customized simulations that integrate both Geant4-DNA's low-energy processes and Geant4's broader high-energy physics models for more complex simulations across multiple scales.

### 3.4.3 TOPAS

TOPAS (Tool for Particle Simulation) is a Monte-Carlo based simulation platform developed to make the power of Geant4 accessible to researchers, particularly in medical physics, radiation therapy and particle therapy. It wraps and extends Geant4 to create a user-friendly tool as shown in Figure 3.1. TOPAS includes the standard Geant4 toolkit, and it evolves as Geant4 evolves. TOPAS allows users to set up simulations through text-based parameter files rather than C++ code. In TOPAS, simulation parameters can be defined in the parameter file without requiring a specific line order, reducing the potential for user error. This flexibility helps ensure accurate simulation configuration. TOPAS supports a variety of pre-defined geometries, such as spheres, cubes, and cylinders, or more complex anatomical phantoms, including voxel-based representations of patient CT scans. Researchers can model treatment rooms, equipment (like linear accelerators and gantries), and patient-specific phantoms, making it ideal for clinical treatment planning studies. TOPAS scorers have additional capabilities beyond Geant4 and provide options to report mean, variance, max etc. along with many filters applied to scoring quantities. It can also handle time-dependent quantities such as component motion, beam current modulation, electric and magnetic fields. TOPAS is modular, allowing users to combine components, such as detectors, beams, and geometries, easily and intuitively.

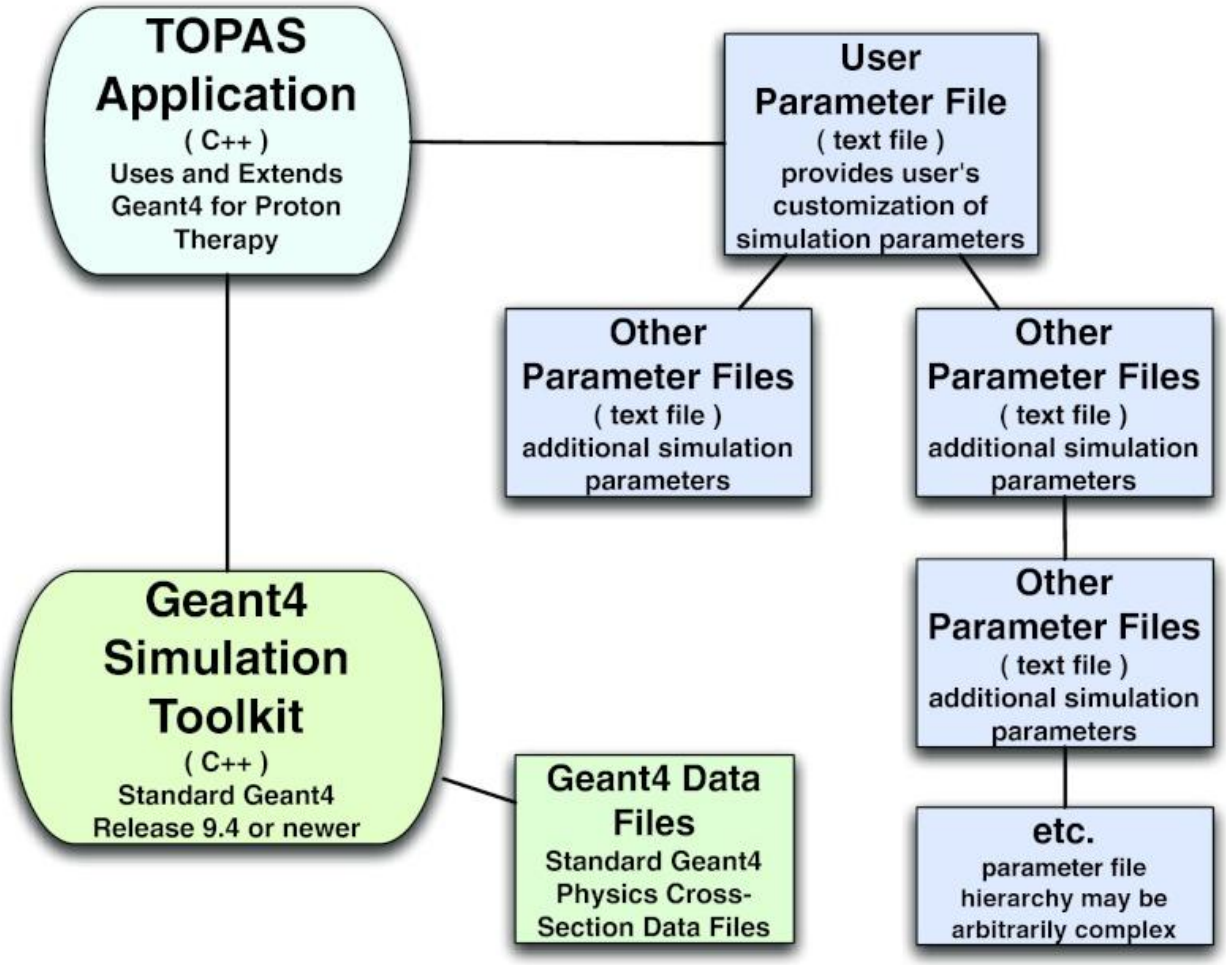


Figure 3.1 TOPAS parameter control system. The user needs to write a parameter file which is a simple text file that controls the simulation. Figure from Perl *et al.* (2012) [5].

### 3.4.5 TOPAS-nBio

TOPAS-nBio is an extension of TOPAS, specifically designed to enable the simulation of radiation interactions at the nanoscale level. It is based on Geant4-DNA. TOPAS-nBio offers full track-structure Monte Carlo simulations. It extends TOPAS to model radiobiological experiments. By default, TOPAS-nBio provides a library of pre-defined biological structures, including nuclei, chromosomes, chromatin fibers, and even detailed DNA models. This allows users to simulate radiation interactions with biological structures realistically, tracking how radiation impacts them at the nanometer scale. A variety of specialized cell geometries as well as sub-cellular structures such as DNA and mitochondria are available in TOPAS-nBio. It also offers integration of chemical reactions

and interfaces to mechanistic models of DNA repair kinetics. The latest version, TOPAS-nBio v3.0, has been released recently which has pre-built a new second cancer model, a new mesh phantom model for mice and imaging extension to allow modelling of basic CT, SPECT, and PET imaging detectors [25].

# Chapter 4

# Radiobiology

## 4.1 The cell

Cells are the fundamental units of life, and most contain DNA, which encodes the genetic instructions required for their function, replication, and response to environmental stimuli. In human cell (i.e. eukaryotic cells) the nucleus houses DNA in the form of tightly coiled chromosomes, which are made up of double-stranded DNA molecules. In prokaryotic cells, DNA is not enclosed in a nucleus but is instead found in a nucleoid region. The integrity of DNA is essential for cell survival and function, as it directs protein synthesis, cellular repair, and regulatory processes necessary for maintaining health [2]. The most of the radiobiology information used in this chapter is taken from Hall and Giaccia (2012) [2].

## 4.2 Radiation toxicity

When cells are exposed to ionizing radiation - such as X-rays, γ-rays, or particle radiation (protons, neutrons, or α-particles) - the energy from the radiation can ionize atoms within the cell. This ionization process leads to the formation of free radicals, primarily through interactions with water molecules in the cell.

Radiation can induce many lesions in DNA including single-strand breaks (SSBs), double-strand breaks (DSBs), and base lesions, most of which are repaired successfully by the cell. An SSB occurs when the phosphate-sugar backbone of one strand of the DNA double helix is broken, but the complementary strand remains intact. By contrast, if two SSBs are opposite one another or separated by only a few base pairs, this can lead to a DSB. After a dose of 1 Gy of X-rays, approximately 1,000 SSBs and 40 DSBs can be observed [2]. Usually, SSBs are of little biological consequence as far as cell killing is concerned because they are easily repaired. However, if a misrepair occurs, it may result in a mutation. In contrast, DSBs are considered the most critical lesions caused by

radiation in chromosomes. The interaction of two DSBs may result in cell death, carcinogenesis, or mutation [2].

## 4.3 Relative Biological Effectiveness

When comparing the biological effects of different types of radiation, 250 keV X-rays are typically used as reference radiation. In 1954, the National Bureau of Standards defined relative biologic effectiveness (RBE) [26] as follows:

The RBE of some test radiation (r) compared with X-rays is defined by the ratio $D_{250}/D_r$, where $D_{250}$ and $D_r$ are, respectively, the doses of X-rays and the test radiation required for equal biological effect.

To measure the RBE of a particular radiation, a biological system is selected in which the effects of the radiation can be measured quantitatively.

While this classical definition of RBE relies solely on absorbed dose, it does not account for differences in radiation quality, particularly the spatial distribution of energy deposition at the microscopic level. A more refined approach to RBE considers lineal energy as a surrogate for radiation quality. Lineal energy describes the stochastic nature of energy deposition at cellular and subcellular scales, making it a more biologically relevant descriptor of radiation damage. Since microdosimetric dose mean lineal energy ($\bar{y}_D$) is strongly correlated with biological damage, it is served as RBE predictor.

## 4.4 Chromosomes and the DNA molecule

DNA is the primary target for the biological effects of radiation, such as cell killing, carcinogenesis, and mutation [2]. Therefore, to understand the biological impact of radiation it is important to consider the structure of the DNA molecule.

### 4.4.1 Structure of the DNA molecule

Deoxyribonucleic acid (DNA) is a large molecule with a characteristic double-helix structure (Figure 4.1). It consists of two strands joined by hydrogen bonds between complementary bases. Each strand has a "backbone" composed of alternating sugar (deoxyribose) and phosphate groups. Four nitrogenous bases are attached to this

backbone, and their sequence encodes the genetic information. The bases are classified as either single-ring structures (pyrimidines: thymine and cytosine) or double-ring structures (purines: adenine and guanine) [2]. For the DNA strands to pair correctly, the bases must be complementary: adenine pairs with thymine, and guanine pairs with cytosine.

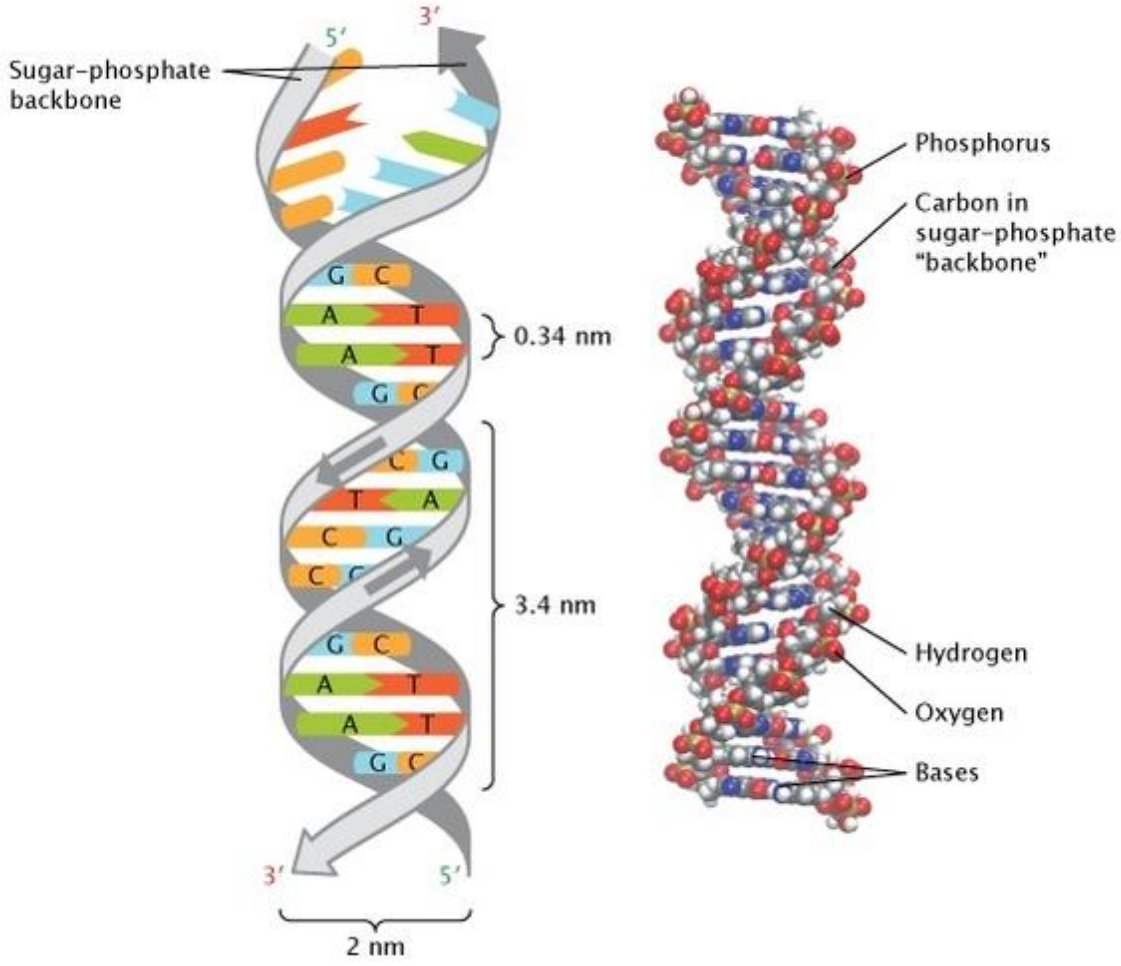


Figure 4.1 The DNA double helix structure. The two strands are held together by hydrogen bonds between base pairs. Figure from Pray *et al.* (2008) [27].

## 4.5 Ionizing radiation and DNA damage

### 4.5.1 Low LET vs High LET

Depending on the density of ionization events created by different types of ionizing radiation as they pass through biological tissue or other materials, the ionizing radiations can be categorized into low LET and high LET as described below.

Low LET radiation refers to ionizing radiation that deposits energy sparsely along its path. Examples of low LET radiation are X-rays, γ-rays, and high-energy electrons. Their LET values are generally under 10 keV/μm. These types of radiation cause fewer ionizations per unit mass of tissue, resulting in a dispersed energy distribution. While low LET radiation is less likely to cause complex damage, it can still lead to significant biological effects, especially at high doses.

High LET radiation deposits energy densely along its path, resulting in clusters of ionizations in a small area. Examples of high LET radiation are α-particles, protons, neutrons, and heavy ions. Their LET values are generally above 10 keV/μm and can exceed hundreds of keV/μm, depending on the particle and its energy. High LET radiation produces many ionizations in proximity, leading to concentrated energy depositions. High LET radiation often causes double-strand breaks (DSBs) in DNA, which are difficult for cells to repair, resulting in higher cell-killing efficiency. It can also cause complex DNA damage, including clusters of breaks and base damage that can overwhelm cellular repair mechanisms.

### 4.5.2 Direct vs Indirect action

When ionizing radiation penetrates matter, it can ionize or excite atoms of the absorbing medium initiating a chain of events leading to biological damage. For high LET radiation (such as neutrons or α-particles), the dominant process is direct action radiation damage. In direct action, the atoms of the target itself may be ionized or excited, thus initiating the chain of events that leads to a biologic change ( see Figure 4.2). Since the damage is immediate and localized, direct action can lead to clustered DNA damage that is challenging for cellular mechanisms to fix. In indirect action, the radiation may interact

with other atoms or molecules in the cell producing hydroxyl radical (OH◦) which then chemically damages the DNA. A free radical is a short lived ($10^{-10}$ seconds) highly reactive species that carries unpaired orbital electrons in the outer shell. It can diffuse up to twice the diameter of DNA double helix [2]. In general, about two-thirds of the X-ray damage to DNA in mammalian cells is caused by hydroxyl radical [2].

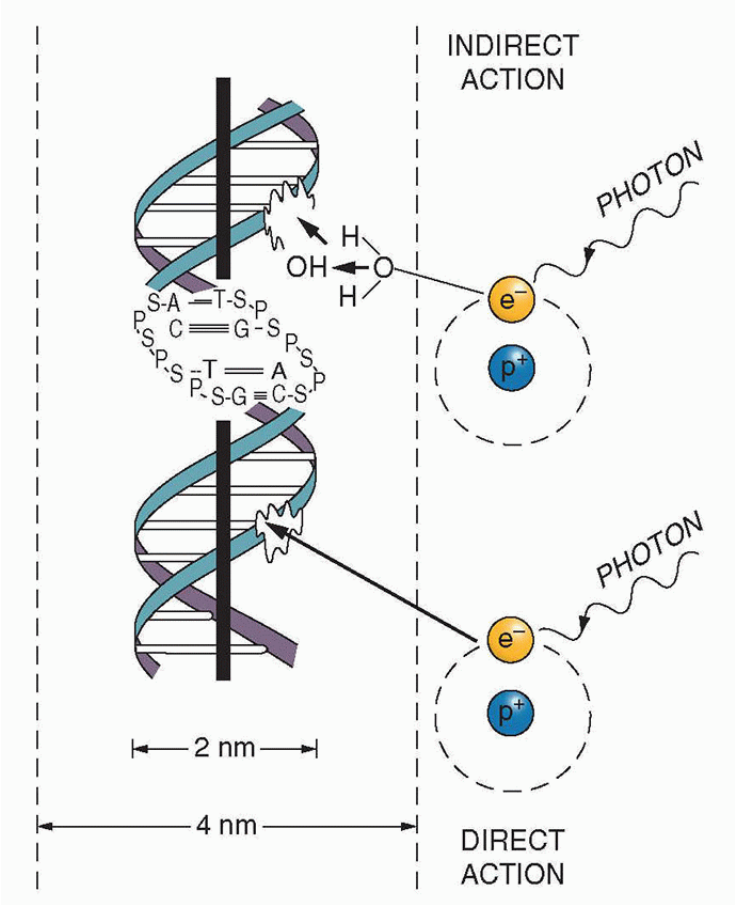


Figure 4.2 Direct vs indirect action radiation damage. In direct action, the ionizing radiation interacts with and damages the cell's DNA without creating chemical species whereas in indirect action, the first step is water radiolysis creating highly reactive free radicals that subsequently damage DNA. Figure from Hall and Giaccia [2].

### 4.5.3 Complex DSB clusters

DSBs are the most important lesions induced by ionizing radiations in DNA. There are many types of DSBs according to the distance between the breaks on the two DNA strands. Complex DSB clusters (see Figure 4.3) are regions in DNA where multiple DNA lesions are closely grouped within a short distance, typically involving DSBs alongside other types of damage, such as SSBs or base lesions. These clusters are often referred to as complex DSB clusters due to the difficulty in accurately repairing them. Complex DSB clusters are particularly relevant in the context of high linear energy transfer (LET) radiation, such as that from heavy ions or α-particles, which deposit energy densely along their tracks.

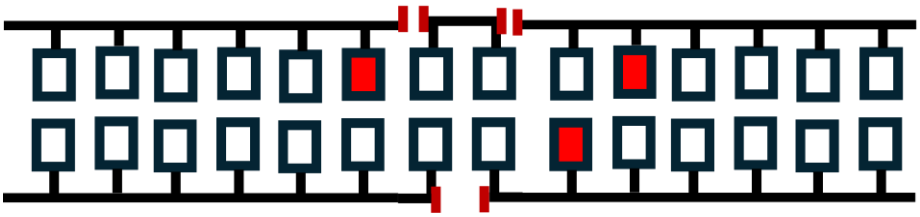

Figure 4.3 Schematic example of a complex DSB cluster containing two or more damage sites, including at least one DSB, each within 40 base pairs of each other [28].

# Chapter 5

# Prior Foundational Work

This chapter presents an overview of the prior foundational work and existing Geant4-based simulation pipeline developed by the Neutron-Induced Carcinogenic Effects (NICE) research group [29] at Kildea Lab [30]. The NICE research group aims to exploit the energy-dependence of the neutron radiation weighting factors for stochastic effects to help explain the biophysics of radiation-induced carcinogenesis [30].

## 5.1 Previous work on neutron RBE as a function of energy

Baiocco *et al.* (2016) [31] aimed to investigate the variation of neutron RBE with neutron energy as part of the European ANDANTE project [32]. The ANDANTE project sought to evaluate neutron RBE for different tissues and neutron energies by integrating findings from three key fields: physics, stem cell radiobiology, and epidemiology.

Baiocco *et al.* (2016) developed two distinct energy-dependent neutron RBE models. The first model utilized the condensed-history Monte Carlo code PHITS (Particle and Heavy Ion Transport Code) [33], where an ICRU44 soft tissue [24] spherical phantom of radius 15 cm was isotropically irradiated with monoenergetic neutrons ($E_n$) ranging from 10 eV to 1 GeV. Three scoring volumes, each with a radius of 1.5 cm, were placed at varying radial depths of 0 cm, 7.5 cm, and 13.5 cm from the phantom's center to capture the spectra of secondary species produced by neutron interactions with phantom material. A microdosimetric quantity, dose mean lineal energy ($\bar{y}_D$), was used to estimate neutron RBE for each scoring volume placed inside the phantom. The microdosimetric quantity, $\bar{y}_D$, characterizes the stochastic energy deposition by radiation at the microdosimetric (cellular and sub-cellular) scale of interest. The $\bar{y}_D$ values were calculated for all secondary particle tracks associated with each initial neutron energy and tracks of the secondary particles generated from reference X-rays (220 keV) in each scoring volume. The estimated neutron RBE in each scoring volume was simply a ratio of $\bar{y}_D$ value for each initial neutron energy and the $\bar{y}_D$ value for 220 keV X-rays.

The second model involved track structure simulations using the PARTRAC [34, 35] Monte Carlo code. Here, the secondary species spectra of carbon, nitrogen, oxygen nuclei, electrons, protons, deuterons, and α-particles recorded in PHITS simulations were used to perform single-cell irradiations. The neutron RBE for each initial neutron energy was determined by comparing the yields of DNA damage clusters, defined as the number of lesions containing at least two double-strand breaks (DSBs) within 25 base pairs (also labeled as DSB++ [31]), to those induced by reference X-rays (220 keV) in each scoring volume. The neutron RBE results using the models are depicted in Figure 5.1. Baiocco *et al.* (2016) connected real-world neutron RBE for stochastic effects to fundamental microdosimetry quantities and biophysical mechanisms.

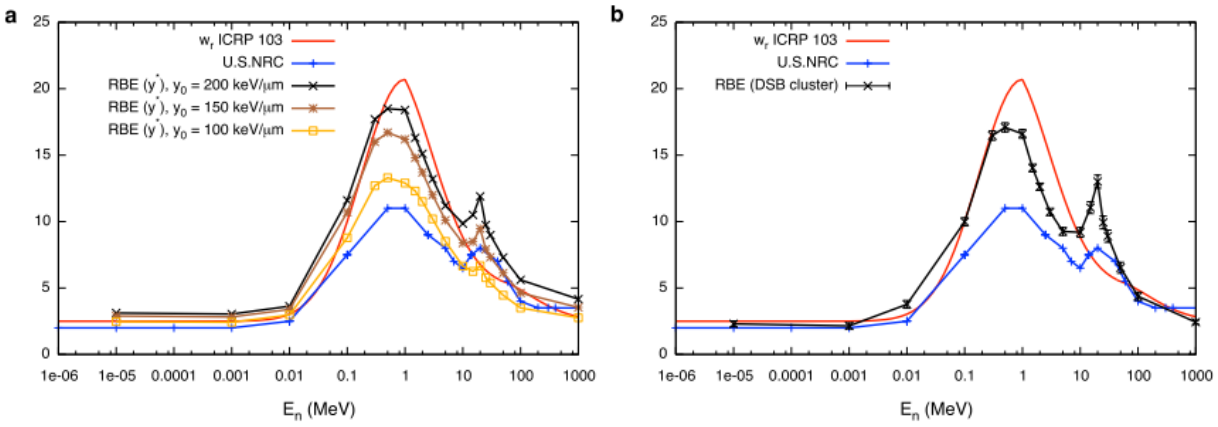


Figure 5.1 Model results for neutron RBE as a function of their energy developed by Baiocco *et al.* (2016) [31]. (a) Model 1: microdosimetric model of neutron RBE as a function of energy for the outer scoring volume. Neutron RBE calculated as a ratio of dose-mean lineal energies for different value of saturation parameter ($y_0$) (b) Model 2: neutron RBE for inducing DSB clusters (black crosses) in the outer scoring volume.

## 5.2 Overview of our existing NICE simulation pipeline

This thesis is built upon the previous work done by our research group, which is described below.

### 5.2.1 Neutron RBE estimation in the ICRU sphere phantom

The secondary species spectra associated with the initial neutron energies and the codes developed by Baiocco *et al.* (2016) for neutron RBE modeling were not open source. This lack of accessibility motivated Lund *et al.* (2020) [10] from our group to develop a model similar to the first model of Baiocco *et al.* (2016) in the open-source Monte Carlo framework: Geant4 and its radiobiological extension Geant4-DNA. Consistent with the Baiocco *et al.* (2016) study, to investigate neutron RBE as a function of energy, Lund *et al.* (2020) [10] also used $\bar{y}_D$ as an RBE proxy.

## Geometry

To simulate neutron interactions, a flat spectrum of neutrons (uniform energy spectrum), spanning 18 monoenergetic neutron energies from 1 eV to 10 MeV, was used to irradiate a tissue-equivalent sphere phantom modeled according to the specifications the International Commission on Radiation Units and Measurements (ICRU) for dosimetric and radiation safety applications [24]. The ICRU-4 sphere, composed of oxygen, carbon, hydrogen, and nitrogen, has a diameter of 30 cm, roughly the size of a human torso. The phantom was centrally positioned within a sphere with a diameter of 40 cm, referred to as the “world”, composed of a vacuum. This outer sphere served as the neutron source, irradiating the ICRU sphere isotropically. Consistent with the Baiocco *et al.* (2016) study, three scoring volumes, each with a radius of 1.5 cm made of the same tissue-equivalent material were placed at radial depths of 0 cm, 7.5 cm, and 13.5 cm along a single axis within the phantom (see Figure 5.2). These volumes were referred to as the inner, intermediate, and outer scoring volumes respectively.

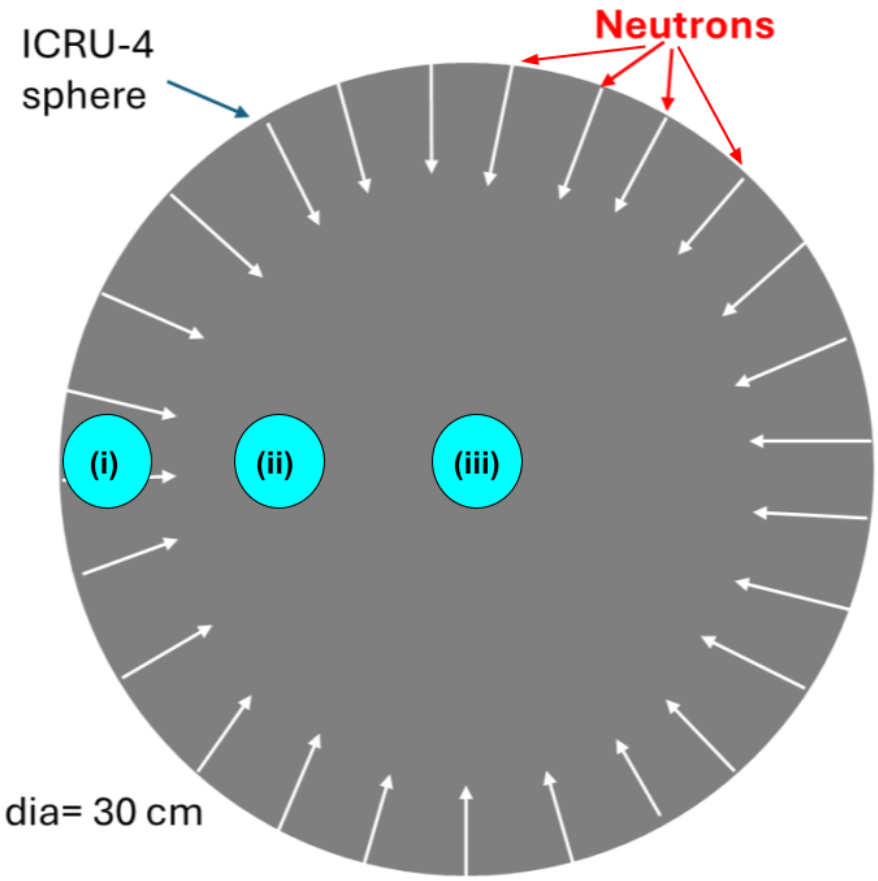


Figure 5.2 ICRU-4 sphere (shown in grey color) phantom [24] geometry used in condensed history simulations. Three scoring volumes: (i) outer (ii) intermediate, and (iii) inner were placed at various radial depths in the phantom. A spherical surface source of diameter 40 cm (not shown here) was placed externally to the phantom served as a source of neutrons (shown in white) emitting them inwards towards the phantom.

## Physics Settings

In Geant4, condensed-history simulations were performed to record the spectra of secondary species in each scoring volume produced by neutron interactions with the phantom's material. The G4HadronPhysicsQGSP_BIC_HP physics list was employed for high-precision hadronic simulations. This list incorporates the Quark-Gluon String (QGS) model, the Binary Cascade (BIC) model, and High Precision (HP) neutron models and cross-sections [36]. These models effectively describe elastic and inelastic scattering, as well as capture and fission reactions for neutrons with energies up to 20 MeV.

Additionally, the G4ParticleHPThermalScattering class is used to accurately simulate the transportation of thermal neutrons, specifically handling scattering events for low-energy neutrons, particularly those with energies below a few eV. For electromagnetic interactions, the G4EmLivermorePhysics model was utilized. This model is based on the Livermore data libraries [37-39], offering detailed cross-section and interaction models for photons, electrons, and positrons down to very low energies, including a few eV. The processes covered by this model include the photoelectric effect, Compton scattering, pair production, bremsstrahlung, ionization, and multiple scattering.

In addition to these primary models, default physics processes were used to manage interactions of lesser significance. G4Stopping is employed for the stopping (absorption) of slow hadrons (such as protons, neutrons, and pions) in matter. G4Decay simulates the decay of unstable particles, while G4RadioactiveDecay handles the decay of radioactive nuclei.

## Scoring

In the first stage, all secondary species produced by neutrons including protons, deuterons, tritons, α-particles, and various ions (beryllium, boron, carbon, nitrogen, and oxygen), were recorded within the scoring volumes utilizing condensed-history simulation approach (see Figure 5.3 (a)). A local approximation condition was applied for heavier charged particles, equating the absorbed dose to electronic kerma. This approximation is valid for neutron fields up to 20 MeV in human tissue due to the short range of resulting heavy ions and the minimal radiative losses involved. Specifically, heavy ions lose a relatively small fraction of their kinetic energies to characteristic X-rays and bremsstrahlung, making the approximation of neutron dose being equivalent to electronic kerma more accurate in this neutron energy range. Under this approximation, all secondary charged particles (excluding protons and electrons) were stopped at their point of generation and their energy was deposited locally. Their initial kinetic energy was obtained using the PreStepKineticEnergy function in Geant4. Protons were allowed to continue interacting freely with the material and were tracked until their energies dropped to 0 eV. Electrons with kinetic energies below 1 MeV, whether produced within the scorer or originating elsewhere in the geometry and passing through the scorer, were

immediately stopped and recorded. High-energy electrons, with kinetic energies above 1 MeV, were transported until a cut-off of 1 MeV. At this point, they were stopped, and their energy depositions were recorded. For each scoring volume, the particle spectra were binned into 500 logarithmically spaced energy intervals ranging from 1 eV to 10 MeV. The relative dose contribution of each secondary particle was calculated by dividing the total dose deposited by all particles by the dose deposited by each specific particle (Figure 5.3 (b)). For each primary neutron energy, approximately $10^{10}$ neutrons were simulated to ensure statistical accuracy.

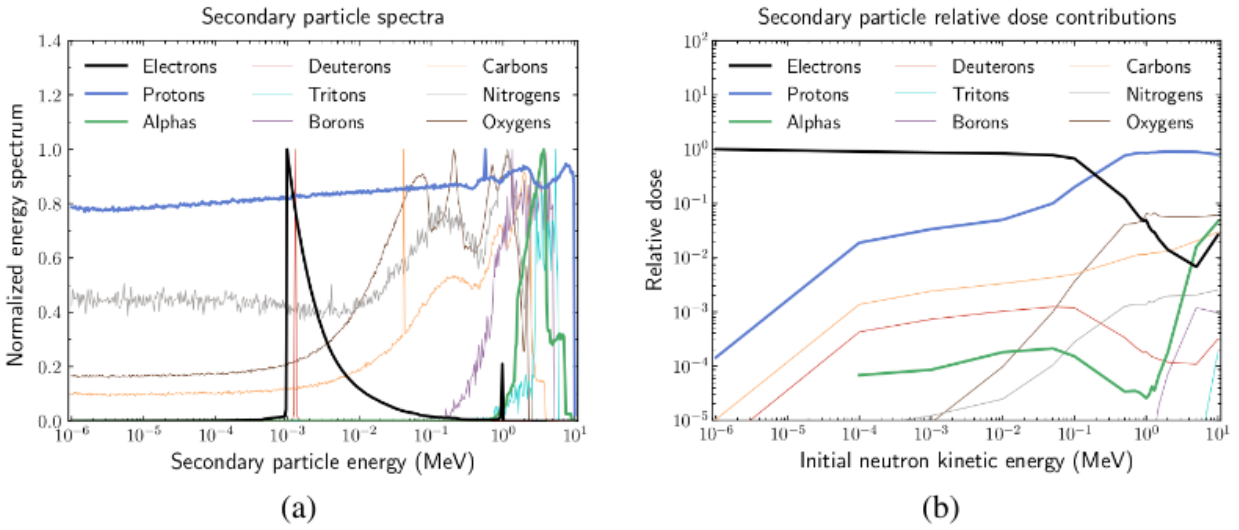


Figure 5.3 (a) Normalized secondary species spectra recorded in the intermediate scoring volume produced by initial neutrons of 10 MeV. (b) Relative dose contributions of secondary species in the intermediate scoring volume for the flat spectrum of neutrons having 18 energies from 1 eV to 10 MeV.

In the next stage, the recorded spectra of secondary species and their relative dose contributions were processed in Geant4-DNA to calculate $\bar{y}_D$ in spherical sampling volumes of varying diameters and using a weighted track sampling algorithm developed by Famulari *et al.* (2017) [40]. The simulations in Geant4-DNA utilized the Monte Carlo track-structure technique for precise microdosimetry. The neutron RBE for each energy was calculated by dividing the $\bar{y}_D$ value obtained from neutron irradiation by the $\bar{y}_D$ value measured using 250 keV X-rays as shown in Figure 5.4.

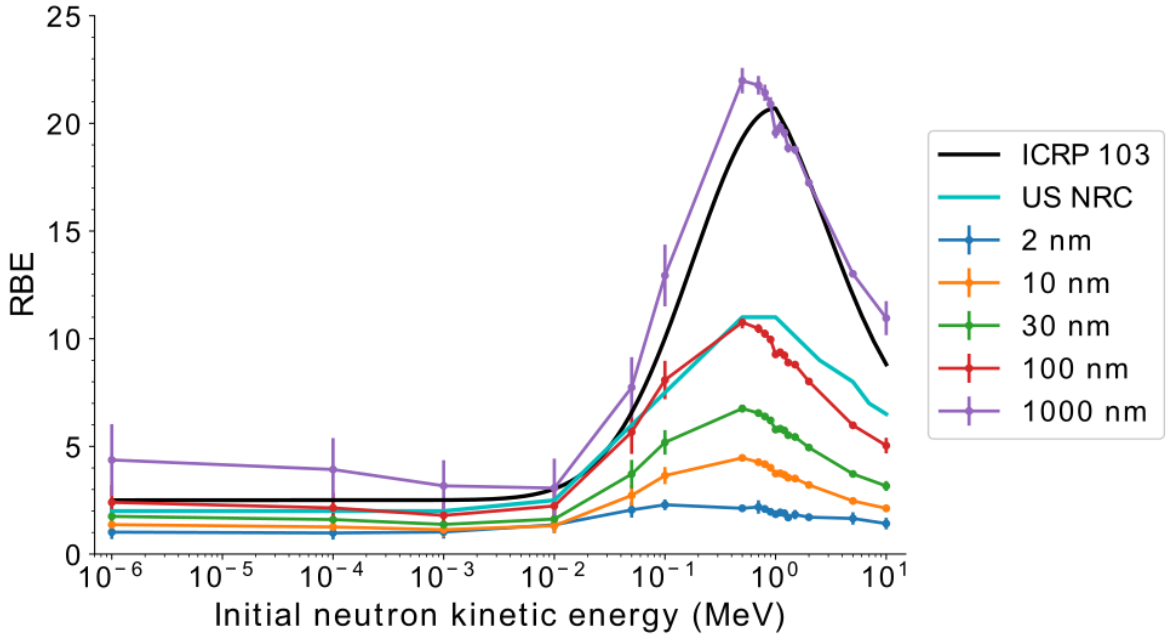


Figure 5.4 Microdosimetric neutron RBE model developed by Lund *et al.* (2020) [10]. Neutron RBE plotted as a function of energy in the outer scoring volume. The results are plotted for different sampling volume diameters to calculate the dose-mean lineal energy alongside the ICRP neutron weighting factors [14] and the US NRC neutron quality factors [41].

### 5.2.2 Neutron RBE for clustered direct DNA damage

The work of Lund *et al.* (2016) [10] provided our research group and the broader scientific community with access to the secondary species spectra generated by the interaction of different neutron beams and 250 keV X-rays with the ICRU sphere phantom material. This access included detailed information on energy deposition patterns and the relative contributions of these secondary species to the total dose. Building on this foundation, Montgomery *et al*. (2021) [28] from our group developed a full nuclear DNA model in an open-source manner using TOPAS and TOPAS-nBio. Their objective was to create a model analogous to the second model of Baiocco *et al.* (2016). However, the Montgomery *et al.* (2021) study also expanded upon Baiocco *et al.*'s (2016) work by including all types of clustered DNA damage such as single-strand breaks (SSBs), base lesions, double-strand breaks (DSBs), complex DSB clusters, and non-DSB clusters to comprehensively assess neutron RBE. Despite the existence of several nuclear DNA models at the time of the Montgomery *et al.* (2021) study, there was a lack of open-source models.

Montogomery *et al.* (2021) filled this gap by providing a complete and open source full nuclear DNA model and released it under the name TOPAS Clustered DNA Damage (hereafter referred as TOPAS-CDD). The main features of the Montgomery *et al.* (2021) study are presented below.

## Step 1: Condensed-history simulations

Montgomery *et al.* (2021) used the simulation pipeline constructed by Lund *et al.* (2020) [10] in Geant4 to get the spectra of secondary species and their relative dose contributions as generated using the condensed-history simulation approach. Essentially the same simulations were performed for neutron beams comprising a flat spectrum with 18 neutron energies ranging from 1 eV to 10 MeV and a reference radiation of 250 keV X-rays. The secondary species spectra and dose depositions were recorded in the inner, intermediate, and outer scoring volumes defined at increasing depths inside the ICRU phantom. The details about the recording of secondary species spectra and calculation of relative dose distribution have been discussed previously in section 5.2.1.

## Step 2: Track-structure simulations

## Nuclear DNA model

Montgomery *et al.* (2021) developed the nuclear DNA model in TOPAS-nBio v1.0. The default parameter values of the DNA model are listed in Table 5.1. This geometric DNA model (Figure 5.5) is based on Villagrasa *et al.*'s [42] chromatin fiber model. In this model, nucleotide base pairs were represented by six spheres, corresponding to the two nitrogenous bases, two deoxyribose molecules, and two phosphate groups (Figure 5.5(a)). Nucleosomes were formed by wrapping 154 DNA base pairs in a double helix around a cylindrical histone complex (Figure 5.5(b)), and ninety of these nucleosomes were connected in a helical arrangement to create a cylindrical chromatin fiber (Figure 5.5(c)).

Following Zhu *et al.*'s [43] approach, a voxel was constructed by arranging 20 chromatin fibers in a fractal pattern (Figure 5.5(d)), using the chromatin folding method of Lieberman-Aiden *et al*. [44]. To build the full nuclear DNA model, $26^3$ cubic voxels were

assembled in a 3D array, resulting in a nucleus model containing 6.3 Gbp of DNA at a density of 13.3 Mbp/$\mu m^3$, consistent with human nuclei (typically nucleus of volume $500$ $\mu m^3$ contains 6.2 Gbp of nucleotides with a density of 12 Mbp/$\mu m^3$). This cubic nucleus model, with a volume of 475 $\mu m^3$, was placed within a 2000 $\mu m^3$ spherical cell volume to simulate a fibroblast in the $G_0/G_1$ phase (Figure 5.5(e)). The entire cell model, along with all its contained volumes, was treated as liquid water with a density of 1.0 g/$cm^3$, except for the nucleotides, which were assigned a density of 1.407 g/$cm^3$. Each voxel, chromatin fibre, DNA strand, nucleotide, and base pair molecule in each nucleotide of the cell model was given a unique integer identifier that helped in determining the location of induced damages.

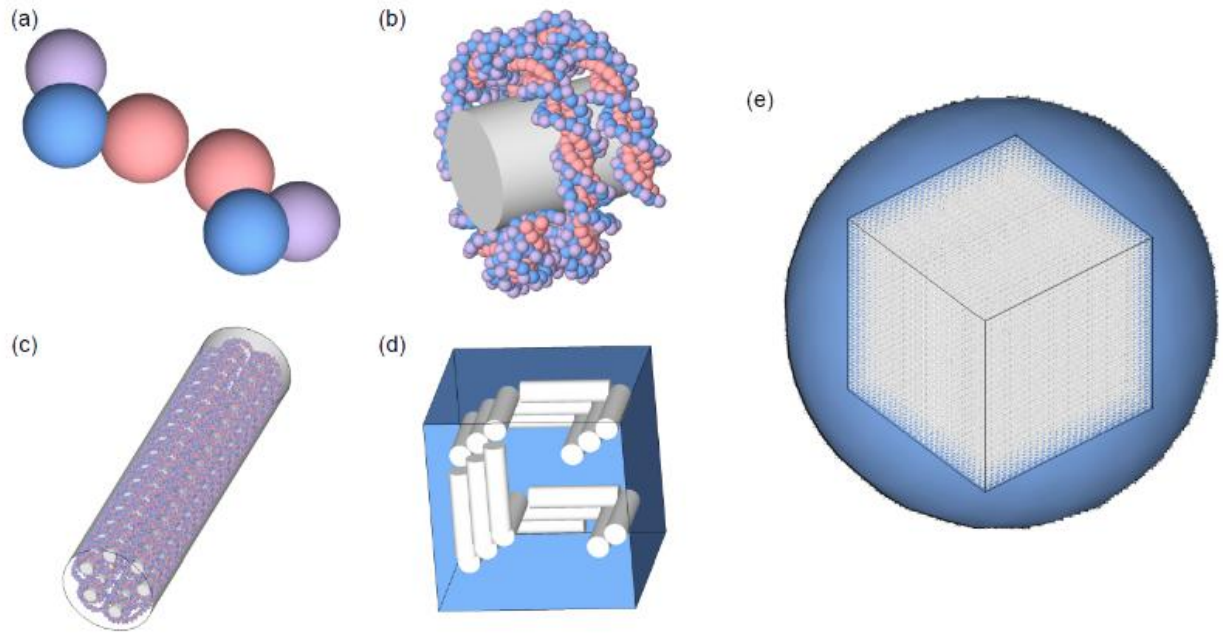


Figure 5.5 Nuclear DNA model developed by Montgomery *et al.* (2021) [28]. (a) A nucleotide base pair containing two nitrogenous bases (red), two deoxyribose molecules (blue) and two phosphate groups (purple). (b) Nucleosome containing 154 base pairs arranged in a double helix and wrapped around a cylindrical histone. (c) A cylindrical chromatin fibre containing 90 nucleosomes connected in a helical arrangement. (d) A voxel constructed using 20 chromatin fibres arranged in a fractal pattern. (e) A cubic nucleus containing $26^3$ voxels, placed in a spherical cell volume. Figure from Montgomery *et al.* (2021) [28].

## Physics settings

To accurately simulate electron transport in liquid water in TOPAS-nBio, Montgomery *et al.* (2021) customized the Geant4-DNA physics constructors (collection of physics models) to be used as a physics module in TOPAS-nBio. The G4EmDNAPhysics_option2 (opt2) constructor offers discrete physics models to track electron transport in liquid water from 1 MeV down to 7.4 eV. The more recent G4EmDNAPhysics_option4 (opt4) constructor has alternative physics models to opt2 for electron transport in liquid water in the 10 eV-10 keV energy range. The physics models included in opt4 provide an updated cross-section as compared to opt2.

In this study, the hybrid physics constructor, named G4EmDNAPhysics_hybrid2and4 (hybrid), developed by Lund *et al.* (2020) [10], was used. This hybrid constructor combines the strengths of both opt2 and opt4, utilizing opt4's models up to 10 keV and opt2's models for higher energies up to 1 MeV. For electrons with kinetic energies less than 10 eV, their tracks were terminated, and their energies deposited locally, following the recommendations from the TOPAS collaboration [45]. The hybrid physics constructor also uses the physics models for protons and α-particles that are available in Geant4-DNA.

Table 5.1 Parameters used to develop the full nuclear DNA model by Montgomery *et al.* (2021) [28]

| Component | Parameter | Value |
|---|---|---|
| DNA base pair | Nitrogenous base radius | 0.3 nm |
| | Deoxyribose radius | 0.29 nm |
| | Phosphate group radius | 0.27 nm |
| Nucleosome | Histone complex dimensions | 2.4 nm radius, 5.72 nm height |
| | Number of bp per nucleosome | 154 bp (+ 46 bp of linker DNA) |
| Chromatin fibre | DNA content per chromatin fibre | 90 nucleosomes ( 18 000 bp) |
| | Chromatin fibre radius | 17 nm |
| | Chromatin fibre length | 136 nm |
| Voxel | Number of fibres per voxel | 20 fibres |
| | Voxel dimensions | 0.3 μm * 0.3 μm * 0.3 μm |
| Nucleus | Number of voxels | 17 576 voxels (26 * 26 * 26 grid) |
| | Volume | 475 $\mu m^3$ |
| | Number of base pairs | 6.3 Gbp |
| | Density of DNA | 13.3 Mbp / $\mu m^3$ |
| Cell | Volume | 2000 $\mu m^3$ |

## Irradiation scenario

Only the electron, proton, and α-particle species from each set of secondary particle spectra (one set per scoring volume) from Lund *et al.* (2020) [10] were used in the track-structure simulations because Geant4-DNA did not offer ionization models for heavier ions. To replicate the way secondary particles were generated and recorded upstream in condensed-history simulations, a volume source was defined. The particles were distributed throughout the cell volume including the nucleus in random directions. This source distribution is consistent with the work of Baiocco *et al.* (2016). A total target dose $D_0$ of 1 Gy was delivered to the nucleus for each initial neutron energy and the reference X-rays. This was consistent with the recent literature to ensure comparability of results

[31, 43, 46]. By irradiating the nuclear DNA model in track-structure simulations using the secondary species spectra recorded in the inner, intermediate, and outer scoring volumes as determined using the condensed-history approach, we effectively replicated the scenario of irradiating the DNA model with neutrons at the corresponding positions within the ICRU sphere. For each secondary particle species $\mathrm{i}$, initial neutron energy $\mathrm{E}$, in a particular scoring volume $\mathrm{k}$, the species-specific target dose $[\,D_i(E)]_k$ was calculated by multiplying their relative dose contribution $[\,r(E)]_k$ with the total target dose $D_0$.

$$[\,D_i(E)]_k = [\,r_i(E)]_k * D_0$$

Three distinct simulations, one per scoring volume, for each species (electrons, protons, and α-particles) were conducted to achieve the species-specific target dose. Simulations were stopped once the species-specific target dose was achieved. However, in each simulation, the species target dose $[\,D_i(E)]_k$ was found to be slightly higher than the actual delivered dose $[\,d(E)]_k$ as the simulation stops only after the complete processing of the current event i.e. the current particle track and any secondary tracks.

## DNA damage clustering algorithm

The study by Montgomery *et al.* (2021) analyzed five types of DNA damage - SSBs, base lesions, DSBs, complex DSB clusters, and non-DSB clusters. The energy depositions in all the sensitive DNA volumes (i.e. the nitrogenous bases, deoxyribose molecules, and phosphates) were recorded for each irradiation scenario described in previous section. The definition of each type of damage examined is described below.

An SSB was considered to occur when the cumulative energy deposited in the sugar-phosphate backbone of a nucleotide exceeded 17.5 eV. This threshold was derived from the work of Charlton and Humm [47] who modeled the experimental work of Martin and Haseltine [48] to study SSB induction by Auger electrons from iodine-125. A base lesion was found to occur when the cumulative energy deposited in a nitrogenous base exceeded 17.5 eV. Although consensus is lacking, there is precedent for scoring base lesions using the same energy threshold applied to SSBs. If two SSBs from opposing strands of DNA occur within 10 bp of each other (i.e. within about one turn of DNA double helix) then a DSB was recorded. Van der Schans [49] determined the maximum number

of nucleotide pairs between SSBs on opposite strands of DNA, beyond which a DSB would not occur by conducting experiments on bacteriophage DNA. A custom DNA damage clustering algorithm was developed to identify the complex DSB cluster and non-DSB clusters by processing the list of recorded SSBs, base lesions, and DSBs. Lesions were grouped into a cluster if they occurred within 40 base pairs of each other - close enough to be within a few turns of the DNA double helix and potentially impact DNA repair. Clusters containing one or more DSBs were labeled as complex DSB clusters, while those without any DSBs were labeled as non-DSB clusters. The length, complexity, and density of these clusters were calculated to understand their characteristics and the impact of neutron energy.

## DNA damage yields

To calculate the DNA damage yields $\left[Y_N^j\ (E)\right]_k$ for each particle species i, generated from an initial neutron energy E in a scoring volume k and inducing a DNA damage j, the species-specific damage yields were combined using a weighted sum.

$$\left[Y_N^j\ (E)\right]_k = \sum_{i=1}^{I} \frac{\left[Y_N^j\ (E)\right]_k [D_i\ (E)]_k}{[d_i\ (E)]_k}$$

In this equation, N refers to neutrons, $[\ D_i(E)]_k$ is the relative target dose and $[\ d(E)]_k$ is the actual dose received for a secondary particle species i.

However, for reference radiation (250 keV), electrons are the only secondary species (denoted as e), so the damage yields did not need to be summed.

$$\left[Y_X^j\ (E)\right]_k = \frac{\left[Y_e^j\ (E)\right]_k [D_e\ (E)]_k}{[d_e\ (E)]_k}$$

## Calculation of Neutron RBE

The neutron RBE was calculated by comparing the neutron-induced DNA damage yields with those induced by 250 keV X-rays. This was done for each type of DNA damage, with a specific focus on the energy dependence of the RBE.

$$\left[RBE^{j}\ (E)\right]_k = \frac{\left[Y_N^j\ (E)\right]_k}{\left[Y_X^j\right]_k}$$

## Uncertainty in RBE

The uncertainties in RBE values were calculated by propagating the standard deviation of the mean neutron-induced and X-ray-induced yields using conventional uncertainty propagation rules. Specifically, the uncertainty in RBE was calculated using the formula:

$$\sigma_{RBE} = \left|\frac{Y_n}{Y_X}\right| * \sqrt{\left(\frac{\sigma_{Y_n}}{Y_n}\right)^2 + \left(\frac{\sigma_{Y_X}}{Y_X}\right)^2}$$

where:

$Y_n$ and $Y_X$ are the mean neutron-induced and X-ray induced yields respectively.

$\sigma_{Y_n}$ and $\sigma_{Y_X}$ are their corresponding standard errors.

This method ensures that the propagated uncertainty in RBE accounts for the relative errors in both yield measurements.

### 5.2.3 Neutron RBE for indirect DNA damage

Manalad *et al.* (2023) [50] expanded on the work of Montgomery *et al.* (2021) by integrating a validated indirect action model of radiation damage in the existing simulation pipeline. They provided our group with a more comprehensive model of neutron-induced DNA damage and determined the neutron RBE for inducing clustered DNA lesions by the combined effect of direct and indirect action of radiation. The direct damage scorer of Montgomery *et al.* (2021) was updated to also track indirect action in a simulation geometry. The default simulation parameters used in the Manalad *et al.* (2023) [50] study are listed in Table 5.2.

## Indirect radiation damage

The open-source indirect action algorithm by Zhu *et al.* [51] was integrated into the existing pipeline to enable the simulation of indirect radiation action by Manalad *et al.* (2023) [50]. This was achieved by updating the relevant codes from Montgomery *et al.*

(2021) to incorporate the indirect action and the new damage types it introduced (described in the following section). All products of water radiolysis (hydroxyl (·OH), solvated electron ($e_{aq}^{-}$), and hydrogen (·H) radicals) available in the chemistry constructor were simulated. Consistent with previous work in literature [2], the duration of the chemical stage was set to 1 ns which is approximately the lifetime of ·OH in the cell. A time-step resolution of 1 ps was set during the chemical stage. The reactive species originating from DNA and histone volumes were immediately stopped. Histones were treated as scavengers of hydroxyl (·OH), solvated electron ($e_{aq}^{-}$), and hydrogen (·H) radicals. The ·OH radical tracks were terminated after an indirect action event with a sugar-phosphate or nucleobase volume. The default chemistry constructor in TOPAS-nBio, TsEmDNAChemistry, which includes updated parameters compared to its Geant4-DNA counterpart, G4EmDNAChemistry, was used.

Table 5.2 The default simulation parameters used in Manalad *et al.* (2023) [50] study.

| Parameter | Value |
|---|---|
| Target geometry | Nuclear DNA model (see Table 5.1) |
| Target material | Liquid water |
| | Density in the sensitive DNA volumes: 1.407 g*cm$^{-3}$, |
| | Elsewhere: 1 g*cm$^{-3}$ |
| Physics Module | G4EmDNAPhysics_hybrid2and4 |
| Chemistry Module | TsEmDNAChemistry |
| | Duration of chemical stage: 1 ns; time-step resolution: 1 ps |
| Additional constraints | DNA molecules are scavengers of ·OH radicals. |
| in the chemical stage | Histones are scavengers of ·OH, $e_{aq}^{-}$ and ·H radicals. |
| | Reactive chemical species are not allowed to be generated inside DNA and histone volumes. |
| Source particle | Electrons, protons, and α-particles |
| Simulation cutoff | Cumulative dose of 1 Gy to the nuclear DNA model |
| Induction of SSB | Direct: A cumulative energy of 17.5 eV deposited in the sugar-phosphate molecules comprising a nucleotide. |
| | Indirect: 0.4 damage probability for ·OH radical with a sugar-phosphate molecule |
| Induction of base damage | Direct: A cumulative energy of 17.5 eV deposited in a nucleobase volume. Indirect: 0.4 damage probability for ·OH radical with a nucleobase volume |
| Induction of DSB | Direct, Indirect, and Hybrid: two SSBs on opposite strands within 10 bp |
| Induction of clustered DNA damage | Aggregation of DNA lesions within 40 bp of each other |
| | C-DSB or N-DSB (direct, indirect, or hybrid) |
| Number of histories | Variable (1 – 10 000 per simulations) |
| Number of threads | 10 |

## Revised DNA damage clustering algorithm

With the integration of the indirect action model, the DNA damage clustering algorithm in the TOPAS-CDD code was updated accordingly. Simple lesions, such as SSBs and base lesions, were categorized as either direct or indirect. In contrast, DSBs, complex DSB clusters, and non-DSB clusters could be classified as direct, indirect, or hybrid (resulting from both direct and indirect actions). For the indirect action model, only damage from interactions between highly reactive ·OH radicals and the sugar-phosphate backbone were recorded. A damage probability of 40% was assigned to indirect action events involving ·OH radicals and pairs of deoxyribose (sugar) and phosphate volumes, a value chosen to align with published literature.

## Neutron RBE estimation

The energy-dependent neutron RBE values for various types of DNA damage were estimated by simulating neutron and reference photon irradiations as before. The RBE curve from Manalad *et al.* (2023) [50], shown in Figure 5.6, represents the ratio of neutron-induced complex DSB yields to those induced by reference photons. The neutron RBE value for inducing C-DSB clusters for all scoring volumes was lower for combined action (direct and indirect) than due to direct action alone (Figure 5.6). It could be because of even more clustering of DNA lesions due to combined actions (compared to direct action alone) that results in more lesions per cluster, but less relative increase in cluster count compared to 250 keV X-rays. Assuming this is the case, C-DSBs due to combined action are potentially more difficult to repair due to the increased density of lesions that include DSBs and correspondingly may be more likely to result in mutagenesis. However, in contrast, looking at RBE alone for inducing C-DSBs, it would appear that direct action is more detrimental than combined action.

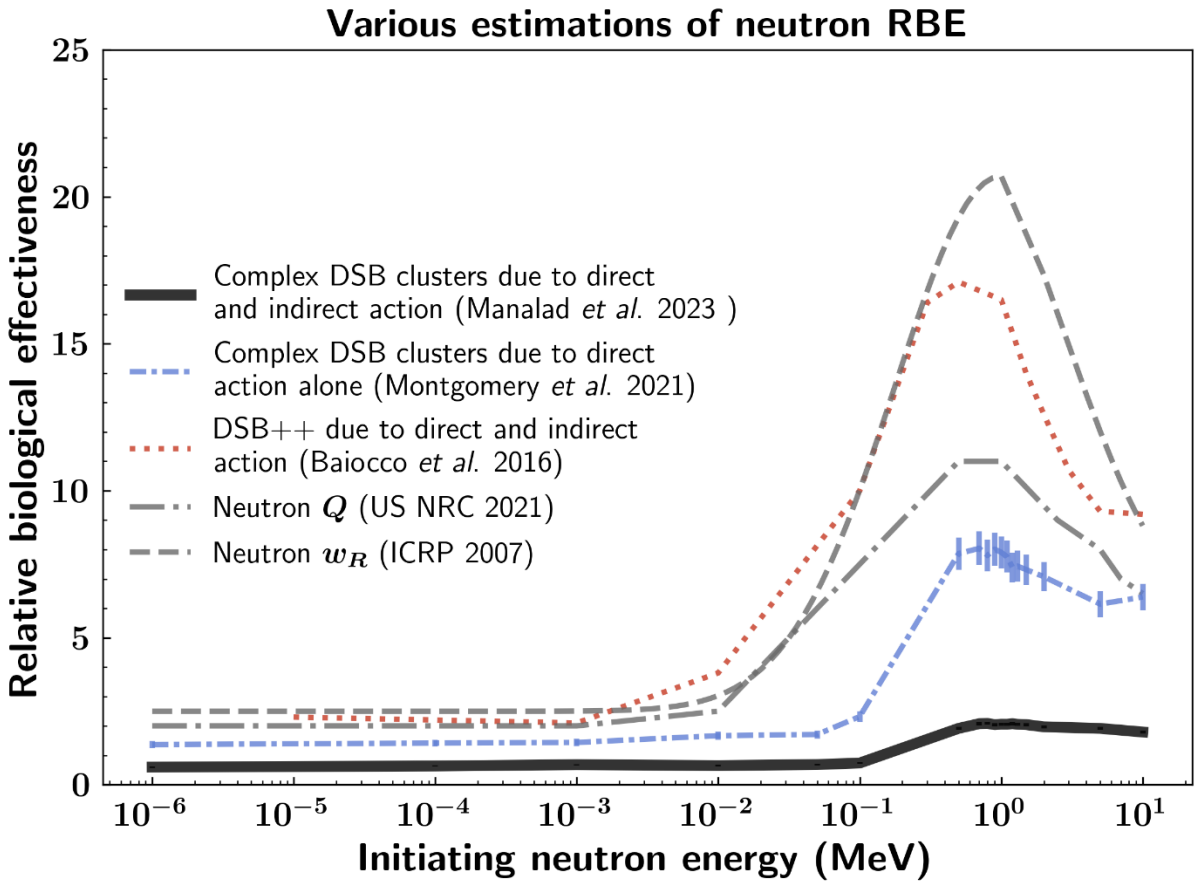


Figure 5.6 Neutron RBE estimated for inducing complex DSB clusters due to direct and indirect action in the intermediate scoring volume compared against RBE estimates of Montgomery *et al.* (2021) and Baiocco *et al.* (2016) alongside the ICRP neutron weighting factors [14] and US NRC neutron quality factors [41]. The error bars represent the standard error of the mean across 100 simulation repeats.

## 5.3 Measuring neutron spectra in radiotherapy

Mathew *et al.* (2021) [52] from our research team measured the neutron spectra arising from a Varian TrueBeam STx 15 MV linac at various locations in the bunker. The linac was operated at a dose rate of 600 MU/min with the collimator jaws completely closed. To capture the neutron fluence rate spectra, they developed a passive-readout Nested Neutron Spectrometer (NNS), using 99.9% pure gold activation foils as a replacement for the default He-3 detector core found in an active NNS. The measurements were taken at four distinct locations (see Figure 5.7) : location A at 100 cm from the isocenter along the

couch and away from the gantry, location B at 200 cm from the isocenter along the couch and away from the gantry, location C at the maze room junction, and location D in the maze. The neutron fluence rate spectrum captured at locations A, B, C, and D is illustrated in Figure 5.8. The neutron spectra measured by Mathew *et al.* (2021) [52] were used to irradiate the in-vitro simulation geometry modeled in this thesis work, providing essential data for the simulation environment.

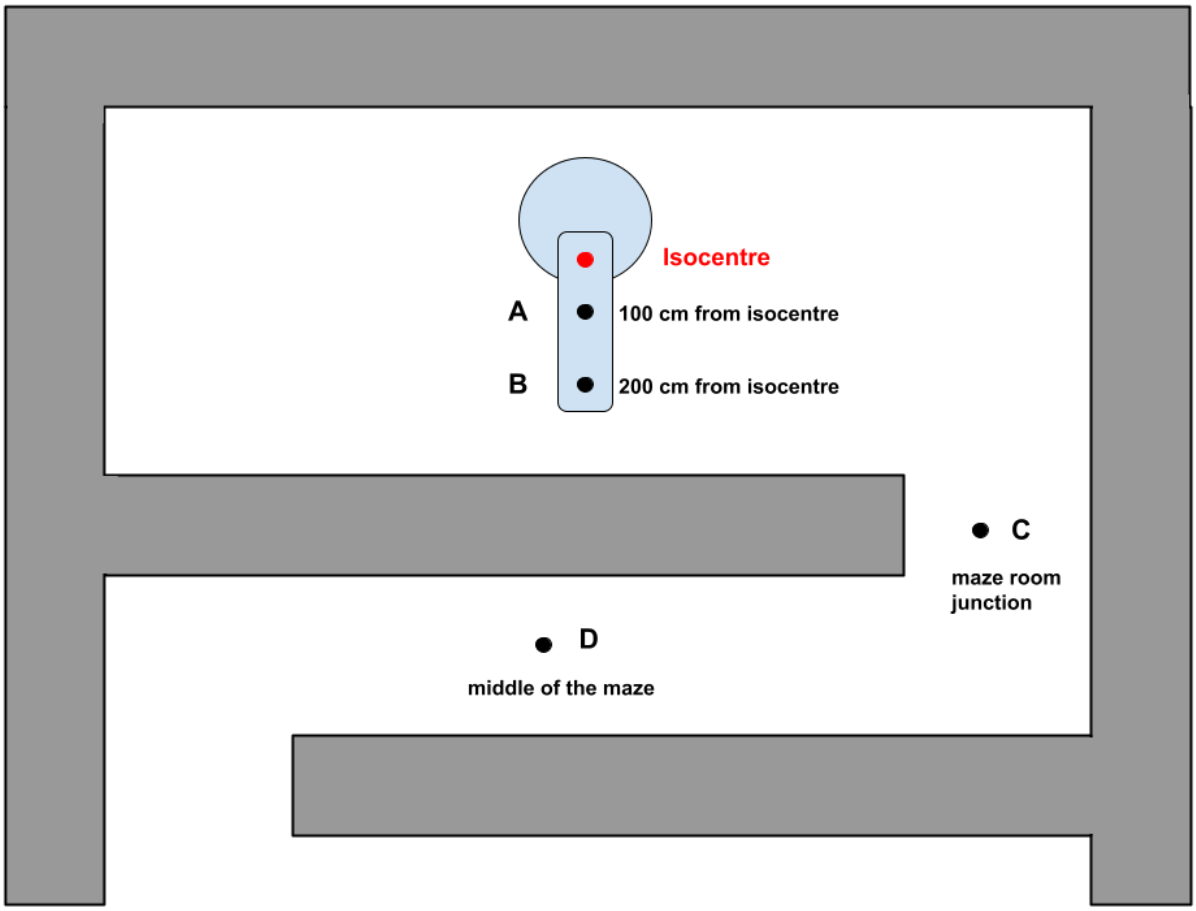


Figure 5.7 Schematic of the Varian TrueBeam STx 15 MV treatment room at the McGill University Health Centre that was used for the neutron spectral measurements of Mathew *et al.* (2021) [52] (figure not to scale). The measurement locations to record the neutron spectra in the bunker are indicated in black.

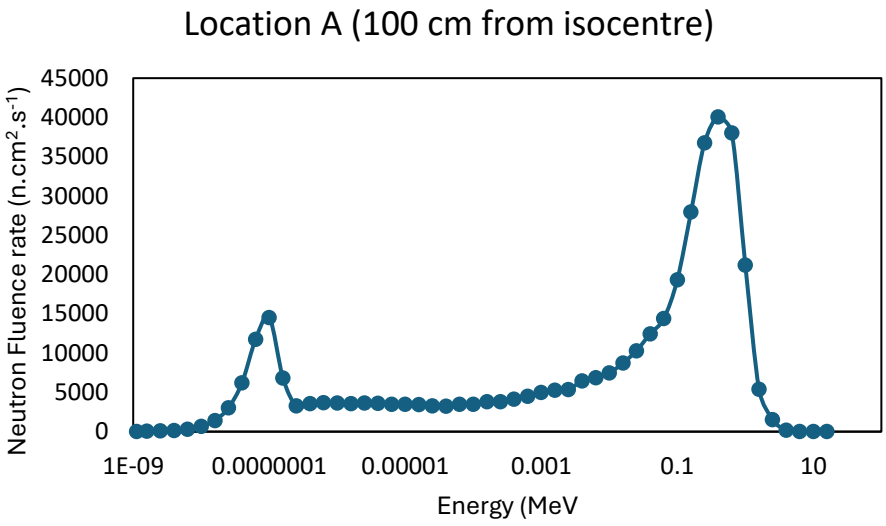
Location A (100 cm from isocentre)
Neutron Fluence rate (n.cm$^{-2}$.s$^{-1}$)
45000
40000
35000
30000
25000
20000
15000
10000
5000
0
1E-09
0.0000001
0.00001
0.001
0.1
10
Energy (MeV

(a)

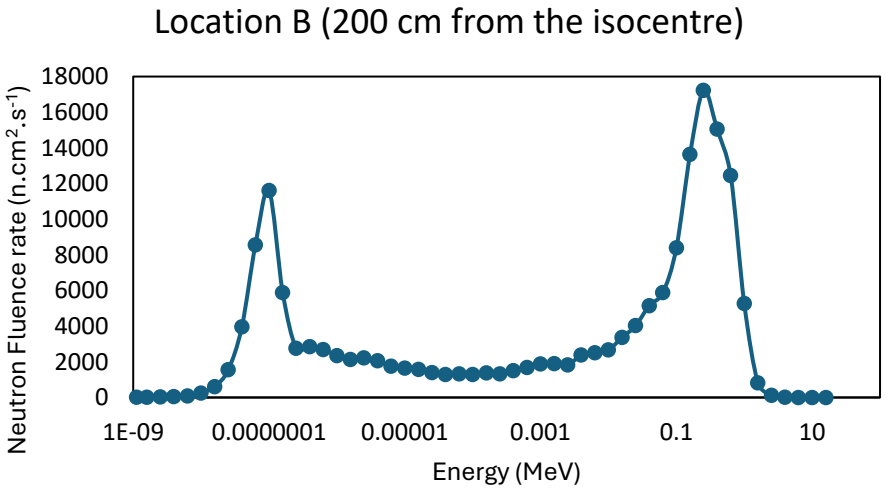
Location B (200 cm from the isocentre)
Neutron Fluence rate (n.cm$^{-2}$.s$^{-1}$)
18000
16000
14000
12000
10000
8000
6000
4000
2000
0
1E-09
0.0000001
0.00001
0.001
0.1
10
Energy (MeV)

(b)

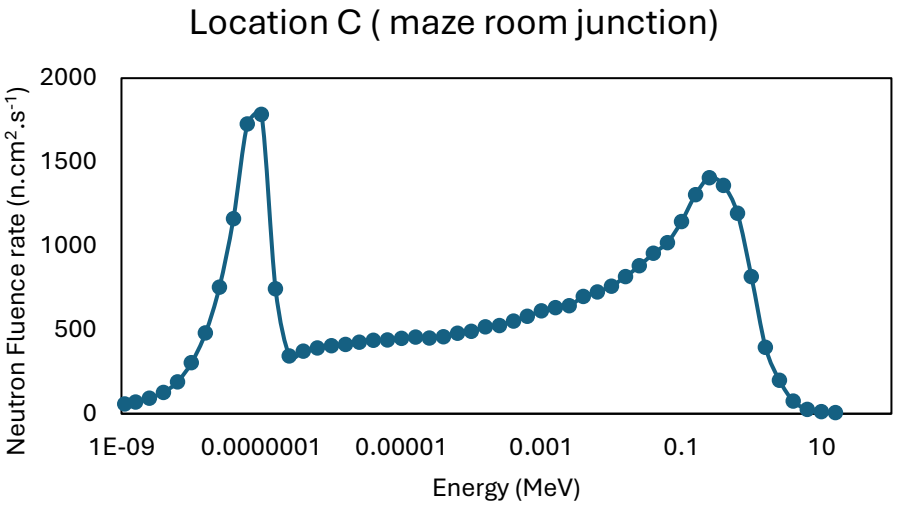


(c)

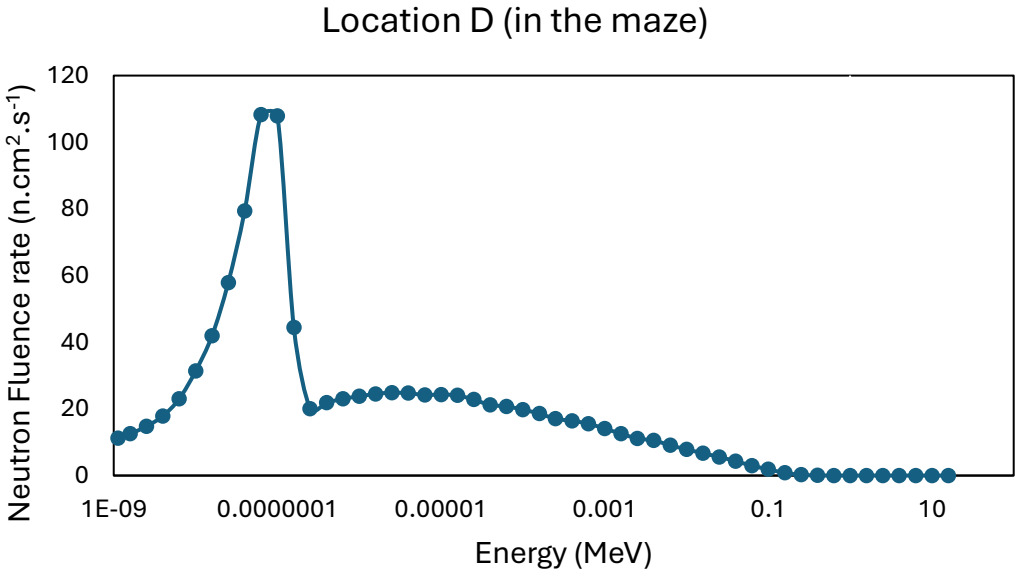


(d)

Figure 5.8 Neutron fluence rate spectra measured by the passive NNS at: (a) Location A (1 metre from the isocentre), (b) Location B (200 metre from the isocentre), (c) Location C (maze room junction), and (d) Location D (in the maze) in a 15 MV linac bunker.

# Chapter 6

# Methodology

## 6.1 Project's simulation pipeline

The flowchart presented in Figure 6.1 outlines the sequence of NICE projects, one project per column, with inherited components from earlier projects shown in the same color to indicate continuity. New developments introduced in each project are displayed in a different color, with relevant updates provided to highlight their significance.

The first column represents the study by Lund *et al.* (2020) [10], as discussed in Chapter 5. Lund *et al*. (2020) [10] constructed a simulation pipeline to explore neutron RBE as a function of energy. They modeled an ICRU sphere phantom in Geant4 v10.04 and exposed it to (i) a flat spectrum of neutrons spanning 18 energies from 1 eV to 10 MeV and (ii) 250 keV X-rays. Using Geant4-DNA, they calculated $\bar{y}_D$, which served as a proxy for RBE.

The second column showcases the work by Montgomery *et al.* (2021) . They utilized the energy spectra and relative dose contributions of secondary charged particles generated by Lund *et al.* (2020) [10] in the ICRU phantom. Their work involved developing a full nuclear DNA model in TOPAS and TOPAS-nBio to estimate neutron RBE for clustered direct DNA damage by comparing neutron-induced DNA damage yields with those caused by 250 keV X-rays.

The third column highlights the study by Manalad *et al.* (2023) [50]. They expanded on the work of Montgomery *et al.* (2023) by incorporating an indirect action model of radiation damage into the existing pipeline. Like Montgomery *et al.* (2023), they also relied on the secondary species energy spectra and relative dose contribution data produced by Lund *et al.* (2020) [10] using Geant4.

The fourth column details the simulation pipeline developed in this project, fully implemented in TOPAS v3.6 and TOPAS-nBio v1.0. This work replicated the Geant4 pipeline by Lund *et al.* (2020) [10] to generate secondary species energy spectra and

relative dose contributions using TOPAS. Since TOPAS v3.6 is based on Geant4 v10.06, all simulations originally performed by Lund *et al.* (2020) [10] in Geant4 v10.04 were repeated using Geant4 v10.06 with the expectation that the results would be identical or very close to those produced using TOPAS v3.6. Subsequently, the ICRU sphere phantom was replaced with an in-vitro geometry and exposed to realistic neutron spectra from a 15 MV linac, instead of a flat neutron spectrum, to replicate real-world conditions. The nuclear DNA model, updated by Manalad et al. (2023) [50], was employed in TOPAS-nBio to estimate damage yields and corresponding RBEs for neutrons and 250 keV X-rays. The final column represents the NICE group's ongoing work, reflecting the latest developments and outlining future research directions.

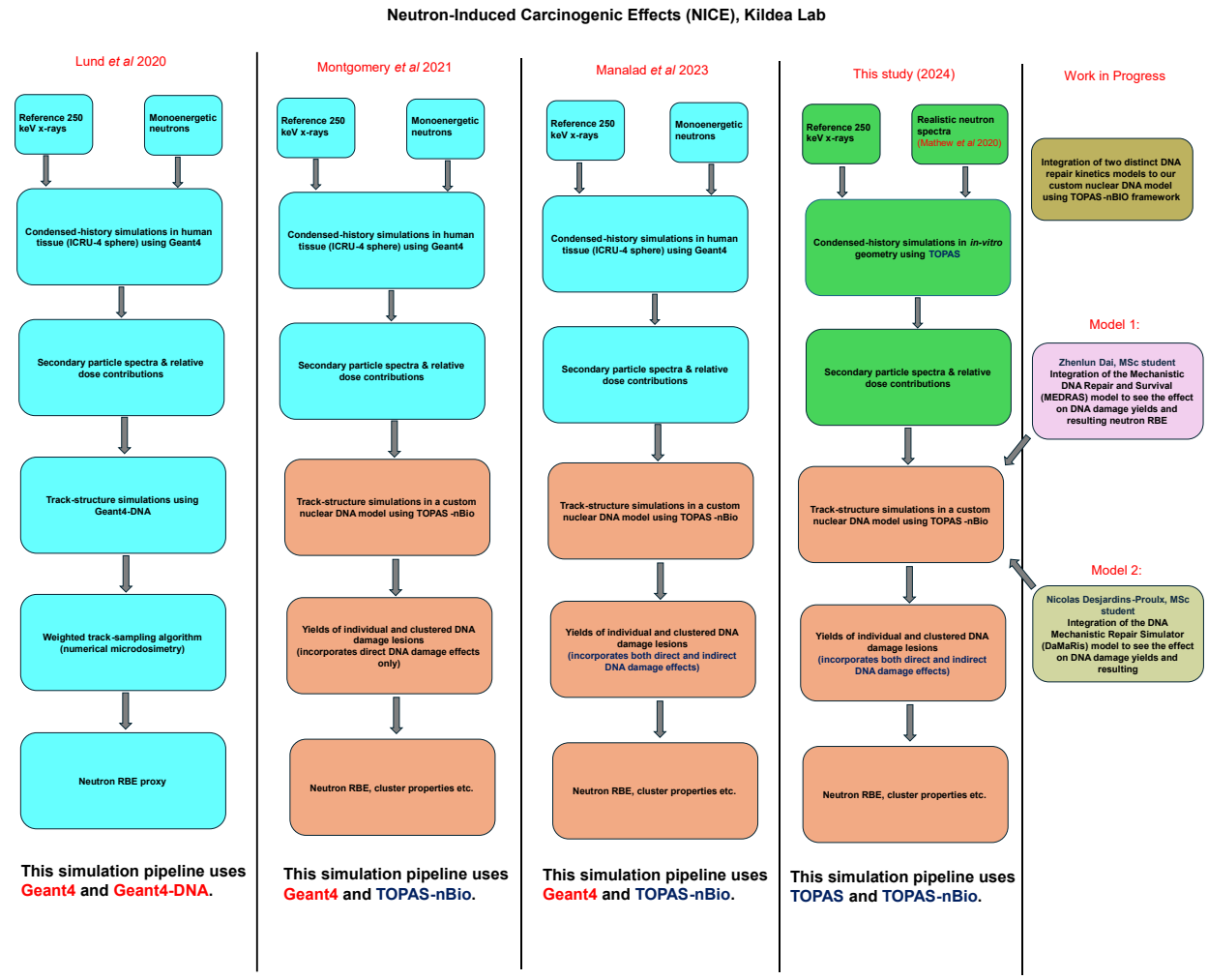


Figure 6.1 The flowchart outlines the sequence of NICE [29] projects.

### 6.1.1 Simulation environment in the ICRU sphere

A difference was encountered in the simulation environment experienced by the scoring volumes inside the ICRU sphere between Geant4 and TOPAS. In the study by Lund *et al.* (2020) [10] , heavy charged particles were terminated at their point of origin, regardless of whether they originated inside the scoring volumes or elsewhere in the ICRU sphere. As a result, secondary charged particles originating outside the scoring volumes were not recorded. In contrast, in TOPAS, only secondary charged particles interacting within the scoring volumes were handled, with their fate determined by the particle type (i.e., either terminated or allowed to interact further). This discrepancy in the radiation simulation environment between Geant4 and TOPAS is illustrated in Figure 6.2.

For example, if a heavy charged particle originated near the boundary of a scoring volume, it was immediately terminated in Geant4. However, in TOPAS, the particle was allowed to enter the scoring volume and deposit energy. Despite this difference, the total number of heavy charged particles generated was not significant, and the effect of this variation on the secondary species spectra and their relative dose contributions was minimal.

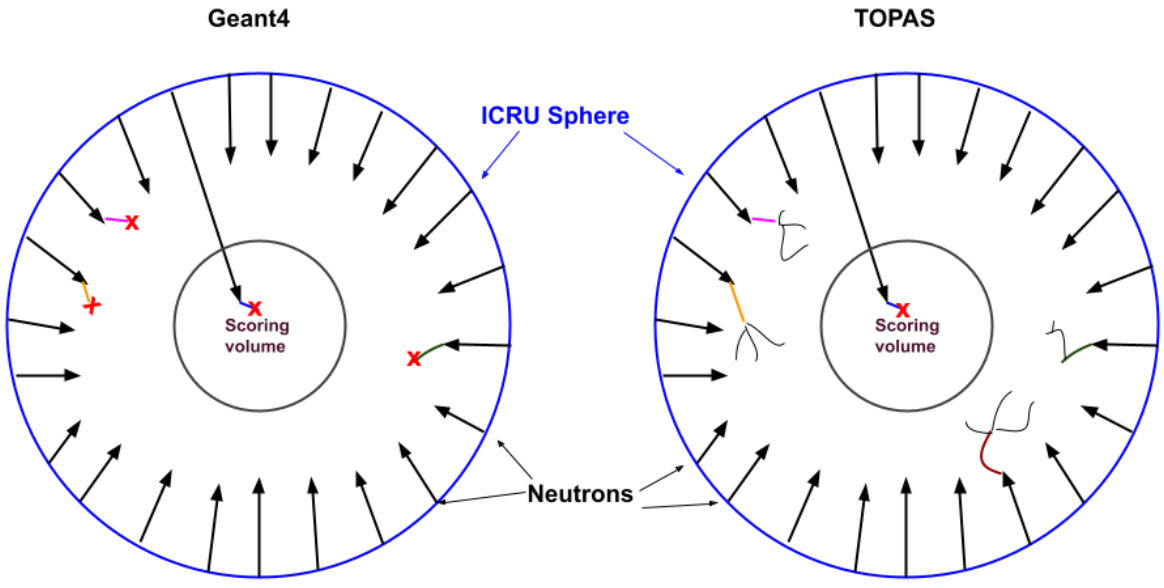

Figure 6.2 Schematic representation of the simulation environment inside the ICRU phantom, as modeled in Geant4 and TOPAS. The red cross denotes the termination of a particle's track. For simplification, only the inner scoring volume (not to scale) is displayed. In Geant4, secondary heavy charged particles (represented by thick, colored squiggly lines) are terminated immediately upon generation, regardless of their origin within the phantom. In contrast, in TOPAS, these particles were allowed to interact freely within the ICRU sphere, generating tertiary particles (depicted as black squiggly lines). They were only terminated upon entering the scoring volume or if generated within the scoring volume.

### 6.1.2 Local approximation and handling of high-energy electrons

In the study by Lund *et al.* (2020) [10], all secondary charged particles (except protons and high-energy electrons) were terminated at their point of origin in condensed-history simulations to achieve the local approximation condition, meaning their energies were assumed to be deposited locally. Protons were allowed to interact freely and were tracked until their energies reached 0 eV. High-energy electrons were handled differently, they were allowed to interact until their energies dropped to 1 MeV, at which point they were terminated, and their remaining energies were assumed to be deposited locally under the local approximation condition.

In this thesis, the local approximation condition applied by Lund *et al.* (2020) [10] was revisited. Upon re-examination, it was found that the heavy charged particles (including deuterium, triton, beryllium, boron, carbon, nitrogen, oxygen ions, and α-particles), as well as protons, adhered to the local approximation in the tested neutron energy ranges of 1 eV, 1 MeV, and 10 MeV. However, electrons with energies around 1 MeV, which were terminated in Lund *et al.*'s (2020) [10] study did not follow the local approximation, and their energies were not deposited locally.

Thus, in this thesis, the electron spectra were generated by allowing electrons to interact freely and recording their energy deposition until they reached 0 eV. This modification altered the electron spectra compared to those reported by Lund *et al.* (2020) [10].

To determine whether a particular secondary charged species follows the local dose approximation condition, its relative dose values were compared using two approaches:

1. Local Deposition Approximation – The species was terminated at its point of origin, assuming that its entire dose was deposited locally.
2. Full Interaction Simulation – The species was allowed to interact fully, and its actual relative dose contribution was calculated.

If the relative dose values from both approaches match, it indicates that the species follows the local dose approximation condition.

### 6.1.3 Thermal hydrogen of Water

Lund *et al.* (2020) [10] customized the ICRU-4 sphere phantom geometry by replacing the hydrogen component with so-called thermal hydrogen of water (TS_H_of_Water), which is a temperature-scaled version of hydrogen. The element TS_H_of_Water shares properties with hydrogen, including isotope fractions, density, atomic mass, and other parameters, but its cross-sections are temperature dependent. To activate neutron thermal scattering models in Geant4 (and TOPAS), users must redefine hydrogen as "TS_H_of_Water" for accurate modeling of thermal neutron transport in water.

Upon review, it was discovered that Lund *et al.* (2020) [10] correctly defined the element TS_H_of_Water in Geant4 but accidentally used the standard hydrogen element in their simulations. This bug in the code resulted in inaccurate modeling of thermal neutron transport, as their thermal neutron models were never activated during the simulations. Although the impact of using the element TS_H_of_Water on the relative dose contribution values was found to be minimal, it significantly affected the proton spectra in the thermal neutron range.

### 6.1.4 Thermal neutron physics models

Lund *et al.* (2020) [10] used G4ParticleHPThermalScattering class to achieve accurate modeling of thermal neutron transport. Building on their work, we utilized the TOPAS Extensions Framework to import the G4ParticleHPThermalScattering class into TOPAS

as a custom physics module and applied it in our simulations. To achieve this, we developed two additional physics modules in C++, adopting a custom TOPAS style that closely mirrors the Geant4 syntax. These modules enabled high-precision modeling of thermal neutron scattering below 4 eV, following the approach implemented by Lund *et al.* (2020) [10].

### 6.1.5 Radiation source definition in TOPAS

In the study by Lund *et al.* (2020) [10], an ICRU sphere phantom with a radius of 15 cm was isotropically irradiated by a flat neutron spectrum emitted from the surface of a spherical shell with a radius of 20 cm. To realistically simulate this isotropic emission from the surface source, the cosine angular distribution was applied in the source definition within Geant4. This distribution aligns with physical principles, such as Lambert's cosine law, ensuring that the emitted particle flux is uniform across the surface.

To replicate this source definition in TOPAS, we defined an "environment source," which created a notional radiation cavity. This cavity was modeled as a sphere with radius R, where primary particles were generated on the surface of the sphere and directed inwards, following a cosine angular distribution relative to the inward directions. This configuration produced an isotropic, homogeneous, omnidirectional flux.

However, when defining the environment source in TOPAS to irradiate the ICRU-4 sphere phantom isotropically, the radius of the notional cavity created by TOPAS was 25.9 cm, which is larger than the 20 cm radius spherical shell used by Lund *et al.* (2020) [10]. The rationale for this 25.9 cm radius lies in how Geant4 computes an "extent" or "bounding box". For a sphere of radius r, the bounding box is a cube with sides of length 2*r. To enclose this bounding box in a notational radiation cavity, the required radius is $\sqrt{3}$ *r, which for the 15 cm radius of the ICRU sphere gives a cavity radius of approximately 25.9 cm. This difference in the source diameter compared to the spherical shell used by Lund *et al.* (2020) [10] led to a discrepancy in the total dose recorded in all scoring volumes.

A detailed comparison of the simulation parameters utilized in TOPAS for this study and those employed by Lund *et al.* (2020) [10] is provided in Table 6.1.

Table 6.1 A comparison of simulation parameters used in Geant4 by Lund *et al.* (2020) [10] and the simulation parameters utilized in TOPAS for this study.

| Parameter | Simulation parameters used in Geant4 v10.04 by Lund *et al.* (2020) [10] | Simulations parameters used in TOPAS v3.6 (This study) |
|---|---|---|
| Local approximation condition in secondary species spectra generation | Applied to all secondary charged particles but high energy electrons were handled separately. | Applied to all secondary charged particles except electrons. |
| Electrons | Electrons having energy below 1 MeV generated in the scoring volume or generated elsewhere in the ICRU sphere and passing the scoring volume were stopped immediately, and their energy was recorded by applying the local approximation condition.<br>High-energy electrons (≥ 1MeV) were allowed to interact and transported until a cut-off of 1 MeV. | All electrons were allowed to interact in the scoring volumes freely until their energy dropped to 0 eV. |
| ICRU phantom composition | Hydrogen, Carbon, Nitrogen, and Oxygen | Thermal hydrogen of Water, Carbon, Nitrogen, and Oxygen |
| Radiation source definition | Surface source (radius = 20 cm) | Environment source (radius = 25.9 cm) |
| Thermal neutron physics models | Not activated | Activated |

| | | |
|---|---|---|
| Total dose deposition in scoring volumes | Total dose deposition in a scoring volume was calculated by applying local approximation to secondary charged particles except protons and electrons. Both protons and electrons were allowed to interact freely. | Total dose deposition in a scoring volume was calculated by applying local approximation to all secondary charged particles except electrons which were allowed to interact freely. |

## Statistical uncertainty in Monte Carlo simulations

The statistical uncertainty in Monte Carlo simulations is typically estimated using the standard deviation (σ) of the mean for a given quantity. The uncertainty decreases as the number of histories (N) increases, following the relation:

$$\sigma_{mean} = \frac{\sigma}{\sqrt{N}}$$

where:

- σ is the standard deviation of individual simulation results (e.g., dose),
- N is the total number of independent histories.

## 6.1.6 Verifying secondary species spectra

The spectra of secondary species generated by neutrons in the inner, intermediate, and outer scoring volumes of the ICRU sphere, as modeled in TOPAS v3.6 in this project, were compared with those generated in Geant4 v10.06. Simulations were performed at three neutron energies (1 eV, 1 keV, and 1 MeV) for validation purposes throughout this study. Since Lund et al. (2020) [10] used Geant4 v10.04, we reperformed their simulations using Geant4 v10.06, as TOPAS v3.6 is based on the latter version of Geant4.

### 6.1.7 Verifying total dose deposition

Lund *et al.* (2020) [10] determined total dose deposition in a scoring volume by applying local approximation to heavy charged particles and allowing simulations of generated electrons and protons down to 0 eV. They also distinguished between the dose deposited by proton-generated electrons and that from γ-generated electrons. In this study, we validated that the local approximation could be applied to protons generated from neutrons up to an initial neutron energy of 10 MeV. Therefore, we used the local approximation to protons, while electrons were allowed to interact until they deposited their full energies.

Due to the difference in source radius - 20 cm for the Geant4 spherical surface source and 25.9 cm for the TOPAS environment source - a discrepancy in total dose deposition was observed. However, the relative dose contributions from all secondary species matched well. To assess the impact of the source radius difference on the total dose, we modeled a surface source with a 20 cm radius in TOPAS. Although the cosine angular distribution functionality was unavailable in TOPAS for a surface source, the total dose in all scoring volumes agreed well with the Geant4 results.

### 6.1.8 ICRU sphere and realistic neutron spectra in TOPAS

Next, the ICRU sphere phantom was irradiated using realistic neutron spectra from a 15 MeV linac, replacing the previously applied flat neutron spectrum. The realistic neutron spectra that were used were measured by Mathew *et al.* (2021) [52] at various locations within the bunker, as detailed in section 5.3.

### 6.1.9 In-vitro geometry simulation in TOPAS

Finally, an in-vitro geometry was simulated and irradiated with realistic neutron spectra to replicate an experimental scenario. A 75 cm² cell culture flask from SARSTEDT AG & Co. KG (51588 Nümbrecht, Germany,) was modeled in TOPAS. The flask, made up of polystyrene, had the dimensions outlined in Figure 6.3. To activate the thermal neutron physics models, the flask material was modified by replacing hydrogen with thermal hydrogen from water (TS_H_of_Water). The same physics models were used as in the

ICRU phantom irradiations. To simplify the modeling, the flask geometry was approximated as a cuboid. Nine scorers were placed throughout the flask volume to record the secondary species spectra and their corresponding doses. The flask was irradiated using the previously-described realistic neutron spectra that were measured at four locations: location A (100 cm from the isocenter), location B (200 cm from the isocenter), location C (at the maze junction), and location D (inside the maze), all employing the condensed history approach in Geant4. A screenshot of the TOPAS parameter file is shown in Figure 6.4.

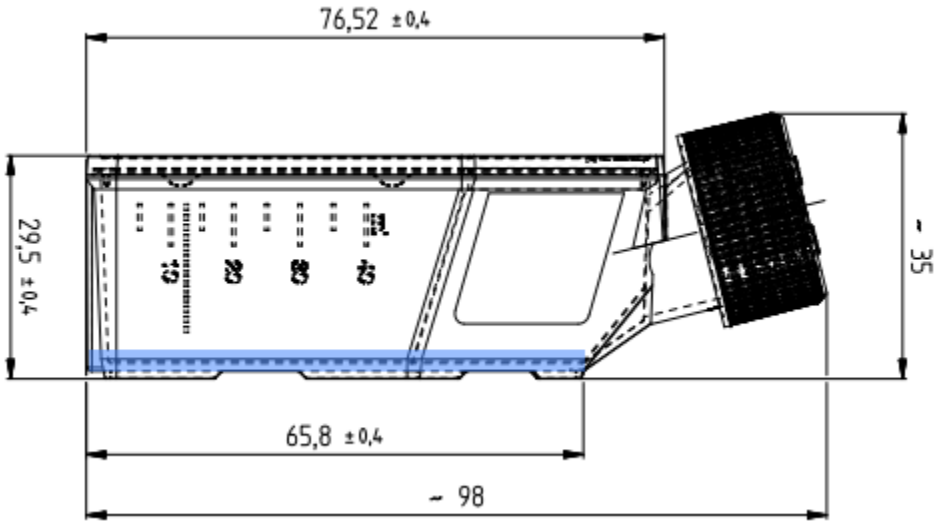


(a)

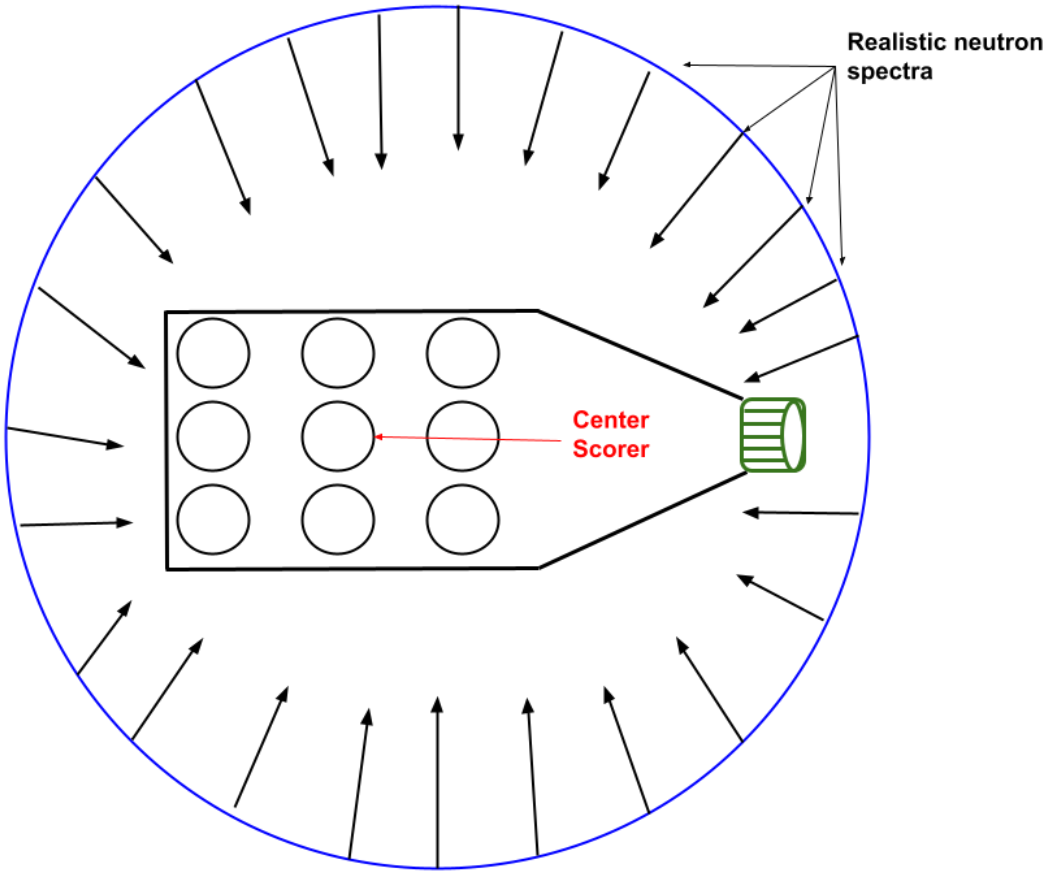


(b)

Figure 6.3 (a) Technical information of the 75 cm² cell culture flask. (b) A top-view of the flask geometry modeled in TOPAS, displaying the placement of various scoring volumes within the flask. The flask was irradiated using a realistic neutron spectrum, with the environment source indicated by the blue outline. Secondary species spectra were collected across all scoring volumes.

```
#flask material composition

s:El/TS_H_of_Water/Symbol              = "TS_H_of_Water"
sv:El/TS_H_of_Water/IsotopeNames       = 2 "H1" "H2"
uv:El/TS_H_of_Water/IsotopeAbundances = 2 99.98 0.02

i:Is/H1/Z = 1
i:Is/H1/N = 1
d:Is/H1/A = 1.007 g/mole

i:Is/H2/Z = 1
i:Is/H2/N = 2
d:Is/H2/A = 2.014 g/mole

i:El/TS_H_of_Water/AtomicNumber =  1
d:El/TS_H_of_Water/AtomicMass = 1.01 g/mole

sv:Ma/Polystyrene/Components = 2 "TS_H_of_Water" "Carbon"
uv:Ma/Polystyrene/Fractions = 2 0.077418 0.922582
d:Ma/Polystyrene/Density = 1.06 g/cm3
d:Ma/Polystyrene/MeanExcitationEnergy = 68.7 eV

sv:Ma/Water/Components = 2 "TS_H_of_Water" "Oxygen"
uv:Ma/Water/Fractions = 2 0.111894 0.888106
d:Ma/Water/Density = 1. g/cm3
d:Ma/Water/MeanExcitationEnergy = 75 eV
```

Figure 6.4 A screenshot of the TOPAS parameter file detailing the material composition of the flask and other relevant physical properties necessary for accurate modelling.

### 6.1.10 Track-structure simulations

The secondary species spectra recorded in the flask geometry for each location's realistic neutron spectrum were used to irradiate our geometric single-cell DNA model and thus calculate DNA damage yields and corresponding neutron RBEs. This was achieved by defining a volume source in TOPAS-nBio and employing track-structure simulations, as described in section 5.2.2. For the track-structure simulations, only electrons, protons, and oxygen ions were considered from the secondary species spectra, as the contributions of other species were negligible. However, previous studies by our research group, including Montgomery *et al.* (2021) and Manalad *et al.* (2023) [50], focused on electrons, protons, and α-particles to calculate DNA damage yields. In contrast, Baiocco *et al*. (2016) included a broader range of species, such as carbon, nitrogen, oxygen nuclei, deuterons, and α-particles, along with electrons and protons.

The primary distinction between this study and our previous research is the irradiation geometry and the use of realistic neutron spectra, as opposed to the flat neutron spectrum as well as the use of TOPAS rather than Geant4. Using the same simulation parameters as in the study by Manalad *et al.* (2023) [50], separate simulations were conducted for all three species (electrons, protons, and oxygen ions) across the four realistic spectra locations. A cumulative dose of 1 Gy was delivered at each scoring location in the flask geometry to facilitate comparisons with our earlier work and the broader literature. DNA damage yields for complex DSB clusters were analyzed for each simulation. The RBE of the realistic neutron spectra at locations A, B, C, and D in the central scoring volume of the flask geometry was determined by calculating the ratio of DNA damage yields induced by neutrons to those induced by reference X-rays. Additionally, simulations were repeated for doses of 0.1 Gy, 0.5 Gy, 1.5 Gy, 2.0 Gy, 2.5 Gy, 3.0 Gy, and 5.0 Gy to evaluate RBE as a function of dose at each location.

# Chapter 7

# Results

## 7.1 Charged particle spectra in the ICRU sphere phantom

We modeled an ICRU sphere geometry with three distinct scoring volumes (inner, intermediate, and outer) in TOPAS v3.6. Simulations were performed with monoenergetic neutron sources with initial kinetic energies of 1keV, 1 MeV, and 10 MeV. Figure 7.1 presents the spectra of secondary species including protons, deuterons, α-particles, and various ions (carbon, nitrogen, oxygen) - produced by neutron interactions with the ICRU phantom. Secondary particles such as tritons, beryllium, and boron were excluded due to their insignificant quantities. Results will be discussed in section 8.1.

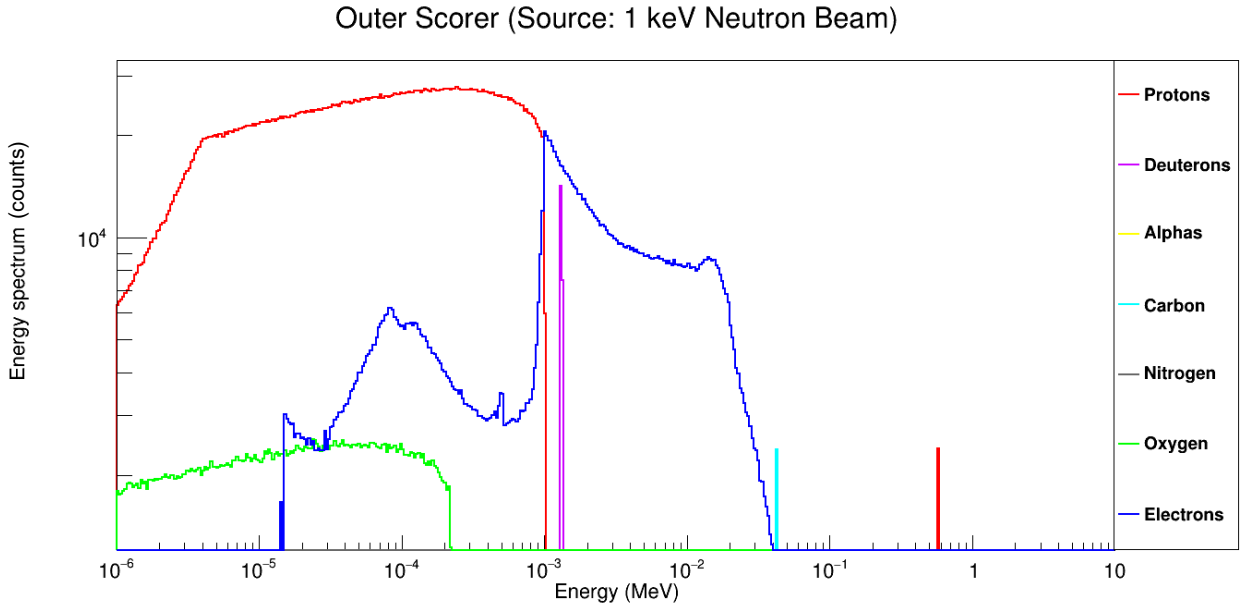


(a1)

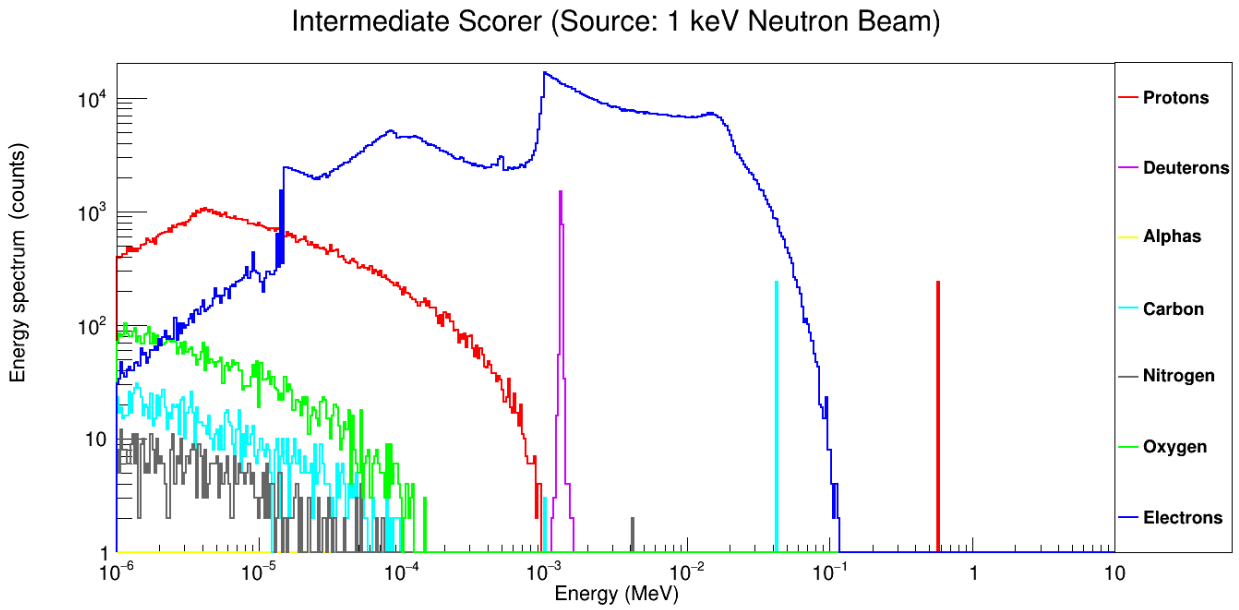
Intermediate Scorer (Source: 1 keV Neutron Beam)
Energy spectrum (counts)
Energy (MeV)
Protons
Deuterons
Alphas
Carbon
Nitrogen
Oxygen
Electrons

(a2)

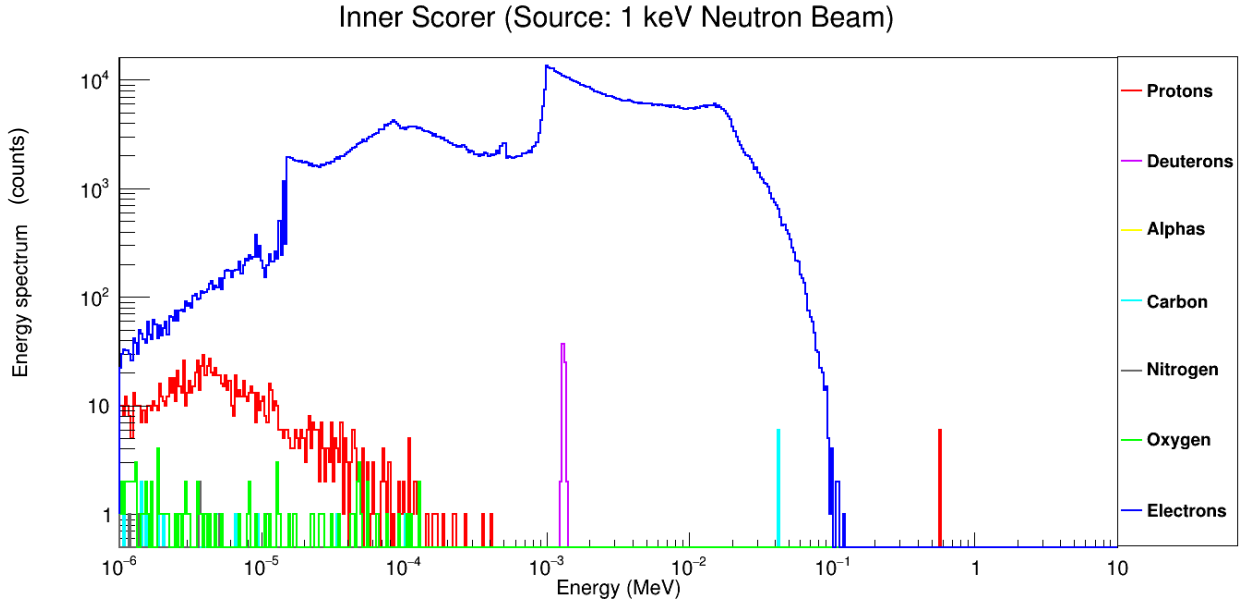
Inner Scorer (Source: 1 keV Neutron Beam)
Energy spectrum (counts)
Energy (MeV)
Protons
Deuterons
Alphas
Carbon
Nitrogen
Oxygen
Electrons

(a3)

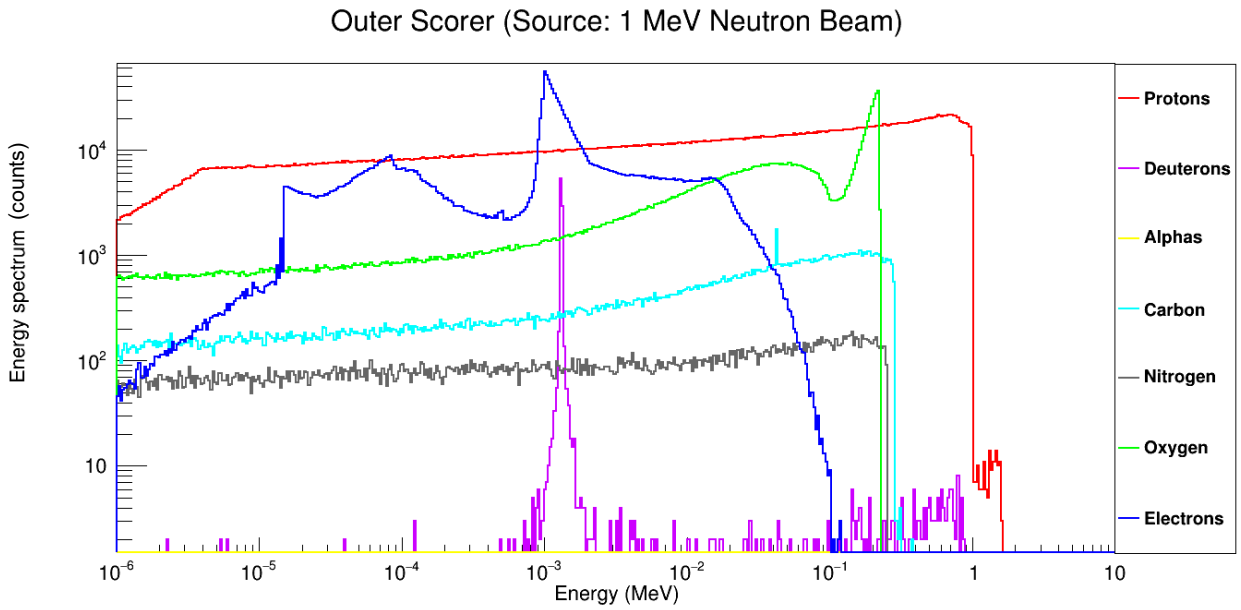
Outer Scorer (Source: 1 MeV Neutron Beam)
Energy spectrum (counts)
Energy (MeV)
Protons
Deuterons
Alphas
Carbon
Nitrogen
Oxygen
Electrons

(b1)

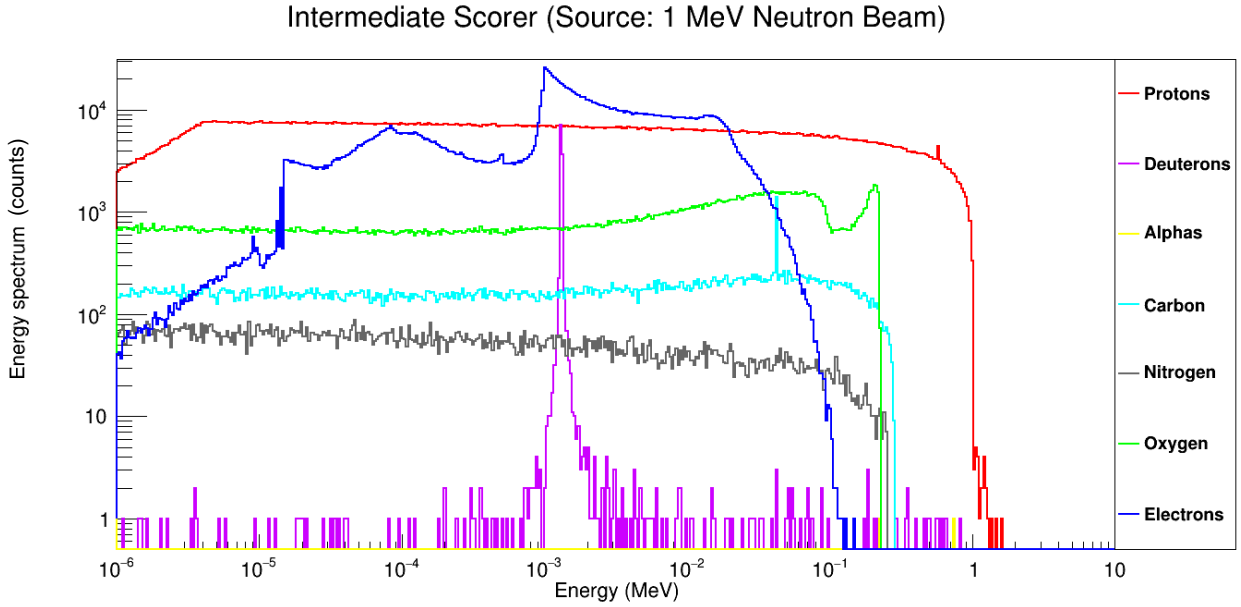
Intermediate Scorer (Source: 1 MeV Neutron Beam)
Energy spectrum (counts)
Energy (MeV)
Protons
Deuterons
Alphas
Carbon
Nitrogen
Oxygen
Electrons

(b2)

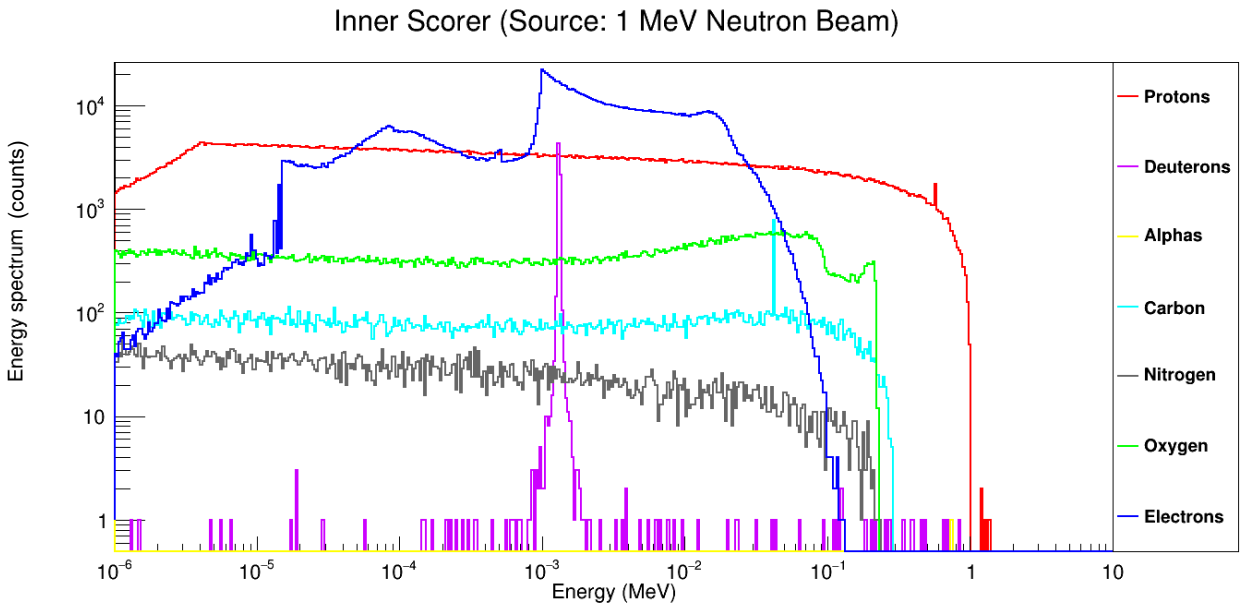
Inner Scorer (Source: 1 MeV Neutron Beam)
Energy spectrum (counts)
Energy (MeV)
Protons
Deuterons
Alphas
Carbon
Nitrogen
Oxygen
Electrons

(b3)

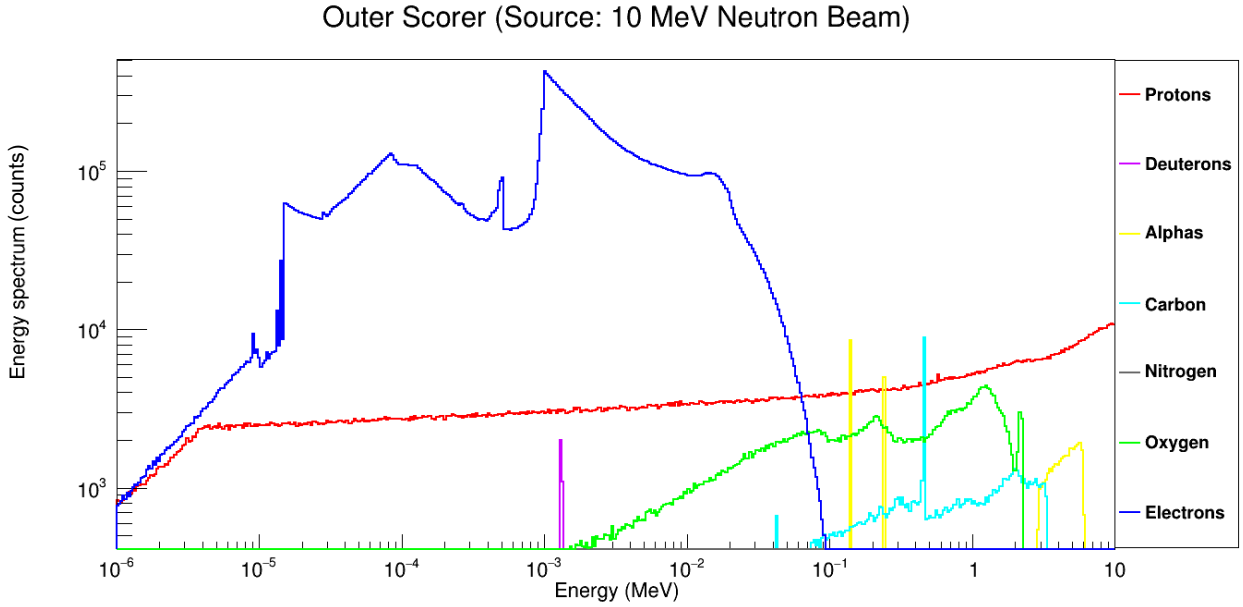
Outer Scorer (Source: 10 MeV Neutron Beam)
Energy spectrum (counts)
Energy (MeV)
Protons
Deuterons
Alphas
Carbon
Nitrogen
Oxygen
Electrons

(c1)

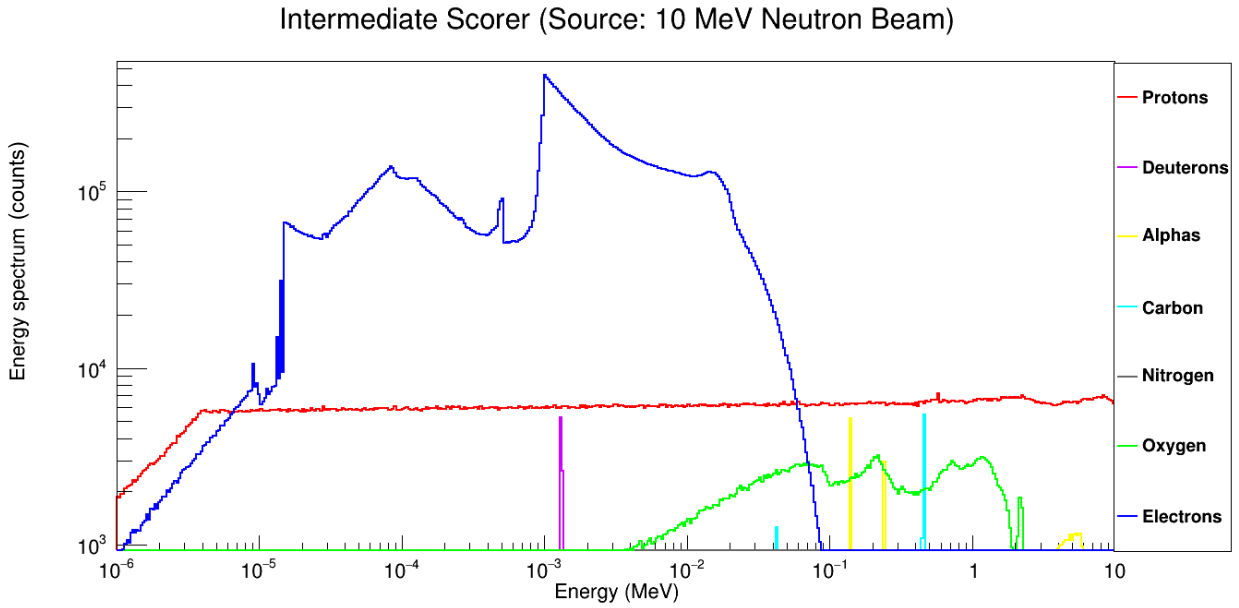


(c2)

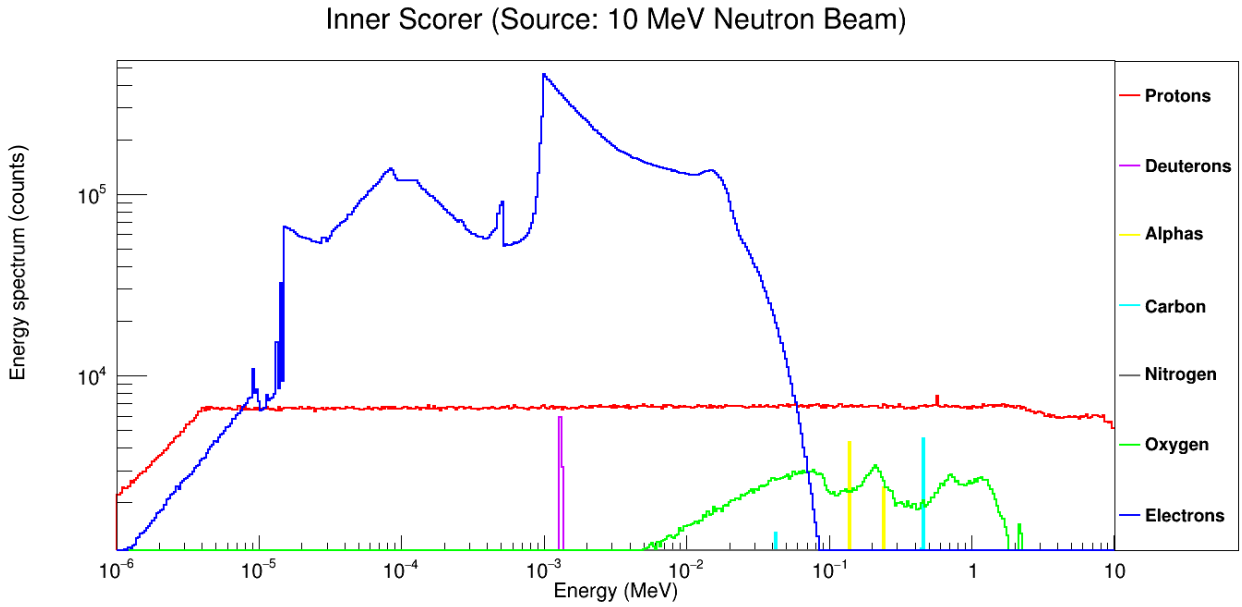


(c3)

Figure 7.1 Secondary charged particle spectra produced in three scoring volumes by monoenergetic neutron sources. The spectra are presented in order of increasing depth (outer, intermediate, and inner scoring volumes) and neutron energy from top to bottom: (a) 1 keV, (b) 1 MeV, and (c) 10 MeV.

## 7.2 Relative dose contributions

The relative dose contributions of secondary species were evaluated in each of the three scoring volumes across all investigated neutron energies. As shown in Figure 7.2, at low neutron energy (1 keV), the majority of the dose was deposited by electrons, whereas the contribution from protons increased significantly at higher energies (1 MeV and 10 MeV).

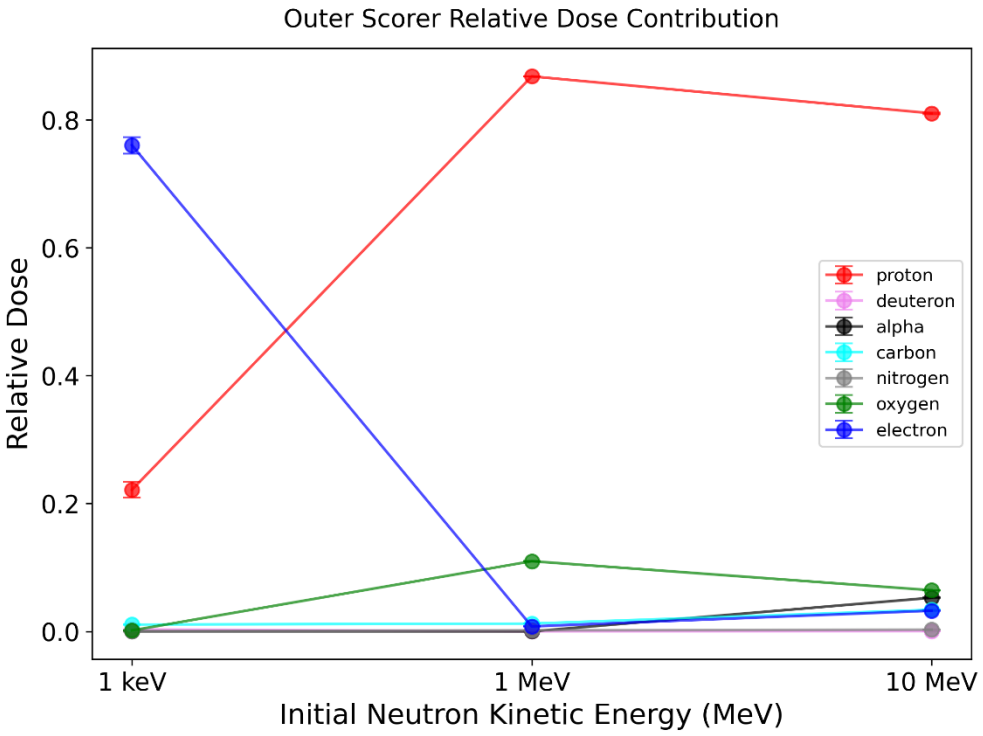


(a)

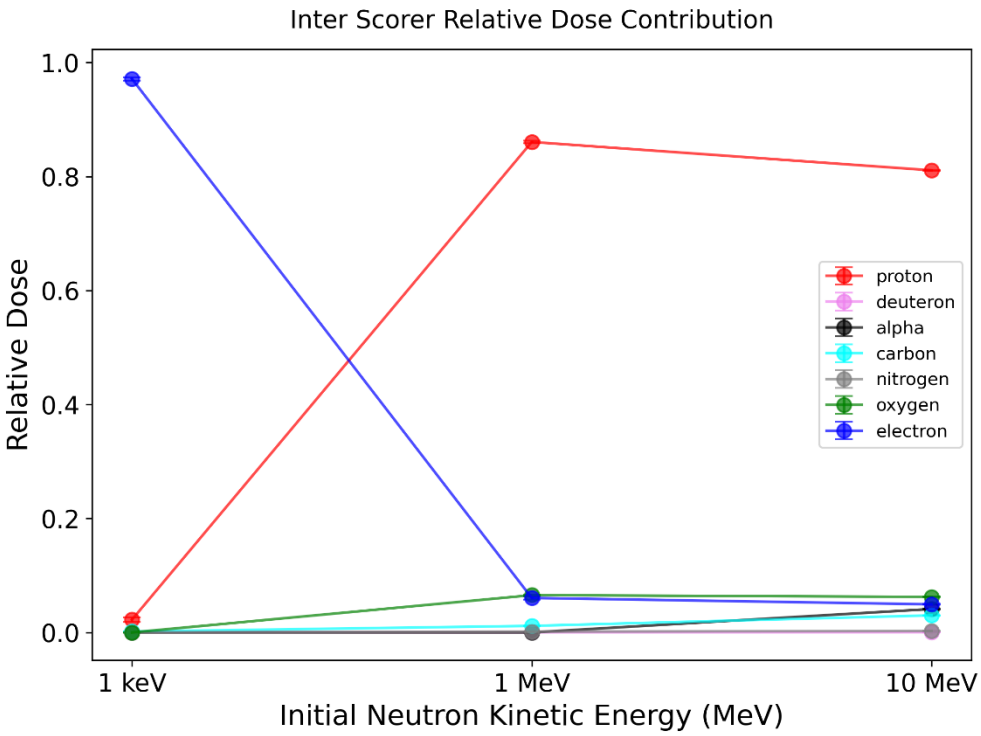
Inter Scorer Relative Dose Contribution
Relative Dose
1.0
0.8
0.6
0.4
0.2
0.0
1 keV
1 MeV
10 MeV
Initial Neutron Kinetic Energy (MeV)
proton
deuteron
alpha
carbon
nitrogen
oxygen
electron

(b)

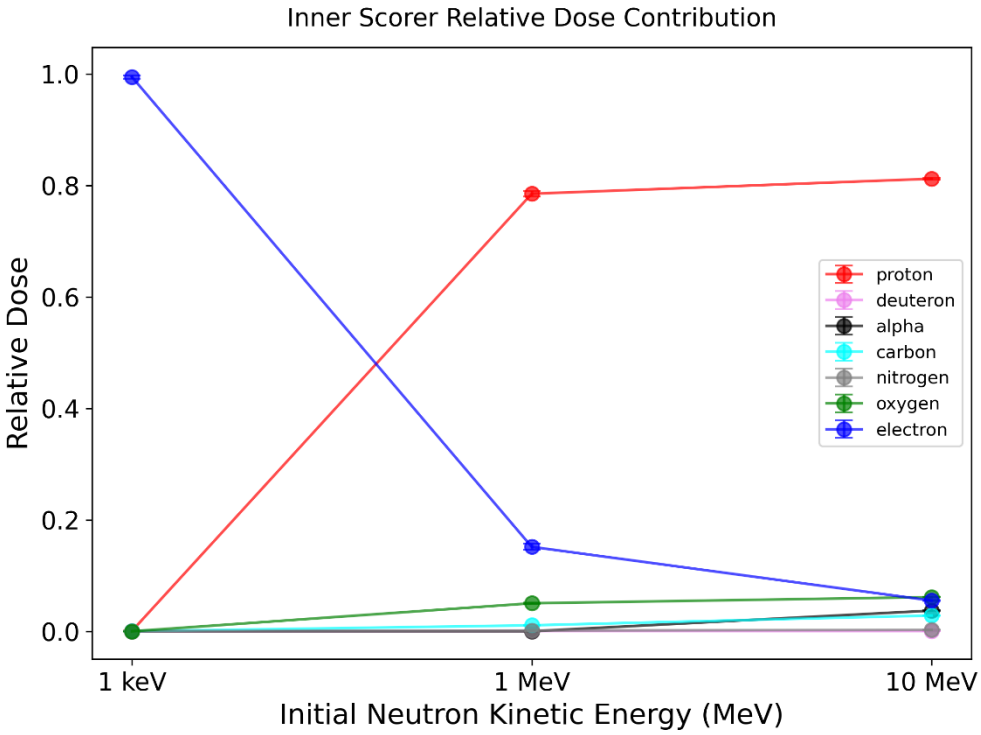
Inner Scorer Relative Dose Contribution
Relative Dose
1.0
0.8
0.6
0.4
0.2
0.0
1 keV
1 MeV
10 MeV
Initial Neutron Kinetic Energy (MeV)
proton
deuteron
alpha
carbon
nitrogen
oxygen
electron

(c)

Figure 7.2 Relative dose contributions in (a) outer, (b) intermediate, and (c) inner scoring volumes for neutron energies of 1 keV, 1 MeV, and 10 MeV. The local approximation was used for all secondary charged particles in the dose calculations, except for electrons, which were allowed to interact freely. Error bars represent the standard uncertainty around the mean of 10 simulation runs each with $10^8$ primary particle simulations.

## 7.3 Transition from Geant4 v10.04 to Geant4 v10.06

The transition from Geant4 v10.04 to v10.06 introduced several updates and improvements to the hadronic physics models. Specifically, the latest versions of the Fritiof (FTF) and Quark-Gluon-String (QGS) string models were released in Geant4 v10.05, marking their first update since v10.2. Additionally, Geant4 v10.06 introduced Glauber-Gribov cross-sections for both elastic and inelastic hadron-nucleus interactions, along with new γ-nuclear models based on pre-compound de-excitation processes. These updates made the hadronic physics models in Geant4 v10.06 more accurate for neutron transport simulations compared to those in v10.04. The improvement in the underlying hadronic physics models from Geant4 v10.04 to Geant4 v10.06 was validated by comparing the changes in electron spectra observed in the intermediate scoring volume of the ICRU phantom for 1 MeV neutron simulations performed in both versions. Figure 7.3 illustrates this comparison. The electron spectra were recorded in both Geant4 versions using the local approximation for electrons, as described by Lund *et al.* (2020) [10], for the purpose of comparison.

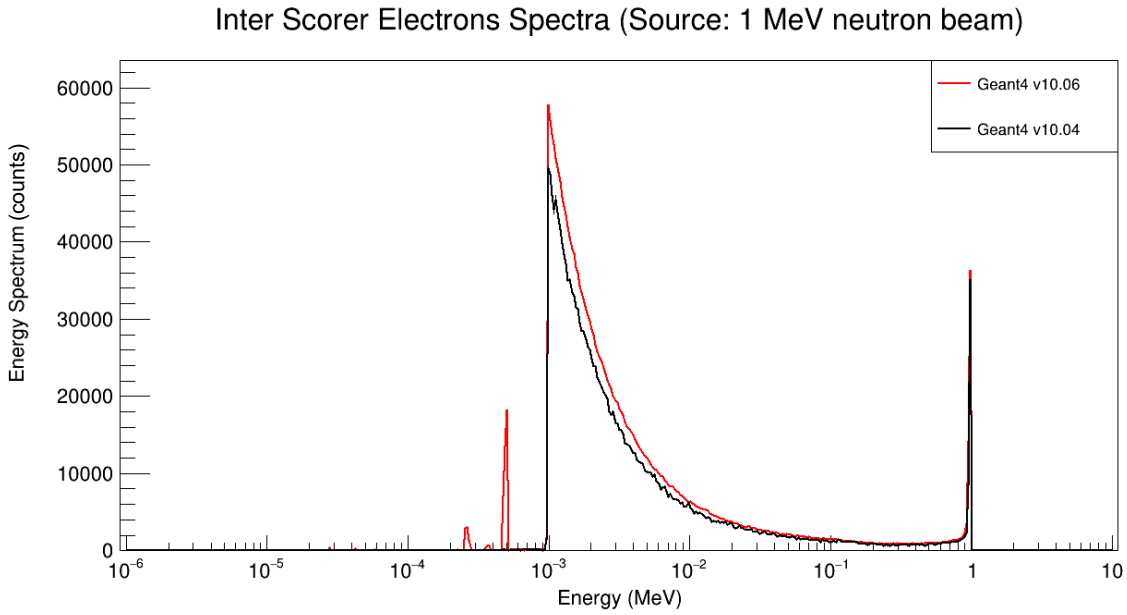


Figure 7.3 Comparison of electron spectra recorded in the intermediate scoring volume of the ICRU phantom for 1 MeV neutron simulations in Geant4 v10.04 and Geant4 v10.06. The electron spectra were obtained using the local approximation for electrons, as described by Lund *et al.* (2020) [10].

## 7.4 Comparison with Geant4 v10.06

As mentioned previously, Lund *et al.* (2020) [10] conducted simulations using Geant4 v10.04, while this study uses TOPAS v3.6, which is based on Geant4 v10.06. To ensure consistency and a valid comparison, all secondary species spectra were re-measured using Geant4 v10.06. This allowed for a direct comparison with the spectra generated in the current study. Figure 7.4 compares proton spectra collected in the intermediate scoring volume at neutron energies of 1 keV, 1 MeV, and 10 MeV. In Geant4 v10.06, the ICRU phantom material was constructed using standard hydrogen, following the approach of Lund *et al.* (2020) [10]. However, in TOPAS v3.6, thermal hydrogen of water (TS_H_of_Water) was used instead of standard hydrogen. This led to a discrepancy in the proton spectra in the thermal neutron range, as the thermal neutron models were not activated in Geant4 v10.06 due to the absence of thermal hydrogen of water.

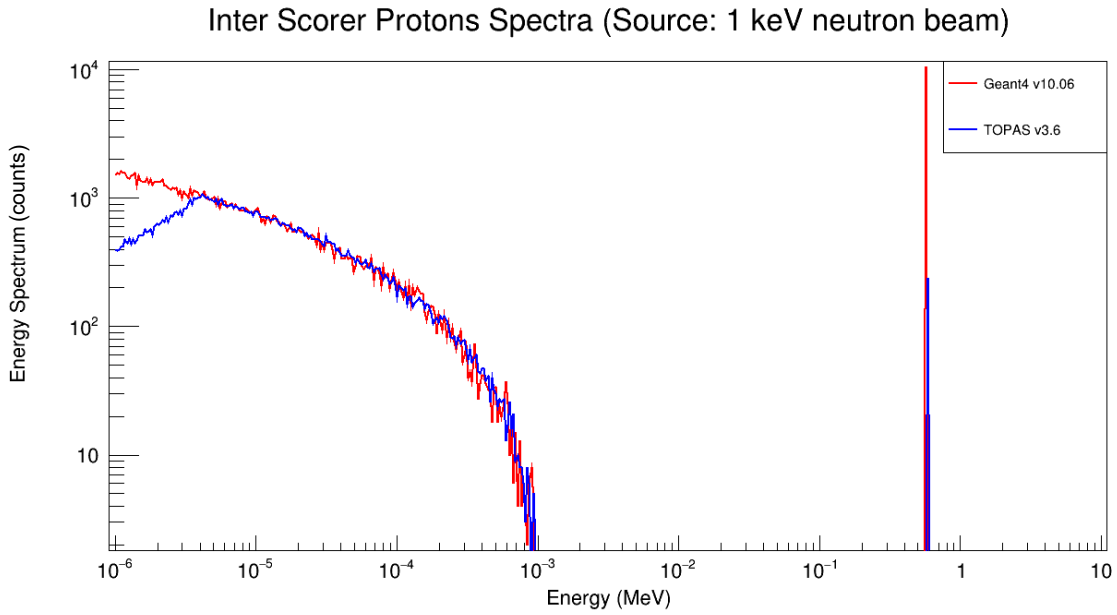
Inter Scorer Protons Spectra (Source: 1 keV neutron beam)
Energy Spectrum (counts)
Energy (MeV)
Geant4 v10.06
TOPAS v3.6

(a)

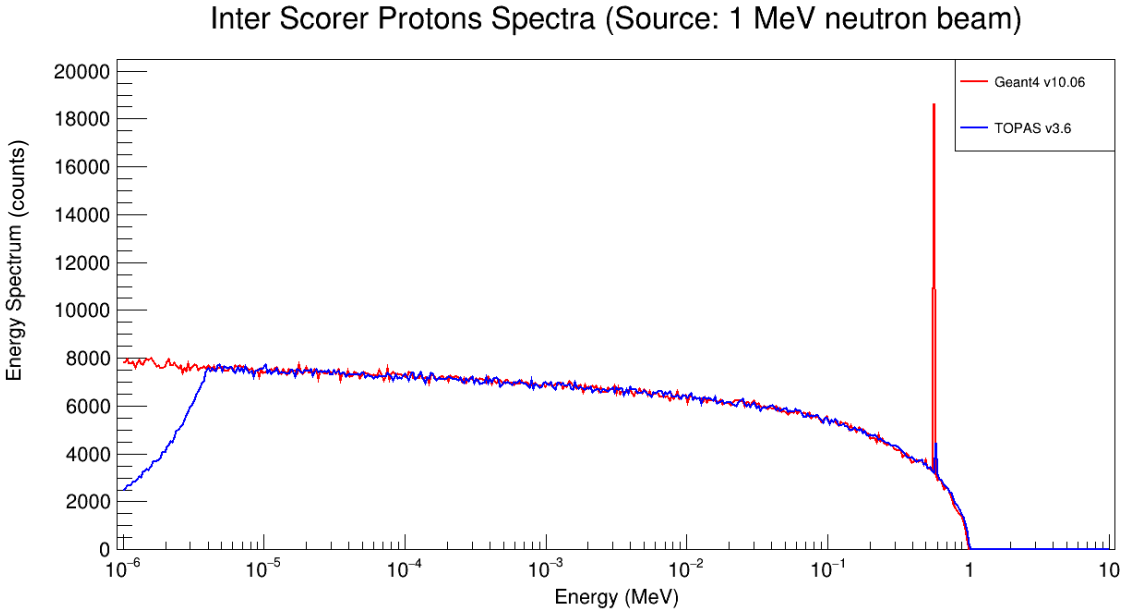
Inter Scorer Protons Spectra (Source: 1 MeV neutron beam)
Energy Spectrum (counts)
Energy (MeV)
Geant4 v10.06
TOPAS v3.6

(b)

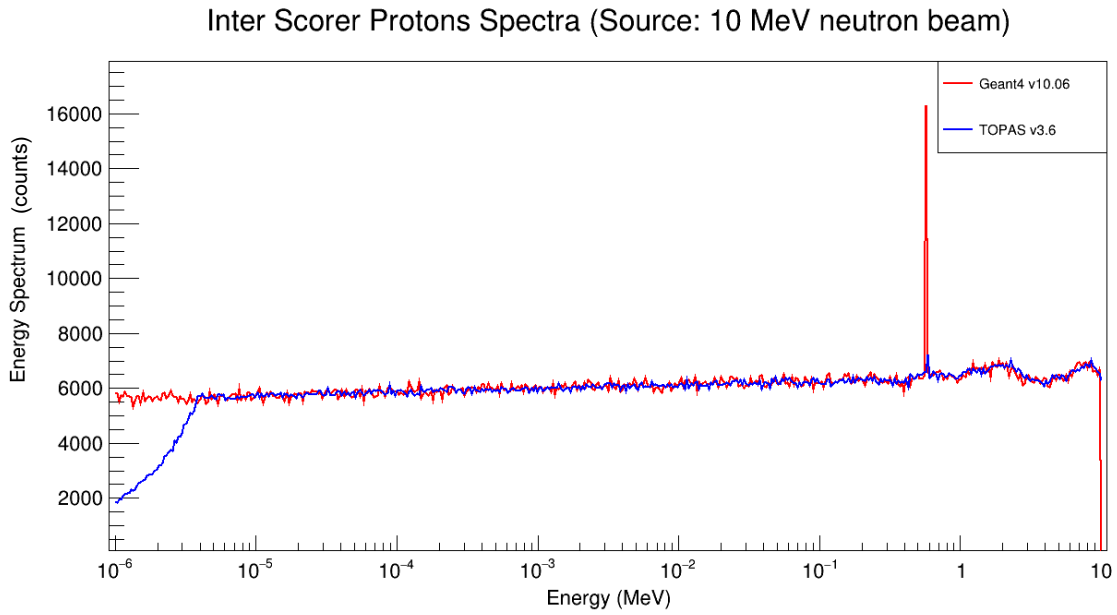


(c)

Figure 7.4 Comparison of proton spectra recorded in the intermediate scoring volume of the ICRU phantom between Geant4 v10.06 and TOPAS v3.6 (with thermal hydrogen of water turned on) for the three investigated monoenergetic neutron energies: (a) 1keV, (b) 1 MeV, and (c) 10 MeV.

## 7.5 The influence of thermal hydrogen of water

To assess the impact of rebuilding the ICRU phantom material with thermal hydrogen of water (TS_H_of_Water) on secondary species spectra in Geant4, the proton spectra within the intermediate scoring volume were compared at neutron kinetic energies of 1 keV, 1 MeV, and 10 MeV. The results of this comparison are presented in Figure 7.5.

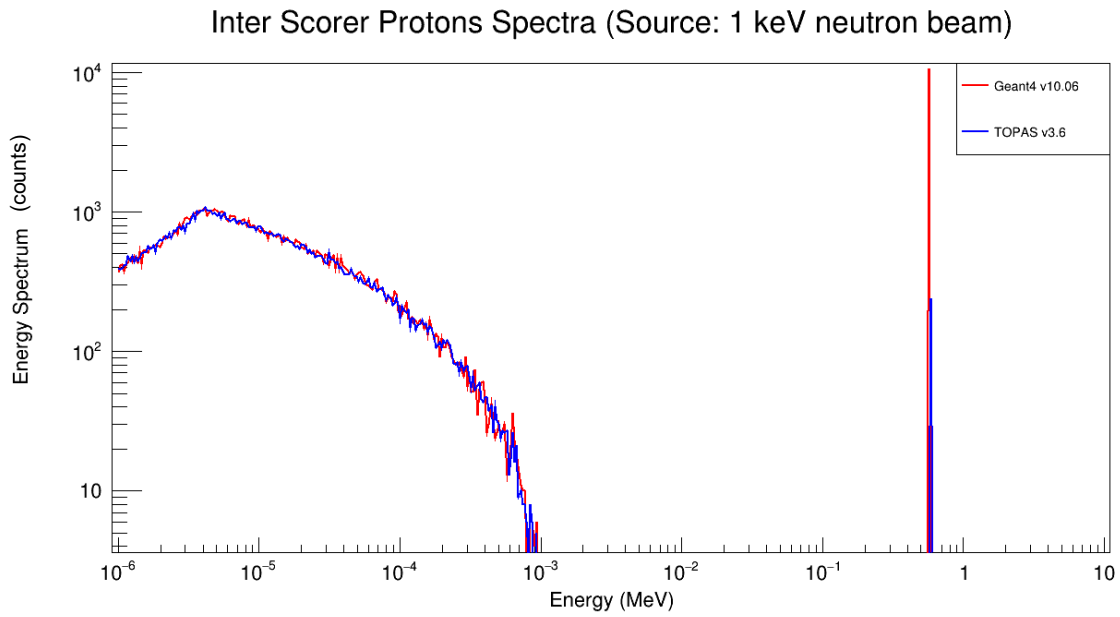
Inter Scorer Protons Spectra (Source: 1 keV neutron beam)
Energy Spectrum (counts)
Energy (MeV)
Geant4 v10.06
TOPAS v3.6

(a)

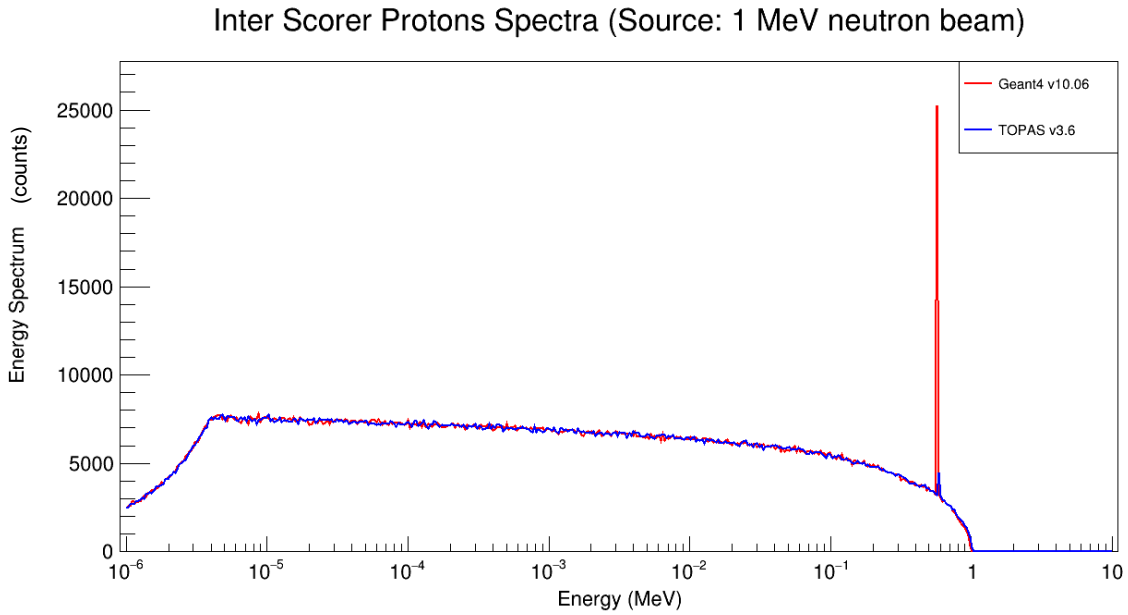
Inter Scorer Protons Spectra (Source: 1 MeV neutron beam)
Energy Spectrum (counts)
Energy (MeV)
Geant4 v10.06
TOPAS v3.6

(b)

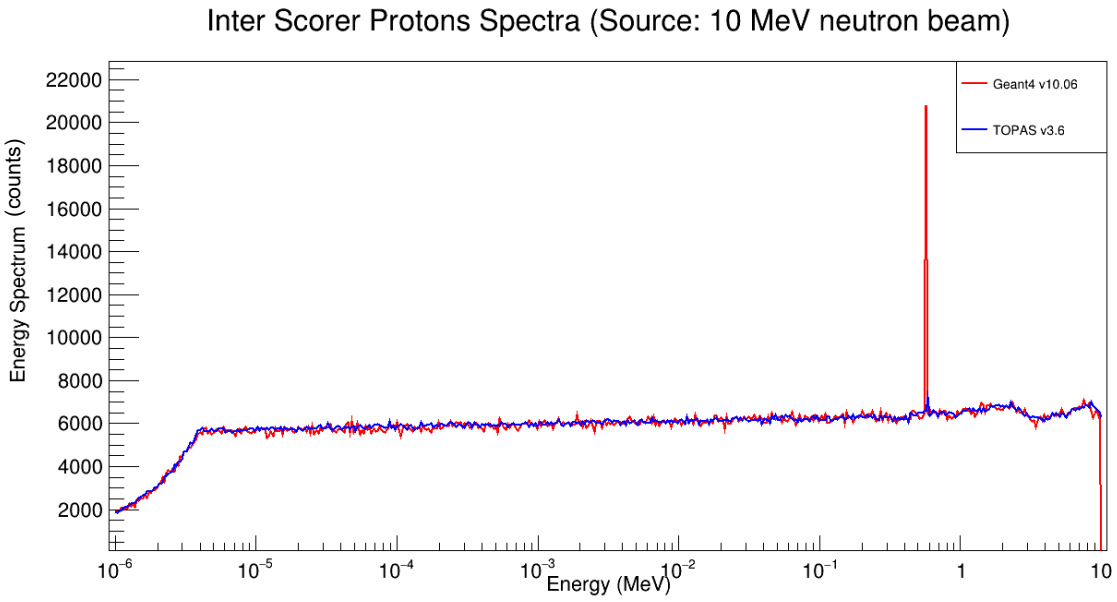


(c)

Figure 7.5 Comparison of proton spectra recorded in the intermediate scoring volume of the ICRU phantom, rebuilt using thermal hydrogen of water, between Geant4 v10.06 and TOPAS v3.6 for the three investigated monoenergetic neutron energies: (a) 1keV, (b) 1 MeV, and (c) 10 MeV.

## 7.6 Local approximation condition and high-energy electrons

Lund *et al.* (2020) [10] terminated the tracking of heavy charged particles and electrons with energies below 1 MeV at their point of origin to achieve a local approximation condition (as discussed in Section 5.2.2). In contrast, we allowed electrons to interact freely, recording their energy deposition down to 0 eV. The energy deposition by electrons liberated through secondary γ interactions within the ICRU material during neutron irradiations at 1 keV, 1 MeV, and 10 MeV are shown in Figure 7.1. Lund *et al.* (2020) [10] recorded the initial kinetic energy of electrons and treated it as their dose deposition under the local approximation condition. A comparison between the electron energy deposition in our study and the electron spectra reported by Lund *et al.* (2020) [10] in the intermediate scoring volume is presented in Figure 7.6.

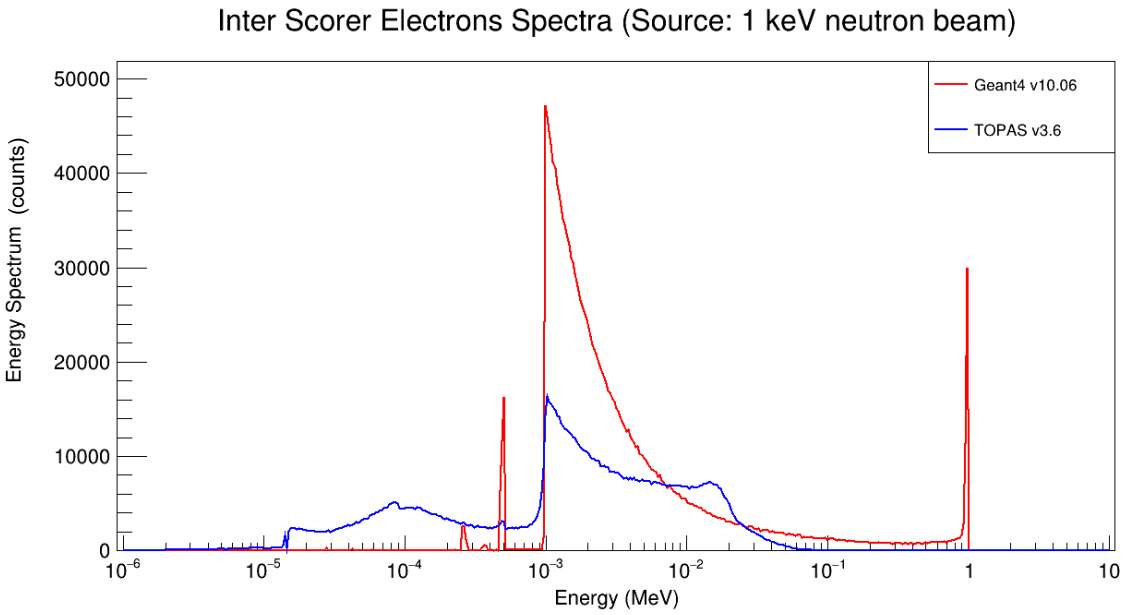
Inter Scorer Electrons Spectra (Source: 1 keV neutron beam)
Geant4 v10.06
TOPAS v3.6
Energy Spectrum (counts)
Energy (MeV)
0
10000
20000
30000
40000
50000
$10^{-6}$
$10^{-5}$
$10^{-4}$
$10^{-3}$
$10^{-2}$
$10^{-1}$
1
10

(a)

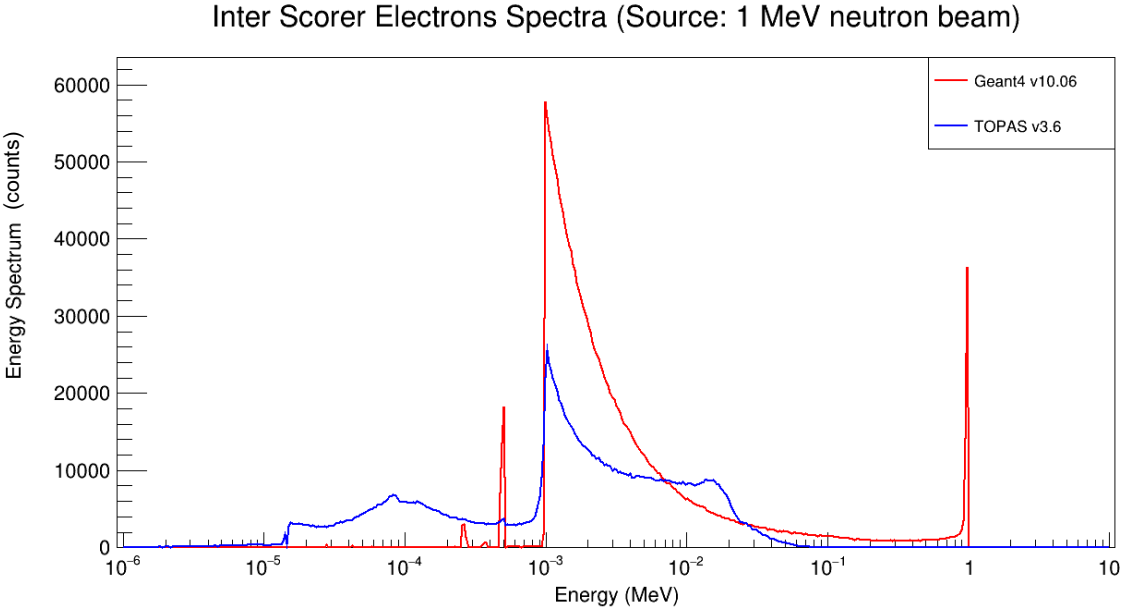
Inter Scorer Electrons Spectra (Source: 1 MeV neutron beam)
Geant4 v10.06
TOPAS v3.6
Energy Spectrum (counts)
Energy (MeV)
0
10000
20000
30000
40000
50000
60000
$10^{-6}$
$10^{-5}$
$10^{-4}$
$10^{-3}$
$10^{-2}$
$10^{-1}$
1
10

(b)

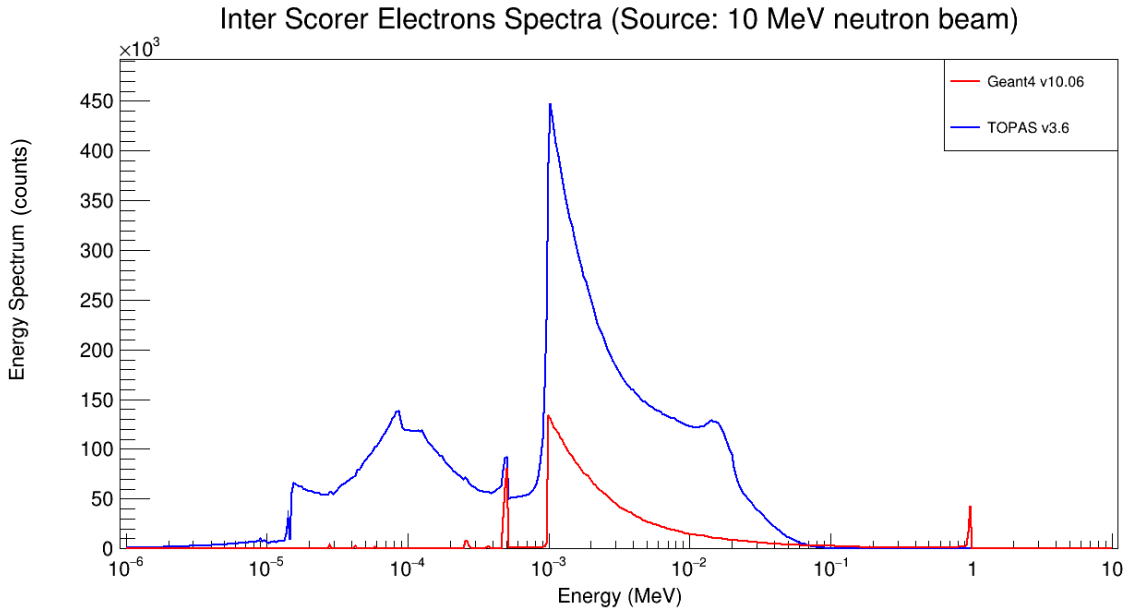


(c)

Figure 7.6 Comparison of electron energy deposition in the intermediate scoring volume of the ICRU phantom between this study and Lund *et al.* (2020) [10] for neutron energies of 1 keV (a), 1 MeV (b), and 10 MeV (c).

## 7.7 Relative dose calculation in the ICRU sphere phantom

A comparison of the relative dose contributions of each secondary species in the inner scoring volume for the neutron energies mentioned above with Lund *et al.* (2020) [10] is presented in Table 7.1. The relative dose contributions obtained in this study show a strong agreement with Lund *et al.* (2020) [10].

Table 7.1 Comparison of relative dose contributions from each secondary species between Lund *et al.* (2020) [10] and this study within the inner scoring for initial neutron energies of 1 keV, 1 MeV, and 10 eV.

| Particle | Lund *et al.* (2020) [10] | | | This study | | |
|---|---|---|---|---|---|---|
| | 1 keV | 1 MeV | 10 MeV | 1 keV | 1 MeV | 10 MeV |
| Proton | 0.002 ± 0.0002 | 0.768 ± 0.089 | 0.8 ± 0.063 | 0.0007 ± 0.0005 | 0.785 ± 0.0049 | 0.811 ± 0.0014 |
| Deuteron | 0 | 0 | 0 | 1.76E-05 ± 5.66E-06 | 0.0003 ± 0.0001 | 0.0002 ± 5.61E-05 |
| Triton | 0 | 0 | 0 | 0 | 0 | 0.0001 ± 4.38E-05 |
| α-particles | 0 | 0 | 0.043 ± 0.003 | 0 | 1.5E-05 ± 4.54E-05 | 0.037 ± 0.0007 |
| Beryllium | 0 | 0 | 0.002 ± 0.0001 | 0 | 0 | 0.0007 ± 2.4E-05 |
| Boron | 0 | 0 | 0.001 ± 8.24E-05 | 0 | 0 | 0.0007 ± 0.0001 |
| Carbon | 0 | 0.011 ± 0.001 | 0.029 ± 0.002 | 5.1E-05 ± 4.21E-05 | 0.010 ± 0.0002 | 0.028 ± 0.0003 |
| Nitrogen | 0 | 0.001 ± 0.0001 | 0.003 ± 0.0002 | 2.94E-08 ± 6.22E-08 | 0.0012 ± 0.0001 | 0.002 ± 0.0001 |
| Oxygen | 0 | 0.049 ± 0.005 | 0.061 ± 0.004 | 3.4E-07 ± 2.23E-07 | 0.050 ± 0.0009 | 0.061 ± 0.0004 |
| Electron | 0.989 ± 0.023 | 0.125 ± 0.0143 | 0.030 ± 0.002 | 0.994 ± 0.003 | 0.151 ± 0.005 | 0.055 ± 0.0005 |

### 7.7.1 Total dose

A discrepancy was observed in the total dose recorded in Geant4 and TOPAS across the three scoring volumes. This was due to a difference in the diameter of the spherical source used to irradiate the ICRU sphere in Geant4 and TOPAS (discussed in section 6.1.5). However, when a spherical source with the same diameter as the one used in Geant4 was modeled in TOPAS, the total dose showed good agreement between the two simulations.

## 7.8 Charged particle spectra in the ICRU sphere phantom using realistic spectra of neutrons

In the next step, we replaced the flat spectrum of neutrons consisting of three monoenergetic energies (1 keV, 1 MeV, and 10 MeV) with the realistic neutron spectra measured by Mathew *et al.* (2021) [52] at locations A, B, C, and D in 15 MV linac bunker to irradiate the phantom. The resulting secondary species spectra recorded in the intermediate scoring volume of the ICRU phantom are plotted in Figure 7.7.

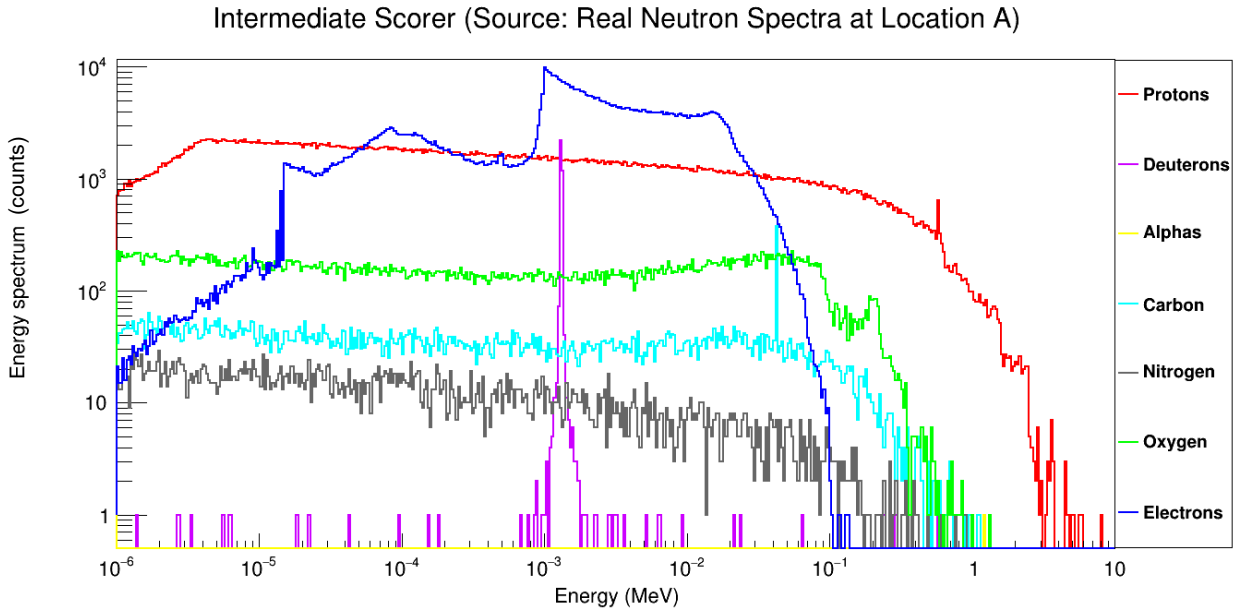


(a)

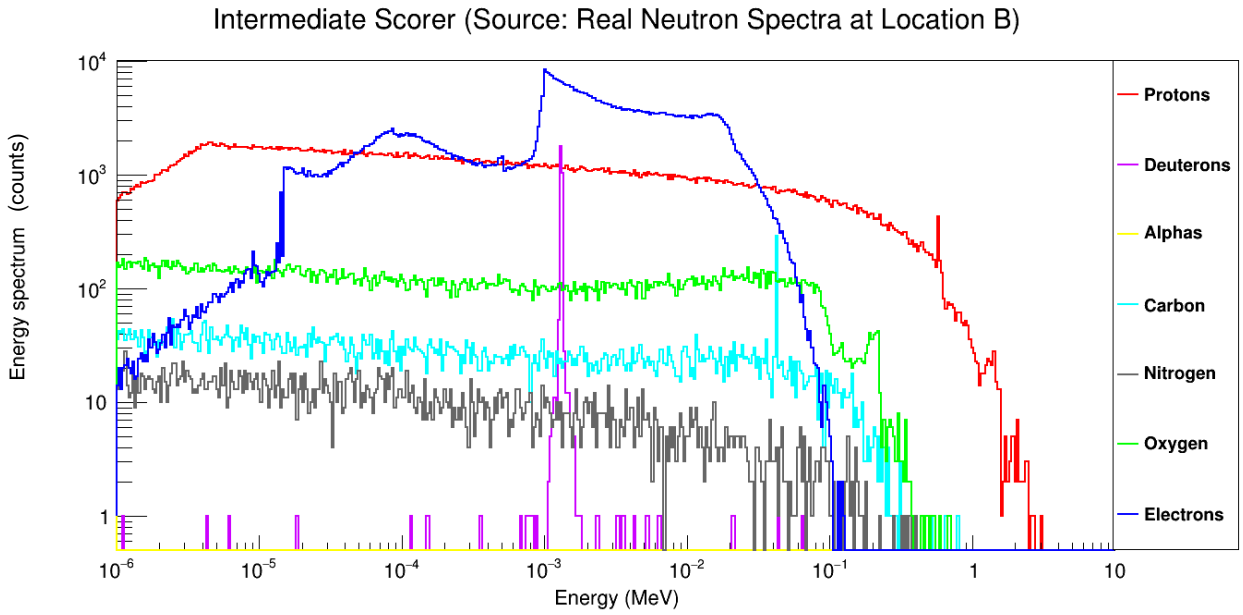
Intermediate Scorer (Source: Real Neutron Spectra at Location B)
Energy spectrum (counts)
Energy (MeV)
Protons
Deuterons
Alphas
Carbon
Nitrogen
Oxygen
Electrons

(b)

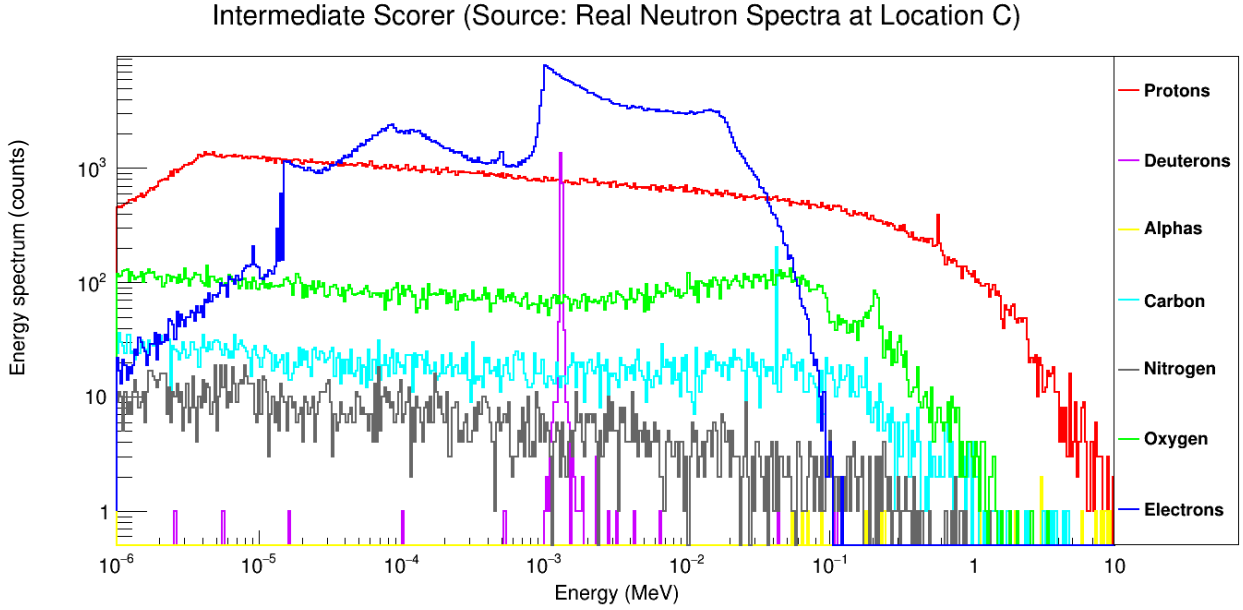
Intermediate Scorer (Source: Real Neutron Spectra at Location C)
Energy spectrum (counts)
Energy (MeV)
Protons
Deuterons
Alphas
Carbon
Nitrogen
Oxygen
Electrons

(c)

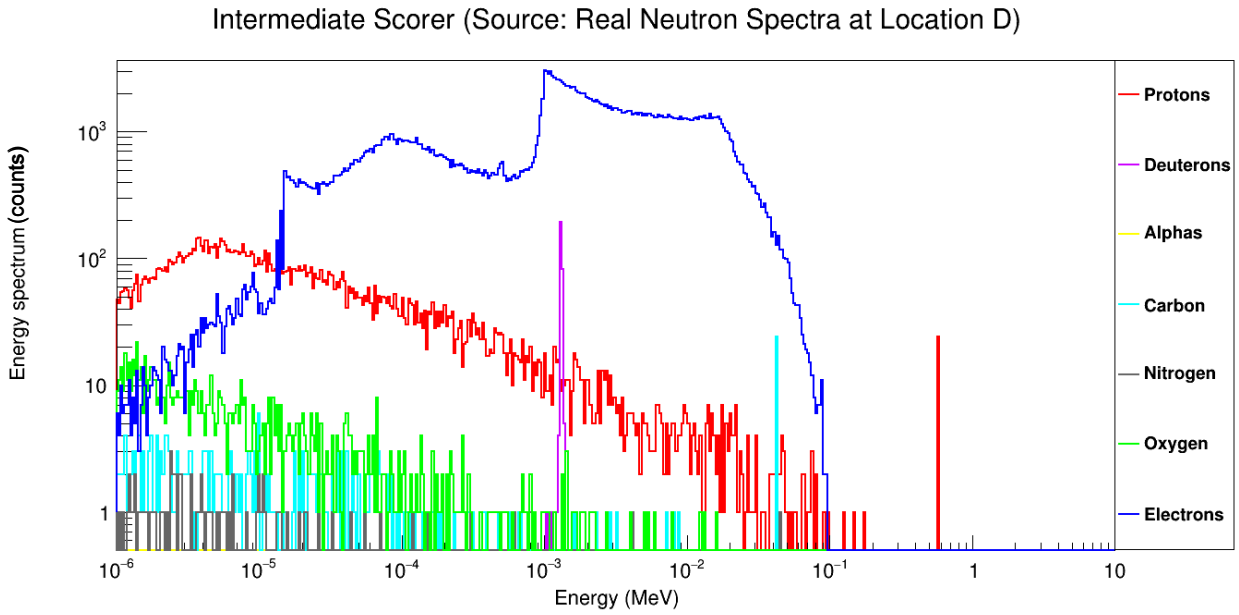


(d)

Figure 7.7 Spectra of secondary charged particles produced in the intermediate scoring volume of the ICRU phantom irradiated with realistic neutron spectra from Location A (a), Location B (b), Location C (c), and Location D. The phantom was irradiated isotropically using the environment source definition in TOPAS.

## 7.9 In-vitro geometry and realistic spectra of neutron

In the final step, the phantom geometry was replaced with an in-vitro flask geometry. Simulations were then performed using the realistic neutron spectra measured at all locations. The secondary species spectra and their relative dose contributions were recorded in all nine scoring volumes defined within the flask geometry. All results presented in this thesis for flask geometry simulations are based solely on the center scoring volume, which is defined at the center of the flask (see Figure 6.3).

### 7.9.1 Measurement of charged particle spectra

Figure 7.8 shows the spectra of all secondary species recorded in the center scoring volume of the flask for the realistic neutron spectra measured at locations A, B, C, and D.

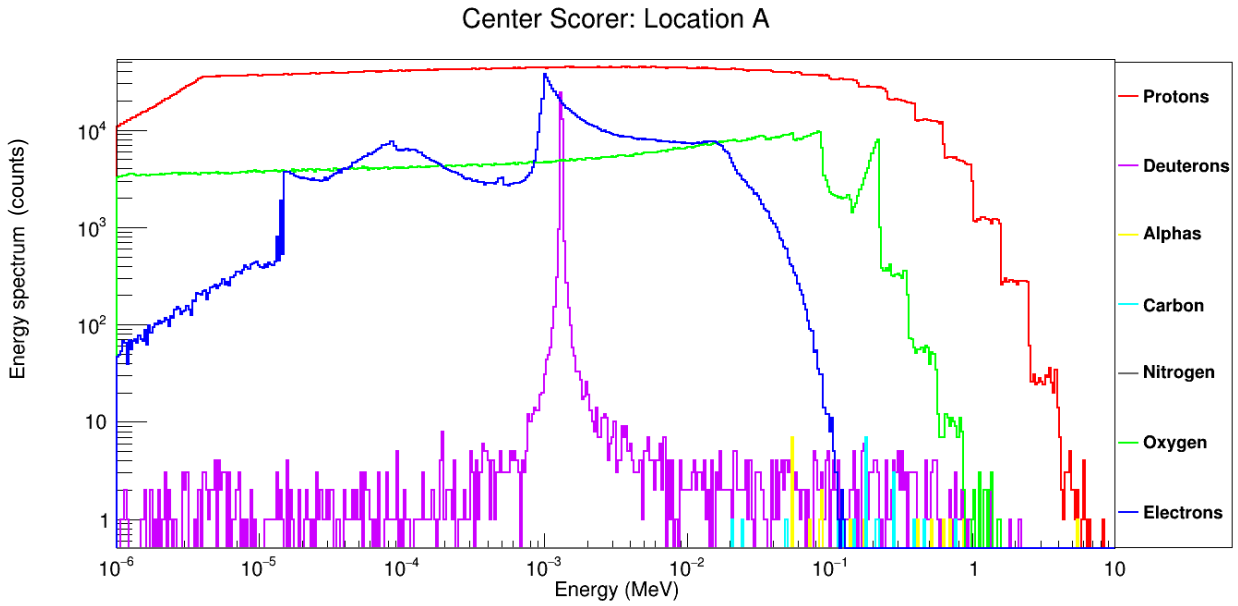
Center Scorer: Location A
Energy spectrum (counts)
Energy (MeV)
Protons
Deuterons
Alphas
Carbon
Nitrogen
Oxygen
Electrons

(a)

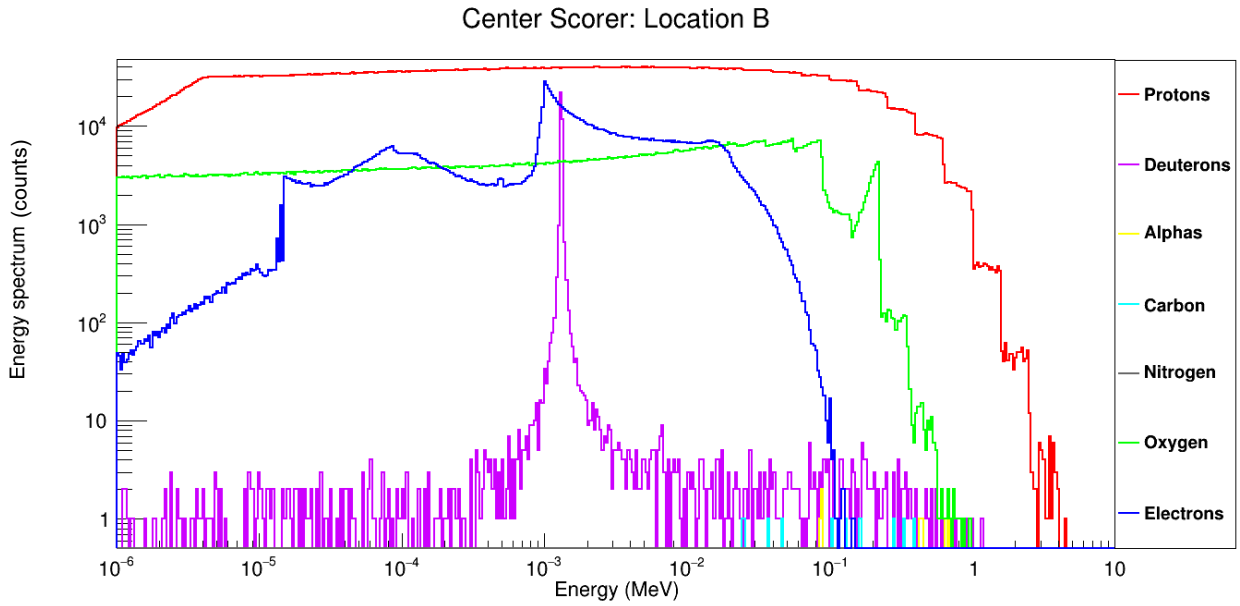
Center Scorer: Location B
Energy spectrum (counts)
Energy (MeV)
Protons
Deuterons
Alphas
Carbon
Nitrogen
Oxygen
Electrons

(b)

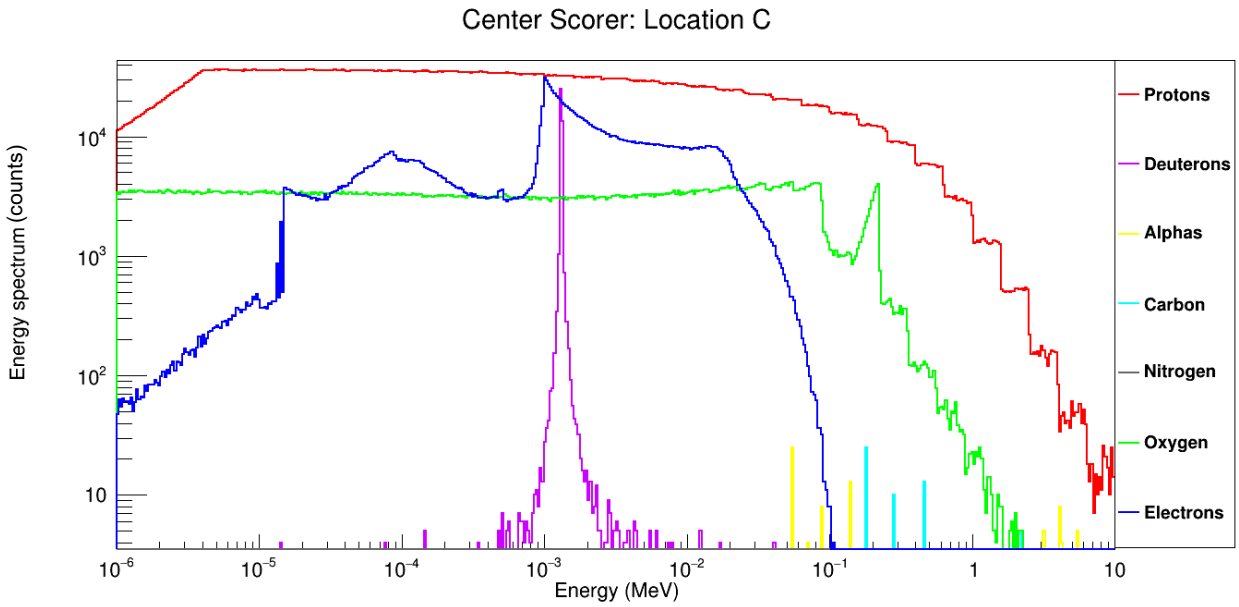
Center Scorer: Location C
Energy spectrum (counts)
Energy (MeV)
Protons
Deuterons
Alphas
Carbon
Nitrogen
Oxygen
Electrons

(c)

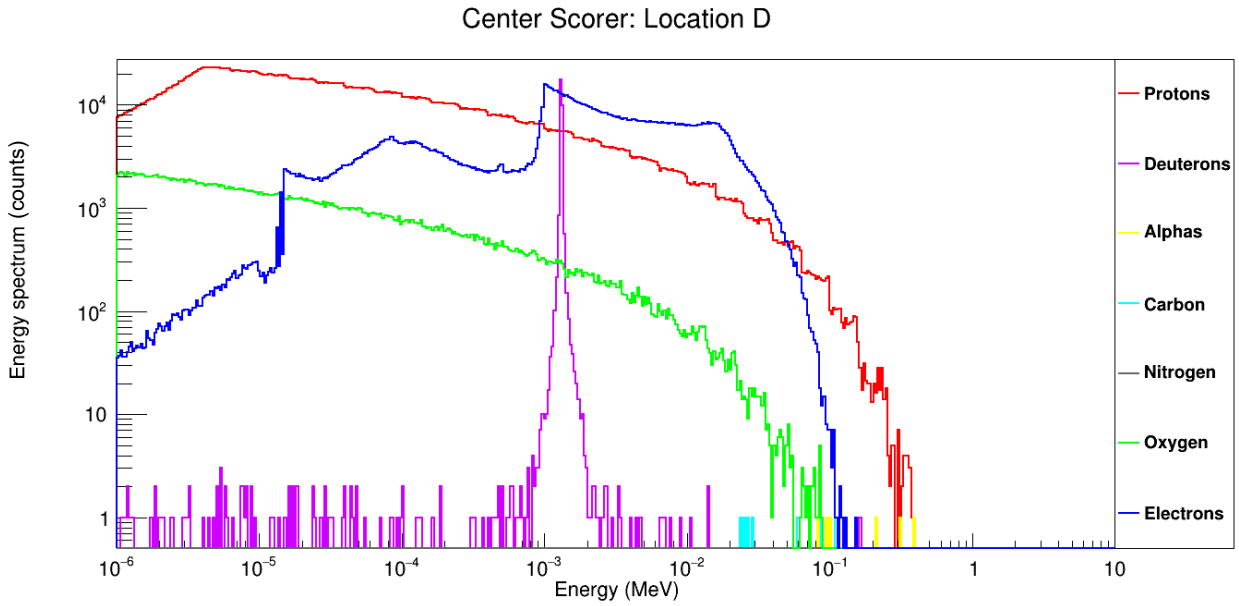


(d)

Figure 7.8 Secondary charged particle spectra produced in the center scoring volume of the flask geometry modeled in TOPAS v3.6. The flask was isotropically irradiated using realistic neutron spectra for locations A, B, C, and D. Panels (a), (b), (c), and (d) correspond to the secondary charged particle spectra produced by the neutron spectra at locations A, B, C, and D, respectively.

### 7.9.2 Relative dose contributions

Figure 7.9 illustrates the relative dose contributions of secondary species in the center scoring volume of the flask for all measurement locations. The contribution of protons to the relative dose decreases significantly as the measurement location shifts outside the treatment room (location D). Only protons, electrons, and oxygen ions contribute meaningfully to dose deposition in the scoring volumes, while the contributions from other secondary particles are negligible.

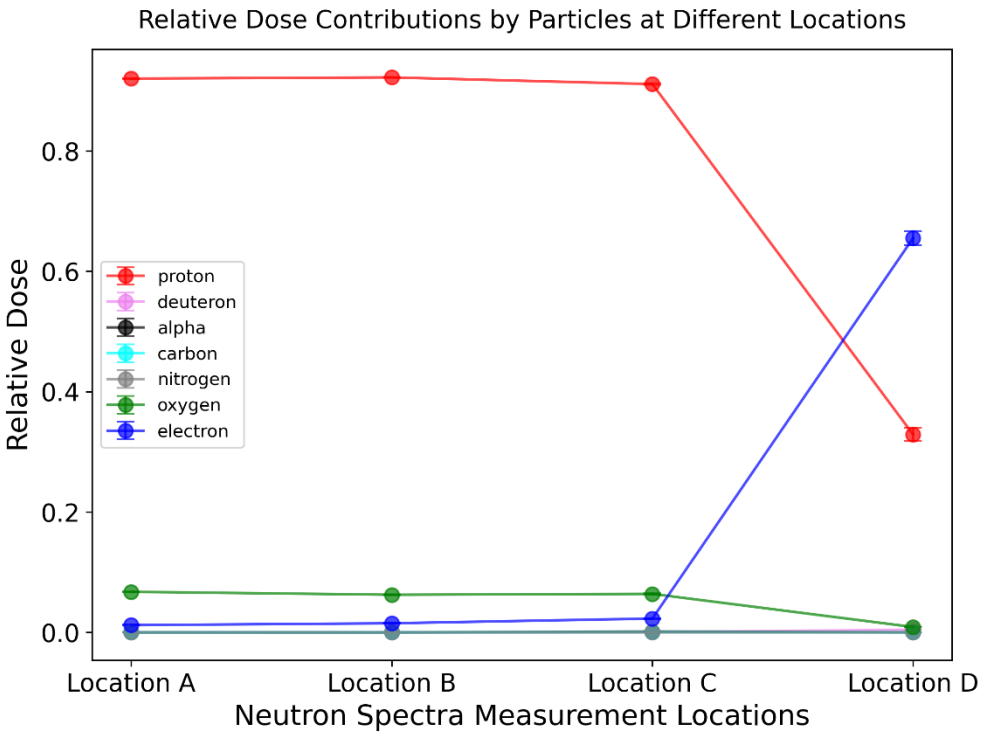


Figure 7.9 Relative dose contributions of secondary particles in the center scoring volume of flask as a function of realistic neutron spectra locations. Only protons, electrons, and oxygen were considered in this study. Lines are drawn to guide the eye.

## 7.10 250 keV X-ray

A reference radiation of 250 keV X-rays was used to estimate the neutron RBE. All steps in our simulation pipeline were repeated, replacing the realistic neutron spectra with 250 keV X-rays. First, the flask was irradiated with 250 keV X-rays to record the electron spectra in all scoring volumes. At 250 keV, electrons are the only secondary charged particles of interest produced by photon interactions. The recorded electron spectra were then input into our DNA model to calculate DNA damage yields in all scoring volumes. The electron spectrum recorded in the center scoring volume of the flask is shown in Figure 7.10.

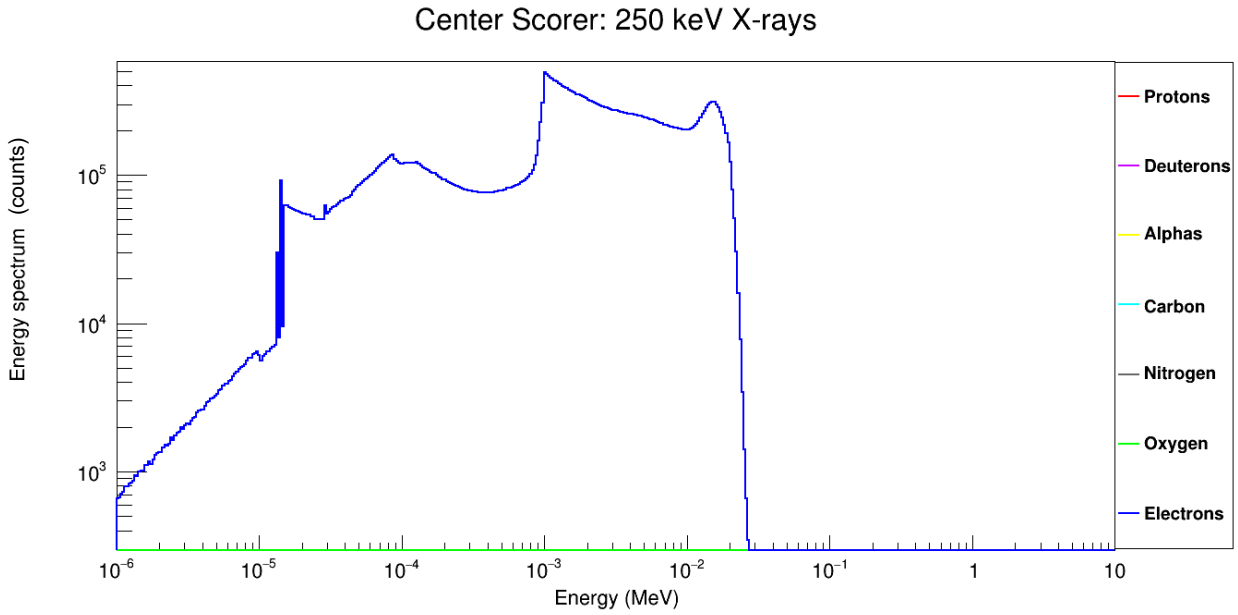


Figure 7.10 The secondary electron spectra produced by 250 keV X-rays in the center scoring volume of flask geometry.

## 7.11 DNA damage yields

Figure 7.11 shows the complex DNA DSB yields per Gy per Gbp at locations A, B, C, and D, as well as for 250 keV X-rays, for a cumulative dose of 1 Gy recorded in the center scoring volume of the flask. We used our updated DNA model code in TOPAS-CDD to calculate DNA DSB yields, scoring direct, indirect, and hybrid types of damage. The DNA damage yields for realistic neutron spectra of each location and each scoring volume of the flask were determined by combining species-specific damage yields through a weighted sum formula described in section 5.2.2. The reported values of yields for a given location and dose were mean values of 10 independent simulation runs.

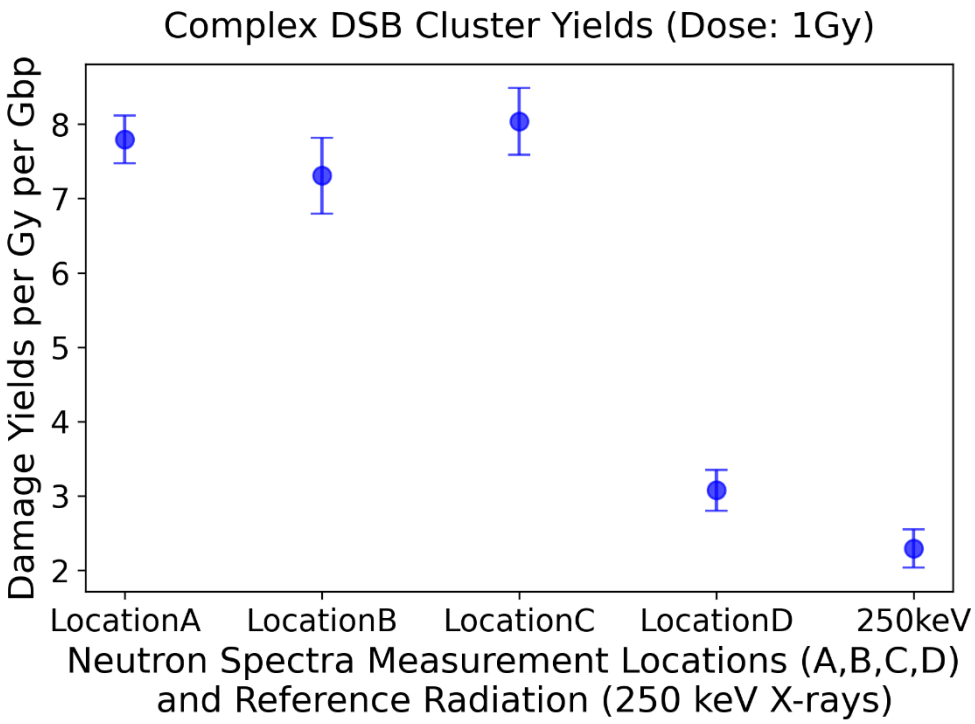


Figure 7.11 Yields of complex DSB clusters (per Gy of delivered dose per Gbp) as a function of measurement locations for realistic neutron spectra at locations A, B, C, and D, compared to reference radiation (250 keV X-rays). The plotted values represent the mean obtained from 10 statistically independent simulations, with error bars indicating the standard uncertainty of the mean.

## 7.12 Neutron RBE estimation

The complex DNA DSB yields were divided by the corresponding DNA damage yields obtained from 250 keV X-rays for a target dose of 1 Gy to estimate the RBE at each location. The RBE values estimated at each location for a cumulative dose of 1 Gy are presented in Figure 7.12.

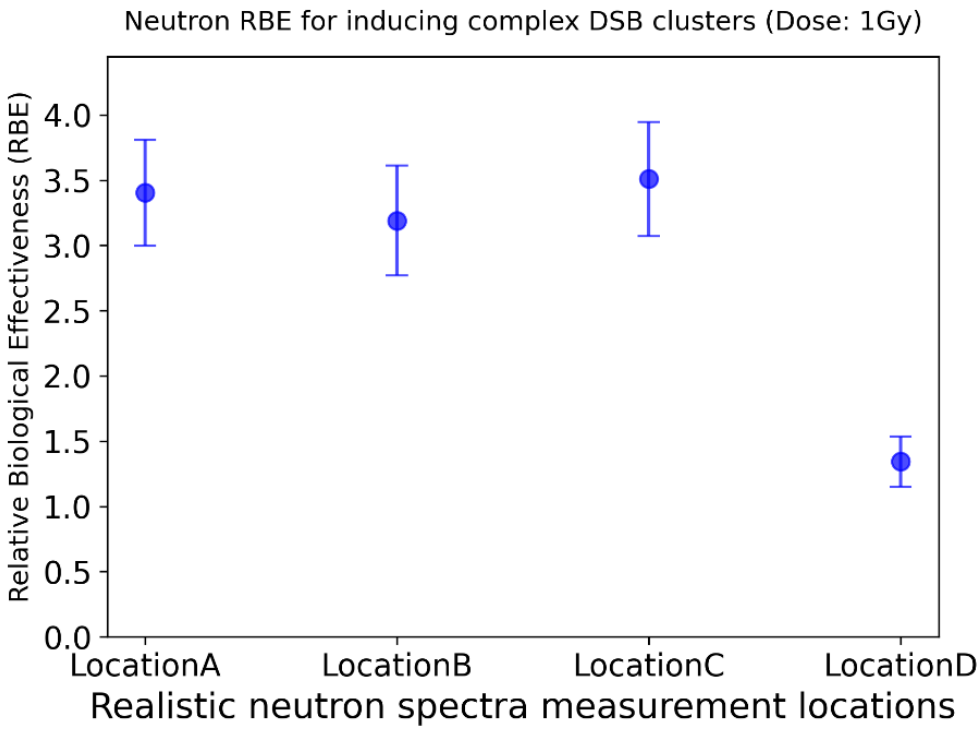


Figure 7.12 Neutron RBE for inducing complex DSB clusters at a target dose of 1 Gy, plotted against measurement locations for realistic neutron spectra. The plotted values are the mean values obtained over 10 statistically independent simulations. Error bars represent the standard deviation of the mean.

## 7.13 Neutron RBE as a function of dose

We conducted an additional set of simulations for target doses of 0.1 Gy, 0.5 Gy, 1.5 Gy, 2.0 Gy, 3.0 Gy, and 5.0 Gy at each location. Figure 7.13 illustrates the variation of neutron RBE as a function of dose for all locations.

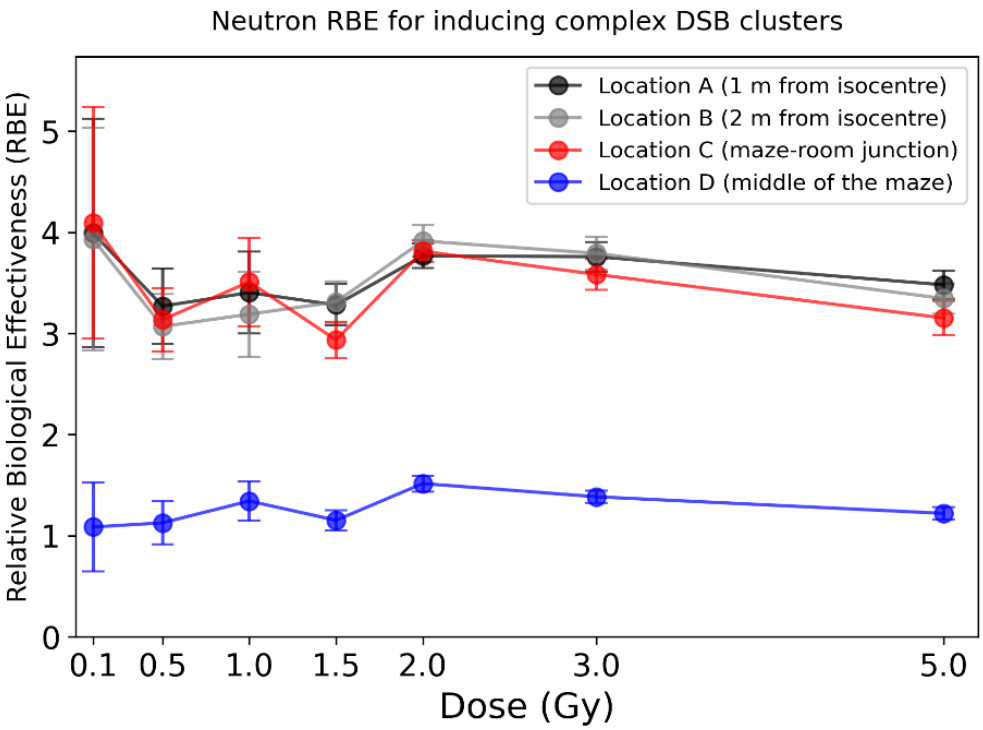


Figure 7.13 Variation of neutron RBE as a function of dose for all realistic neutron spectra measurement locations in the 15 MV linac bunker. Error bars represent the standard uncertainty of the mean. Lines are drawn to guide the eye.

## 7.14 Neutron RBE variation with location

To assess the fluctuation of RBE at each location, we plotted the neutron RBE for all target doses at every location, as shown in Figure 7.14.

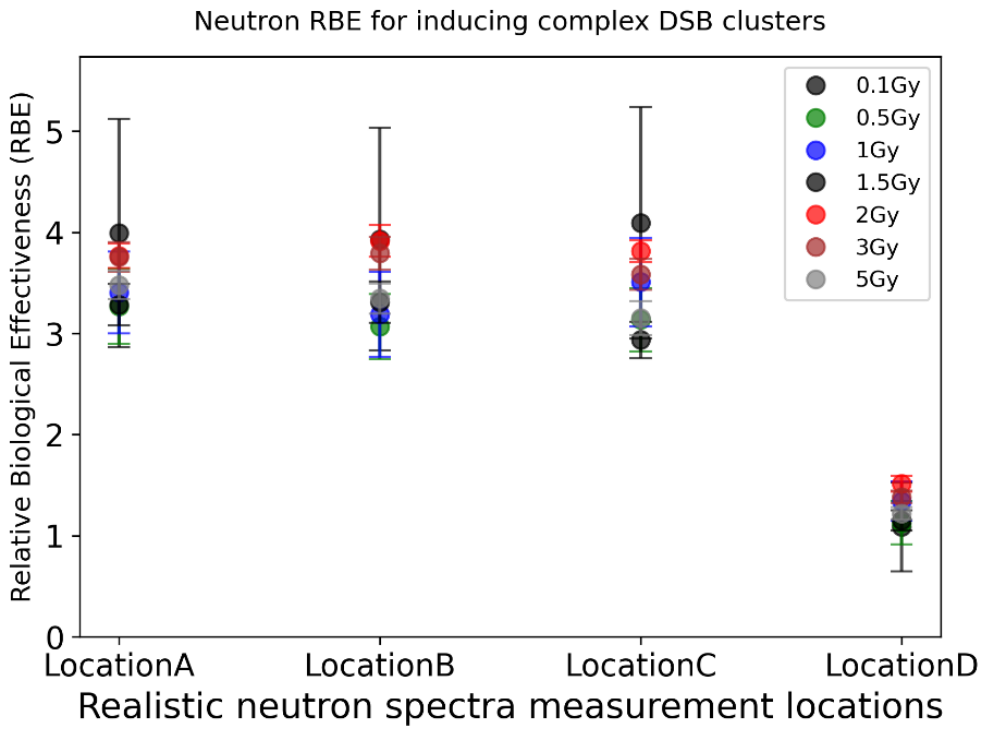


Figure 7.14 Impact of varying the total delivered dose on neutron RBE for inducing complex DSBs at each measurement location of realistic neutron spectra. The plotted values are the mean values obtained over 10 statistically independent simulations. Error bars represent the standard deviation of the mean.

# Chapter 8

# Discussion

## 8.1 Neutron simulations in the ICRU sphere

### 8.1.1 Charged particle spectra

As neutrons travel through the ICRU phantom, they scatter and lose energy through multiple elastic collisions, primarily with hydrogen nuclei. This moderation process results in a polyenergetic neutron spectrum within the phantom and reduced effective neutron energy at greater depths. Below, we discuss the particle spectra that are produced for each of the 1 keV, 1 MeV, and 10 MeV neutron beams that were examined in this thesis project.

**1 keV neutron irradiation:**

At an initial energy of 1 keV, neutron interactions are dominated by elastic scattering with hydrogen nuclei (protons) and other elements such as carbon, nitrogen, and oxygen in the phantom. Due to the low neutron energy, the recoiling protons also have low energy, as seen in Figure 7.1 (a1-a3). The secondary particles observed are primarily protons and electrons, with the electron contribution increasing with depth.

The electrons are generated by the $^{1}H(n,\gamma)^{2}H$ (Q = 2.225 MeV) neutron capture reaction, which is abundant due to the high hydrogen content in the phantom. This reaction results in the formation of deuterons ($^{2}H$) and the release of γ-rays, which further produce electrons via interactions in the medium. Since all secondary charged particles (except electrons) are terminated at the point of formation in the simulation, deuterons appear as peaks in the spectra across all depths, as they are captured and recorded immediately after their generation. Other significant reactions producing deuterons include $^{14}N(n,d)^{13}C$ and $^{16}O(n,d)^{15}N$.

A second peak in the proton energy spectra around ~580 keV is attributed to direct neutron-proton elastic scattering. The ~580 keV proton peak is due to the $^{14}N(n,p)^{14}C$

reaction. When a thermal neutron undergoes this reaction, nearly all the Q-value energy (626 keV) is transferred to the emitted proton because the resulting $^{14}C$ is much heavier and recoils with negligible energy. The presence of recoil oxygen, carbon, and nitrogen nuclei is due to elastic scattering with these elements, but the number of recoiling nuclei decreases with depth as the neutrons lose energy.

The ~40 keV carbon peak is likely the result of a neutron capture reaction where a neutron is absorbed by a carbon nucleus, causing the carbon nucleus to recoil and be recorded in the spectra.

**1 MeV neutron irradiation:**

At 1 MeV, more interaction channels are available compared to 1 keV. While elastic scattering with hydrogen remains the dominant interaction, the recoil protons now have higher energies, forming the main component of secondary species (Figure 6.1 (b1-b3)). The height of the proton energy spectra remains relatively stable across different depths. At this energy, inelastic scattering also becomes significant, with neutrons exciting nuclei like oxygen and nitrogen, which de-excite by emitting γ-rays. These interactions are reflected in the observed oxygen and nitrogen energy spectra at all depths. A peak in the oxygen energy spectra at ~0.2 MeV may result from neutron capture by oxygen, leading to the emission of a proton and the formation of nitrogen-16, contributing to both the nitrogen and proton spectra. The $^{14}N(n,p)^{14}C$ (Q = 0.626 MeV) neutron capture reaction produces carbon ions and protons, with the recoil energy of carbon-14 likely responsible for the carbon peaks observed in the spectra. The ~40 keV carbon peak persists and overlaps with the broad carbon spectrum from elastic scattering.

As the neutrons lose energy with depth, the number of heavy ions produced by scattering decreases due to the lower effective neutron energies.

**10 MeV neutron irradiation:**

At 10 MeV (Figure 7.1 (c1-c3)), neutrons have a higher penetrating power, resulting in less thermalization and more energetic secondary particles. The elastic scattering interactions produce more energetic protons, and inelastic scattering leads to a higher proportion of heavy ions and γ-rays.

This is especially evident in the increase of electron energy spectra at all depths, which are produced by interactions of high-energy γ-rays. Inelastic scattering also leads to excitation of carbon (first excited level at 4.439 MeV), nitrogen (2.311 MeV), and oxygen (6.05 MeV) [53], contributing to the higher observed energies of secondary particles.

The presence of α-particles is due to (n,α) reactions on carbon, nitrogen, and oxygen. It was observed that the electron energy spectra remain below 100 keV at all neutron energies and depths. This could be due to the nature of γ interactions and ionization processes that typically produce low-energy secondary electrons.

### 8.1.2 Relative dose contributions

**1 keV neutron energy**:

For primary neutrons at 1 keV, electrons dominate across all scoring volumes (Figure 7.2 (a-c)). This is primarily due to the hydrogen capture reaction $^{1}H(n,\gamma)^{2}H$, which emits a 2.225 MeV γ-ray. These γ-rays interact with matter, liberating a significant number of electrons through processes such as Compton scattering and photoelectric absorption. Protons generated by elastic scattering at 1 keV are relatively low in energy and contribute minimally compared to the more energetic electrons.

Since thermal neutrons (~0.025 eV) are more likely to undergo capture reactions due to their low energy, this effect highlights the increased probability of neutron capture at lower energies. As neutron energy increases, the capture probability (and thus electron dominance) decreases.

**1 MeV neutron energy**:

For primary neutrons at 1 MeV, protons become the most significant contributors across all depths, resulting from elastic scattering reactions with higher-energy protons produced compared to the 1 keV case. The likelihood of the $^{1}H(n,\gamma)^{2}H$ capture reaction decreases at 1 MeV due to a lower capture cross-section, leading to fewer secondary γ emissions and, consequently, fewer electrons. Oxygen nuclei begin contributing significantly at 1 MeV, reaching up to 11% in the outer scoring volume, as reactions with oxygen become more probable.

**10 MeV neutron energy**:

For primary neutrons at 10 MeV, protons remain dominant due to the production of even more energetic protons via elastic scattering, while neutron capture continues to decrease with increasing energy. At 10 MeV, inelastic reactions involving heavier ions become relevant. The increased neutron energy surpasses inelastic thresholds, leading to the production of heavy ions like carbon and α-particles. The dose contribution from carbon ions rises at 10 MeV, reaching around 2-3% across scoring volumes due to higher cross-sections for inelastic reactions involving carbon and other heavier elements at this energy level.

## 8.2 Thermal neutron models

This section discusses the impact of using thermal hydrogen in water and the application of additional high-precision models for thermal neutron scattering. Lund *et al.* (2020) [10] utilized an additional dataset, G4ParticleHPThermalScattering, to improve the transport of thermal neutrons below 4 eV. However, they mistakenly used standard hydrogen instead of thermal hydrogen in water when building the ICRU phantom. Consequently, the G4ParticleHPThermalScattering dataset was never activated in their simulations. To validate this, a comparison between the proton energy spectra obtained from TOPAS v3.6 in this study and Geant4 v10.06 is presented in Figure 7.4 (a-c) for all neutron energies within the intermediate scoring volume. It is clear that below 4 eV, the proton spectra in Geant4 resemble an extrapolation. The simulations were then repeated using thermal hydrogen in water when constructing the ICRU phantom in Geant4 v10.06, resulting in proton spectra that match well with TOPAS v3.6 (see Figure 7.5 (a-c)).

The effect of using thermal hydrogen in water instead of standard hydrogen on neutron RBE was not explicitly analyzed in this thesis. However, the presence of thermal hydrogen in water improved the secondary proton spectra and enabled accurate modeling of thermal neutron transport in our simulation setup.

The presence of thermal neutrons plays a critical role in neutron RBE for inducing C-DSB clusters. Their contribution primarily arises from $^{14}N(n,p)^{14}C$, which release energetic protons (~580 keV). These protons create dense ionization tracks that

significantly enhance DNA damage complexity, making the resulting damage more challenging to repair.

## 8.3 Local approximation and High-energy electrons

Recall that Lund *et al.* (2020) [10] applied a local approximation to record energy spectra of secondary charged particles, allowing electrons to interact down to 1 MeV. Once below 1 MeV, electrons were terminated, and their kinetic energies were recorded, creating a peak at 1 MeV (Figure 7.6 (a-c)). In our approach, electrons interacted down to 0 eV. For 1 keV and 1 MeV (Figure 7.6 (a) and (b)), Geant4 electron spectra were higher than those from TOPAS, as Geant4 terminated electrons at 1 MeV, while we allowed further interaction and energy deposition within the phantom. Here, electrons were generated from the 2.225 MeV γ-ray of the $^{1}H(n,\gamma)^{2}H$ capture reaction, decreasing in number and energy with interactions.

At 10 MeV (Figure 7.6 (c)), the TOPAS electron spectrum exceeded Geant4's. This results from higher initial electron energy, leading to multiple interactions that produced more low-energy delta rays. Lund *et al.* (2020) [10] terminated electrons ≤1 MeV, limiting interaction within the ICRU material. Higher-energy γ-rays at 10 MeV primarily interacted via Compton scattering, generating more energetic secondary electrons due to increased Compton transfer fractions.

The effect of the altered electron spectra obtained in this thesis, compared to Lund *et al.* (2020), on neutron RBE was not explicitly investigated.

## 8.4 Realistic Neutron Spectra

**ICRU sphere phantom:**

The shape of secondary species recorded in the intermediate spectra of an ICRU phantom irradiated with realistic neutron spectra from Locations A, B, and C (see Figure 7.8 (a-c)) closely resembles that produced by an initial 1 MeV neutron energy (Figure 7.1 (b2)). However, the spectral intensity for all secondary charged particles decreases progressively from Location A to C. Locations A, B, and C, where neutron spectra were measured, are within the treatment room, while Location D is situated outside the

treatment room, midway through the maze. The average neutron energy decreases from 240 keV at Location A to approximately 1 keV at Location D, where electrons dominate the secondary species energy spectra.

**In-vitro geometry:**

As we move further from the linac (from Location A to C) within the treatment room, the shape of secondary species spectra in the center scorer of the flask geometry, as shown in Figure 7.9 (a-c), remains largely unchanged. Significant secondary species include electrons, protons, oxygen ions, and a prominent deuteron peak at 1 keV. At Location C, however, some higher-energy α-particles and carbon ions are also observed. Protons are the dominant species at all locations within the treatment room.

At Location D, outside the treatment room, the recorded secondary species display comparatively lower energies due to neutron attenuation by the maze wall. Here, electrons dominate over protons within the 1 keV to 100 keV energy range. Consistent with expectations, protons contribute most significantly to the dose at all locations within the treatment room, while electrons contribute the highest dose outside the treatment room. This behavior mirrors the 1 keV initial neutron energy case discussed in Section 7.1.2, as the average neutron energy at Location D is approximately 1 keV.

Comparing the secondary species spectra recorded in the ICRU sphere and the flask after irradiation with the realistic neutron spectra, it was observed that the spectral shapes of all secondary species matched well in both cases at all locations. Since the ICRU sphere is composed of tissue-equivalent materials, whereas the flask is made of polystyrene (which lacks nitrogen), the nitrogen spectrum was not observed in the flask. Consequently, no inelastic neutron scattering with nitrogen occurred in the flask.

Additionally, it was noted that protons dominate over electrons in the flask. This can be attributed to the high proportion of hydrogen atoms in polystyrene, which effectively moderate neutrons through elastic scattering. Given that hydrogen and neutron masses are nearly equal, neutrons can transfer almost all their kinetic energy to protons in a single collision, leading to a significant population of recoil protons in the flask.

### Electron spectra in Neutron Irradiation Simulations

Regardless of the initial neutron energy (1 keV, 1 MeV, and 10 MeV), the electron spectra in our simulations never exceed 100 keV. These electrons are primarily generated by the $^{1}H(n,\gamma)^{2}H$ neutron capture reaction (Q = 2.225 MeV). Although the 2.225 MeV gamma-ray is relatively energetic, Compton scattering is the dominant interaction process, with the maximum electron energy transfer from a single scattering event typically around 511 keV. The simulation materials used, including the ICRU sphere and polystyrene, are low-Z, which results in a softer gamma spectrum. Additionally, the use of the Livermore low-energy electromagnetic model, which is optimized for precise tracking of low-energy electrons, may further suppress the production of higher-energy electrons.

## 8.5 250 keV X-rays secondary particle spectra in the flask

At 250 keV, both photoelectric absorption and Compton scattering can occur, though the photoelectric effect is less significant and contributes only modestly to the overall dose. Compton scattering is the predominant interaction at this energy in tissue-equivalent materials like the ICRU phantom [12], producing scattered photons and recoil electrons. The electrons generated in these interactions transfer their energy through ionization and excitation of atoms in the phantom, leading to a spread of dose throughout the material. This results in a dose distribution characteristic of mid-energy X-rays, as shown in Figure 7.11.

## 8.6 DSB damage yields

The yields of complex DSB clusters were determined in the central scoring volume of the flask geometry by irradiating our DNA model in track-structure simulations using secondary species spectra of electrons, protons, and oxygen ions corresponding to the realistic neutron spectra at different locations. As outlined in Section 8.5, the secondary species spectra for locations A, B, and C closely resemble each other, and their corresponding complex DSB cluster yields were also similar for a target dose of 1 Gy (see Figure 7.12). However, the yields at location D were comparatively lower, as electrons

contribute more significantly to dose at this location, whereas protons are the primary dose contributors at locations A, B, and C.

## 8.7 Neutron RBE

This section presents a rationale for neutron RBE as a function of realistic neutron spectra at different locations. Based on the complex DSB cluster yields, neutron RBE was calculated by dividing the yields at each location by the yields obtained with 250 keV X-rays for the same target dose. As expected, neutron RBE follows a similar trend to that of complex DNA DSB yields (see Figure 7.13). Additionally, simulations were performed for target doses of 0.1 Gy, 0.5 Gy, 1.5 Gy, 2.0 Gy, 3.0 Gy, and 5 Gy. The RBE values as functions of dose and spectra location are shown in Figure 7.14. The error bars in RBE values are highest at 0.1 Gy and decrease with increasing target dose. An unexpected fluctuation in neutron RBE with dose highlights an important feature of secondary neutrons, warranting further investigation in future studies as we expected no dose dependence in neutron RBE for inducing complex DSB clusters.

## 8.8 Limitations

### 8.8.1 Heavy ion simulations in TOPAS-nBio

Our DNA model is currently unable to simulate the transport of ions heavier than α-particles due to inherent limitations in TOPAS-nBio and Geant4-DNA. These codes can only simulate the ionization of heavy ions, but not their full transport. In contrast, Baiocco *et al.* (2016) conducted track-structure simulations of heavy ions (C, N, and O) using the PARTRAC code. Lund *et al.* (2020) [10] found that heavy ions can contribute up to 14% of the dose in simulations involving 10 MeV neutrons. Despite this, we have calculated the energy spectra and relative dose contributions of heavy ions in our condensed history simulations. Once heavy ion transport models become available in TOPAS-nBio and Geant4-DNA in future, our code will be able to easily adapt to these new capabilities.

### 8.8.2 Limitations of our DNA model

Our DNA model was initially developed by Montgomery *et al.* (2021) and later updated by Manalad *et al.* (2023) [50] to include the indirect action of radiation damage. However, the

physical and biological modeling limitations identified in the original model were not addressed by Manalad *et al.* (2023) [50] and remain unchanged. These limitations include (i) the cubic shape of the model, which does not reflect the typically ellipsoidal shape of fibroblast nuclei, and (ii) the lack of connectivity between chromatin fibers. Despite these constraints, the results of our DNA model were validated against published literature by Manalad *et al.* (2023) [50] and were found to be consistent.

### 8.8.3 Limitations in chemical simulations

The updated nuclear DNA model provided by Manalad *et al.* (2023) [50] was used in this thesis, and as a result, it inherits the same limitations discussed in their work. At the time of their study, they employed the TsEmDNAChemistry constructor for simulating chemical species, which was the latest available chemistry constructor. However, an updated version, TsEmDNAChemistryExtended, is now available in TOPAS-nBio, offering simulations of a broader range of chemical species though it was not used in this study.

Other chemistry-related limitations of our DNA model, as outlined in the previous work [50], include the simulation of chemical species propagation in pure liquid water at neutral pH and 25°C. This does not fully reflect real-world conditions, as the pH of cells is not neutral, and human body temperature is not 25°C. However, new chemistry models in TOPAS-nBio now offer temperature-dependent G-values for chemical species in liquid water from 20°C to 90°C, and temperature-dependent yields for SSBs and DSBs from 0°C to 42°C but were not utilized in this study.

# Chapter 9

# Summary, conclusion, and future work

## 9.1 Summary and Conclusions

The use of ionizing radiation offers great benefits to society. However, radiation may be detrimental to human health. The use of radiation thus entails an associated non-zero risk. The unwanted photoneutron exposure to patients during high-energy (> 8 MeV) radiation therapy is one such example of a risk associated with the use of radiation [4, 54]. This unavoidable exposure of secondary neutrons can potentially cause patients to develop iatrogenic secondary cancers later in life [55]. The risk for inducing stochastic effects associated with neutrons is energy dependent and relatively higher in magnitude as compared to other types of radiation. The energy dependence of neutron-induced stochastic effects is typically quantified by neutron radiation weighting factors ($w_R$) provided by International Commission on Radiological Protection (ICRP 2003, 2007) [14, 56] and the neutron quality factors (Q) published by the United States Regulatory Commission (US NRC 2021) [41]. Although the factors $w_R$ and Q follow similar energy dependence trends qualitatively, their magnitudes are highly discrepant. The wide variety of neutron RBE data used to derive the weighting and quality factor potentially explains this discrepancy. This study is an expansion of our Neutron-Induced Carcinogenic Effects (NICE) research group's efforts to trace the biophysical origin of neutron RBE [4, 10, 28, 29, 50]. We generated secondary charged species spectra produced by monoenergetic neutrons of initial energies 1 keV, 1 MeV, and 10 MeV by modeling an ICRU-4 sphere phantom in TOPAS v3.6. To validate our TOPAS simulations, we replicated Lund *et al.* (2020) [10] simulations in Geant4 v10.06, comparing the secondary species spectra and their relative dose contributions. During this process, we addressed errors in Lund *et al*. (2020) [10] by (i) reconstructing the ICRU phantom using thermal hydrogen of water (TS_H_of_Water) to activate thermal neutron models, (ii) refining local approximation conditions for electron energy spectra calculations. We allowed electrons to interact freely until they reached 0 eV and recorded their dose

deposition, addressing an inconsistency where Lund et al. (2020) [10] terminated electron tracks below 1 MeV.

Furthermore, we developed a TOPAS extension to simulate thermal neutron transport below 4 eV by importing the G4NeutronHPThermalScattering model, following the approach of Lund *et al.* (2020) [10] in condensed history simulations. Thus, we enabled the accurate transportation of thermal neutrons in TOPAS for the first time contributing to advance the capabilities of TOPAS simulation application. Once we get assured that our ICRU sphere modeling in TOPAS is correct and all results match well with Geant4 demonstrating the robustness of both our methodology and results, we further modeled a flask geometry in TOPAS used for in-vitro experimental cell irradiations. We defined various scoring volumes in the flask to collect the secondary charged particles spectra by irradiating it with the realistic neutron spectra measured at several locations in a 15 MV linac bunker. Out of the various secondary species spectra collected in the center scorer of the flask, ns, protons, and oxygen ions were considered, and their energy spectra and relative dose contributions were used in subsequent track structure simulations. These simulations involved our geometric DNA model [28], irradiated with the spectra of secondary species. This approach yielded five types of DNA damage for a cumulative dose of 1 Gy, corresponding to realistic neutron spectra at each location. Simulations with 250 keV X-rays provided comparative damage yields, allowing us to calculate photoneutron RBE in the central scoring volume (~3.5 in bunker location A-C, and ~1.3 at location D outside the bunker) by taking the ratio of complex DSB clusters induced by neutron spectra to those induced by 250 keV X-rays. Additional simulations at doses of 0.1 Gy, 0.5 Gy, 1.5 Gy, 2.0 Gy, 3.0 Gy, and 5.0 Gy explored neutron RBE variation with dose. Future avenues for exploration with this simulation pipeline are discussed below.

## 9.2 Future work

### 9.2.1 Temperature-dependent DNA damage yields

All types of DNA damage yields reported by our DNA model were calculated at ambient temperature. It would be valuable to investigate how the yields of DNA SSBs and DSBs

and thus neutron RBE values are affected by variations in environmental temperature, which can be simulated using the latest version of TOPAS-nBio [57].

### 9.2.2 DNA Repair models

Our DNA model currently considers direct and indirect DNA damage induced by radiation. Integrating DNA repair models in our simulation pipeline might affect the damage yields and resulting neutron RBE. Our research group is currently working on incorporating DNA repair kinetics through two distinct mechanistic repair models: DaMaRis (DNA Mechanistic Repair Simulator) [58-62] and MEDRAS (Mechanistic DNA Repair And Survival) [63-65]. Both repair models can be linked to the TOPAS-nBio framework via the Standard for DNA Damage (SDD). Integration of a repair model has the potential to predict clinically relevant endpoints and support treatment personalization in the future.

### 9.2.3 Scoring volume dimensions

An important direction for future research could be to investigate the effects of scoring volume dimensions on secondary species spectra. Utilizing a molecular dynamics tool like LAMMPS (Large-scale Atomic/Molecular Massively Parallel Simulator) could allow for the simulation of cells and nuclei with dimensions based on those used in in-vitro experiments. By designing scoring volumes that reflect the actual sizes of nuclei within cells, rather than the 1.5 cm radius used in this study, secondary species spectra could be collected in condensed history simulations more accurately. This approach would bring the study closer to real-world conditions of radiation-induced DNA damage in cells.

# References


1. Ruddon, R.W., *Cancer Biology*. Fourth ed. 2007: Oxford University Press.
2. E. Hall, A.G., *Radiobiology for the Radiologist*. 7th ed. 2012: Lippincott Williams & Wilkins, Philadelphia, Pa.
3. *Canadian Cancer Statistics*. 2023, Canadian Cancer Society.
4. Maglieri, R., et al., *Measuring neutron spectra in radiotherapy using the nested neutron spectrometer.* Med Phys, 2015. **42**(11): p. 6162-9.
5. Perl, J., et al., *TOPAS: An innovative proton Monte Carlo platform for research and clinical applications.* Medical Physics, 2012. **39**(11): p. 6818-6837.
6. Schuemann, J., et al., *TOPAS-nBio: An Extension to the TOPAS Simulation Toolkit for Cellular and Sub-cellular Radiobiology.* Radiation Research, 2019. **191**(2): p. 125-138.
7. Agostinelli, S., et al., *GEANT4-a simulation toolkit.* Nuclear Instruments & Methods in Physics Research Section a-Accelerators Spectrometers Detectors and Associated Equipment, 2003. **506**(3): p. 250-303.
8. Allison, J., et al., *Geant4 developments and applications.* Ieee Transactions on Nuclear Science, 2006. **53**(1): p. 270-278.
9. Allison, J., et al., *Recent developments in GEANT4.* Nuclear Instruments & Methods in Physics Research Section a-Accelerators Spectrometers Detectors and Associated Equipment, 2016. **835**: p. 186-225.
10. Lund, C.M., et al., *A microdosimetric analysis of the interactions of mono-energetic neutrons with human tissue.* Phys Med, 2020. **73**: p. 29-42.
11. Attix, F.H., *Introduction to Radiological Physics and Radiation Dosimetry*. 1986: WILEY-VCH Verlag GmbH & Co. KGaA.
12. Podgoršak, E., *Radiation physics for medical physicists, 3rd Ed.* . 2016, Springer International Publishing, Switzerland.
13. ICRU, *ICRU 85a (Revised) Fundamental Quantities and Units for Ionizing Radiation*. 2011.
14. ICRP, *ICRP Publication 103: The 2007 recommendations of the International Commission on Radiological Protection*. 2007. p. 2-4.
15. *Hitting the Jackpot: The Birth of the Monte Carlo method* 2023; Available from: https://www.lanl.gov/media/publications/actinide-research-quarterly/first-quarter-2023/hitting-the-jackpot-the-birth-of-the-monte-carlo-method.
16. Forster, R.A., Godfrey, T.N.K., *MCNP - a general Monte Carlo code for neutron and photon transport.*, in *Monte-Carlo Methods and Applications in Neutronics, Photonics and Statistical Physics*. 1985, Springer, Berlin, Heidelberg.
17. Kawrakow I, R.D., Mainegra-Hing E, Tessier F, Townson RW, Walters BRB, *EGSnrc toolkit for Monte Carlo simulation of ionizing radiation transport.* 2000.
18. Bernal, M.A., et al., *Track structure modeling in liquid water: A review of the Geant4-DNA very low energy extension of the Geant4 Monte Carlo simulation toolkit.* Physica Medica-European Journal of Medical Physics, 2015. **31**(8): p. 861-874.

19. Incerti, S., et al., *The Geant4-DNA Project*. International Journal of Modeling Simulation and Scientific Computing, 2010. **1**(2): p. 157-178.
20. Incerti, S., et al., *Comparison of GEANT4 very low energy cross section models with experimental data in water*. Medical Physics, 2010. **37**(9): p. 4692-4708.
21. Incerti, S., et al., *Geant4-DNA example applications for track structure simulations in liquid water: A report from the Geant4-DNA Project*. Medical Physics, 2018. **45**(8): p. E722-E739.
22. Rogers, D.W., et al., *BEAM: a Monte Carlo code to simulate radiotherapy treatment units*. Med Phys, 1995. **22**(5): p. 503-24.
23. Walters B. R, K.I., Rogers D. W., *DOSXYZnrc Users Manual*, in *NRC Report PIRS 794 (rev B)*. 2005.
24. ICRU, *Tissue Substitutes in Radiation Dosimetry and Measurement*. 1989: Bethesda, MD.
25. Mendez, J.R. *TOPAS-nBio v3.0*. 2024; Available from: https://github.com/topas-nbio/TOPAS-nBio/releases/tag/latest.
26. Standards, N.B.o., *Report of the International Commission on Radiological Units and Measurements (ICRU)* 1956.
27. Pray, L., *Discovery of DNA Structure and Function: Watson and Crick*. Nature Education, 2008. **1**.
28. Montgomery, L., et al., *Towards the characterization of neutron carcinogenesis through direct action simulations of clustered DNA damage*. Phys Med Biol, 2021. **66**(20).
29. Kildea, J., *The Canadian Neutron-Induced Carcinogenic Effects Research Program: A research program to investigate neutron relative biological effectiveness for carcinogenesis with a particular focus on secondary (by-product) neutrons in high-energy radiation therapy*. Radiation Environment and Medicine 2017. **6**(2): p. 55-61.
30. Kildea, J. *Kildea Lab, Medical Physics Unit, McGill University, Canada*. Available from: https://kildealab.com/.
31. Baiocco, G., et al., *The origin of neutron biological effectiveness as a function of energy*. Sci Rep, 2016. **6**: p. 34033.
32. Ottolenghi, A., et al., *The ANDANTE project: a multidisciplinary approach to neutron RBE*. Radiat Prot Dosimetry, 2015. **166**(1-4): p. 311-5.
33. Sato, T., et al., *Particle and Heavy Ion Transport code System, PHITS, version 2.52*. Journal of Nuclear Science and Technology, 2013. **50**(9): p. 913-923.
34. Alloni, D., et al., *Track structure, radiation quality and initial radiobiological events: considerations based on the PARTRAC code experience*. Int J Radiat Biol, 2012. **88**(1-2): p. 77-86.
35. Friedland, W., et al., *Track structures, DNA targets and radiation effects in the biophysical Monte Carlo simulation code PARTRAC*. Mutat Res, 2011. **711**(1-2): p. 28-40.
36. Ivantchenko, A.V., et al., *Geant4 hadronic physics for space radiation environment*. Int J Radiat Biol, 2012. **88**(1-2): p. 171-5.
37. Perkins ST, C.D., Seltzer SM, *Tables and graphs of electron-interaction crosssections from 10 eV to 100 GeV derived from the LLNL evaluated electron data library (EEDL),*

*Z= 1–100*. 1991a, Lawrence Livermore National Lab. (LLNL), Livermore, CA (United States). p. 21-24.
38. Perkins ST, C.D., Chen MH, Rathkopf J, Scofield J, Hubbell JH, *Tables and graphs of atomic subshell and relaxation data derived from the LLNL Evaluated Atomic Data Library (EADL), Z= 1–100*. 1991b, Lawrence Livermore National Lab. (LLNL), Livermore, CA (United States).
39. Cullen DE, H.J., Kissel L, *EPDL97: the evaluated photo data library 97 version*. 1997, Lawrence Livermore National Lab., CA.
40. Famulari, G., P. Pater, and S.A. Enger, *Microdosimetry calculations for monoenergetic electrons using Geant4-DNA combined with a weighted track sampling algorithm.* Phys Med Biol, 2017. **62**(13): p. 5495-5508.
41. NRC, U., *Units of Radiation Dose* 2021. p. 298-300.
42. C. Villagrasa, S.M., G. Gonon, G. Gruel, U. Giesen, M. Bueno, and H. Rabus, *Geant4-dna simulation of dna damage caused by direct and indirect radiation effects and comparison with biological data*. EPJ Web of Conferences, 2017. **153**: p. 04019.
43. Zhu, H., et al., *Cellular Response to Proton Irradiation: A Simulation Study with TOPAS-nBio.* Radiat Res, 2020. **194**(1): p. 9-21.
44. Lieberman-Aiden, E., et al., *Comprehensive mapping of long-range interactions reveals folding principles of the human genome.* Science, 2009. **326**(5950): p. 289-93.
45. J. Perl, D.H., J. Shin, J. Schuemann, and J. Ramos-Méndez, *Modular Physics Lists*. 2016.
46. Tang, N., et al., *Influence of chromatin compaction on simulated early radiation-induced DNA damage using Geant4-DNA.* Med Phys, 2019. **46**(3): p. 1501-1511.
47. Charlton, D.E. and J.L. Humm, *A method of calculating initial DNA strand breakage following the decay of incorporated 125I.* Int J Radiat Biol Relat Stud Phys Chem Med, 1988. **53**(3): p. 353-65.
48. Martin, R.F. and W.A. Haseltine, *Range of radiochemical damage to DNA with decay of iodine-125*. Science, 1981. **213**(4510): p. 896-8.
49. Van Der Schans, G.P., *Gamma-ray induced double-strand breaks in DNA resulting from randomly-inflicted single-strand breaks: temporal local denaturation, a new radiation phenomenon?* Int J Radiat Biol Relat Stud Phys Chem Med, 1978. **33**(2): p. 105-20.
50. Manalad, J., L. Montgomery, and J. Kildea, *A study of indirect action's impact on simulated neutron-induced DNA damage.* Phys Med Biol, 2023. **68**(7).
51. Zhu, H., et al., *A parameter sensitivity study for simulating DNA damage after proton irradiation using TOPAS-nBio.* Phys Med Biol, 2020. **65**(8): p. 085015.
52. Mathew, F., et al., *Development of a passive gold-foil Nested Neutron Spectrometer to validate the active current-mode He-3 measurements in a high neutron fluence rate radiotherapy environment.* Nuclear Instruments & Methods in Physics Research Section a-Accelerators Spectrometers Detectors and Associated Equipment, 2021. **985**.
53. Caswell, R.S. and J.J. Coyne, *Interaction of neutrons and secondary charged particles with tissue: secondary particle spectra.* Radiat Res, 1972. **52**(3): p. 448-70.

54. Howell, R.M., et al., *Calculation of effective dose from measurements of secondary neutron spectra and scattered photon dose from dynamic MLC IMRT for 6 MV, 15 MV, and 18 MV beam energies.* Med Phys, 2006. **33**(2): p. 360-8.
55. Friedman, D.L., et al., *Subsequent neoplasms in 5-year survivors of childhood cancer: the Childhood Cancer Survivor Study.* J Natl Cancer Inst, 2010. **102**(14): p. 1083-95.
56. ICRP, *ICRP 92: Relative Biological Effectiveness (RBE), Quality Factor (Q), and Radiation Weighting Factor (wR)*, in *Annals of ICRP*. 2003.
57. Ramos-Mendez, J., et al., *TOPAS-nBio simulation of temperature-dependent indirect DNA strand break yields.* Phys Med Biol, 2022. **67**(14).
58. Henthorn, N.T., et al., *Clinically relevant nanodosimetric simulation of DNA damage complexity from photons and protons.* Rsc Advances, 2019. **9**(12): p. 6845-6858.
59. Henthorn, N.T., et al., *Nanodosimetric Simulation of Direct Ion-Induced DNA Damage Using Different Chromatin Geometry Models.* Radiation Research, 2017. **188**(6): p. 690-703.
60. Henthorn, N.T., et al., *In Silico Non-Homologous End Joining Following Ion Induced DNA Double Strand Breaks Predicts That Repair Fidelity Depends on Break Density.* Scientific Reports, 2018. **8**.
61. Ingram, S.P., et al., *Mechanistic modelling supports entwined rather than exclusively competitive DNA double-strand break repair pathway.* Scientific Reports, 2019. **9**.
62. Warmenhoven, J.W., et al., *Insights into the non-homologous end joining pathway and double strand break end mobility provided by mechanistic modelling.* DNA Repair, 2020. **85**.
63. McMahon, S.J., et al., *Mechanistic Modelling of DNA Repair and Cellular Survival Following Radiation-Induced DNA Damage.* Sci Rep, 2016. **6**: p. 33290.
64. McMahon, S.J. and K.M. Prise, *A Mechanistic DNA Repair and Survival Model (Medras): Applications to Intrinsic Radiosensitivity, Relative Biological Effectiveness and Dose-Rate.* Front Oncol, 2021. **11**: p. 689112.
65. McMahon, S.J., et al., *A general mechanistic model enables predictions of the biological effectiveness of different qualities of radiation.* Scientific Reports, 2017. **7**.